Application of fluid inclusions in geological thermometry

András Fall

Dissertation submitted to the faculty of the Virginia Polytechnic Institute and State University in partial fulfillment of the requirements for the degree of

Doctor of Philosophy
in
Geosciences

Committee
Robert J. Bodnar, Chair
Robert P. Lowell
J. Donald Rimstidt
Csaba Szabó
Robert J. Tracy

December 10, 2008
Blacksburg, Virginia

Keywords: fluid inclusion assemblages, fluid inclusion size, thermal history, homogenization temperature variation, ore deposits, microthermometry, Raman microspectrometry, CO_2 clathrate, salinity.

Application of fluid inclusions in geological thermometry

András Fall

ABSTRACT

Many geologic processes occur in association with hydrothermal fluids and some of these fluids are eventually trapped as fluid inclusions in minerals formed during the process. Fluid inclusions provide valuable information on the pressure, temperature and fluid composition (PTX) of the environment of formation, hence understanding PTX properties of the fluid inclusions is required.

The most important step of a fluid inclusion study is the identification of Fluid Inclusion Assemblages (FIA) that represent the finest (shortest time duration) geologic event that can be constrained using fluid inclusions. Homogenization temperature data obtained from fluid inclusions is often used to reconstruct temperature history of a geologic event. The precision with which fluid inclusions constrain the temperatures of geologic events depends on the precision with which the temperature of a fluid inclusion assemblage can be determined.

Synthetic fluid inclusions trapped in the one-fluid-phase field are formed at a known and relatively constant temperature. However, microthermometry of synthetic fluid inclusions often reveals T_h variations of about ± 1- 4 degrees Centigrade, or one order of magnitude larger than the precision of the measurement for an individual inclusion. The same range in T_h was observed in well-constrained natural FIAs where the inclusions are assumed to have been trapped at the same time. The observed small variations are the result of the effect of the fluid inclusion size on the bubble collapsing temperature. As inclusions are heated the vapor bubble is getting smaller until the pressure difference between the pressure of the vapor and the confining pressure reaches a critical value and the bubble collapses. It was observed that smaller inclusions reach critical bubble radius and critical pressure differences at lower temperatures than larger inclusions within the same FIA.

Homogenization temperature (T_h) variations depend on many factors that vary within different geological environments. In order to determine minimum and acceptable T_h ranges fro FIAs formed in different environments we investigated several geologic environments including sedimentary, metamorphic, and magmatic hydrothermal environments. The observed minimum T_h ranges range from 1-4 degrees Centigrade and acceptable T_h range from 5-25 degrees Centigrade. The variations are mostly caused by the fluid inclusion size, natural temperature and pressure fluctuations during the formation of an FIA and reequilibration after trapping.

Fluid inclusions containing H_2O-CO_2-NaCl are common in many geologic environments and knowing the salinity of these inclusions is important to interpret PVTX properties of the fluids. A technique that combines Raman spectroscopy and microthermometry of individual inclusions was developed to determine the salinity of these inclusions. In order to determine the salinity, the pressure and temperature within the inclusion must be known. The pressure within the inclusions is determined using the splitting in the Fermi diad of the Raman spectra of the CO_2 at the clathrate melting temperature. Applying the technique with to synthetic fluid inclusions with known salinity suggests that the technique is valid and useable to determine salinity of H_2O-CO_2-NaCl fluid inclusions with unknown salinity.

Acknowledgements

This dissertation was made possible with help and support from many people while working at Virginia Tech to whom I would like to express my deepest gratitude. First, I would like to thank my advisor, Dr. Robert J. Bodnar for his unselfish support over the years, for the thoughtful discussions and much wise counsel during the past five years of graduate life, not to forget the financial support accorded for the study. I would also like to thank Dr. Csaba Szabó from the Eötvös University, Budapest, Hungary for his support and for guiding my first steps into the mysteries of scientific research. I also thank J. Donald Rimstidt, Robert P. Lowell and Robert J. Tracy as members of my committee for help and discussions that improved the quality of my research. My gratitude goes also to T. James Reynolds who helped me see through the chaos of fluid inclusions in many samples. The departmental staff is thanked for their help without whom many things would be impossible to reach in the department. My special thanks go to Charles Farley whose help made possible many of the experimental work in the Fluids Research Laboratory. Daniel Smith also contributed to technical aspects of my experimental setups. Some of the samples for this study were provided by Daniel Kontak, James Student and Paul Spry. I would also like to thank my current and past colleagues in the Fluids Research Laboratory, with whom I shared many of the ups and downs of graduate life and who made office and laboratory work easier over the years: Tristan Azbej, Stephen Becker, Claudia Cannatelli, Rosario Esposito, Silvio Ferrero, Matt MacInnis, Daniel Moncada, Massimiliano Rolandi, and Rocky Severs. Members of the Hungarian Students Association at Virginia Tech contributed to recreation.

I thank my family back in Transylvania for their support and encouragmenet over the years.

Finally, I would like to express my deepest gratitudes to my wife Annamari for her support and help, for being always there when needed and for being the perfect teammate in life for the past nine years and many more to come.

Table of Contents

List of Tables

Chapter 1:

Chapter 2:

List of Figures

Chapter 1:

Chapter 2:

Chapter 3:

CHAPTER 1

An assessment of the precision of thermal history reconstruction based on fluid inclusions: The effect of fluid inclusion size

1.1. Introduction

Fluid inclusions trapped in minerals provide information on the temperature, pressure and fluid composition attending various geologic processes (Roedder, 1984). Over the years a standard methodology has been developed and accepted by the scientific community for the collection and interpretation of data from fluid inclusions (Hollister et al., 1981; Roedder, 1984; Shepherd et al., 1985; Goldstein and Reynolds, 1994; Goldstein, 2003). The first and most important step in the process is to identify a *Fluid Inclusion Assemblage* (FIA), defined as the most finely discriminated fluid inclusion trapping event that can be identified based on petrography (Goldstein & Reynolds, 1994; Goldstein, 2003). This definition implies that the fluid inclusions in the assemblage all trapped a fluid of the same composition *"at the same time"* and, by extension, at the same temperature and pressure (Bodnar, 2003a). The constraint that the fluid inclusions were trapped *"at the same time"* is relative and the absolute amount of time required to trap a fluid inclusion assemblage will depend on the environment of trapping (Brantley et al., 1990; Voigt and Brantley, 1991; Bodnar, 2003a). The amount of time required to trap the fluid inclusion assemblage may, in turn, affect the validity of the assumption that the fluid inclusions were all trapped at the same temperature and pressure. And, it should be emphasized that the trapping of fluid inclusions requires that host mineral is being precipitated to produce primary inclusions or that fractures are being sealed to trap secondary inclusions and these processes in turn suggest changing physical and/or chemical conditions in the fluid. Thus, the assumption of constant PTX trapping conditions must be viewed with caution.

With modern microscope heating and cooling stages, the homogenization temperature (T_h) of most fluid inclusions that homogenize to the liquid phase can be determined with a precision (reproducibility) of ±0.1 degrees Centigrade. The accuracy of T_h determinations varies with temperature, and is generally estimated to be about ±0.5% of the measured T_h, i.e., ±1 degree Centigrade for T_h = 200°C, ±2.5 degree Centigrade for T_h = 500°C, etc. The precision and

accuracy of T_h measurements for fluid inclusions that homogenize to the vapor phase is considerably poorer, owing to the difficulty of recognizing when the last amount of liquid wetting the inclusion walls has evaporated into the vapor phase (Bodnar et al., 1985; Sterner and Bodnar, 1991).

While the precision and accuracy of individual fluid inclusion measurements is well understood, few workers have discussed the precision and accuracy with which a geologic event or process can be constrained based on fluid inclusion studies. In this study we assume that a Fluid Inclusion Assemblage represents the finest (shortest time duration) geologic event that can be constrained using fluid inclusions. If the time duration of the event was such that all of the inclusions in the FIA were trapped at exactly the same PTX conditions, then all of the inclusions in the FIA should show identical microthermometric behavior, within the precision of the measurement. If the PTX conditions change during trapping of fluid inclusions, the effect of varying trapping conditions within an FIA on the microthermometric behavior of the FIA is related to how long it takes individual inclusions to become closed systems, relative to the rate of change of the PTX conditions.

Synthetic fluid inclusions trapped in the one-fluid-phase field (Sterner and Bodnar, 1984) are formed at a known and relatively constant temperature and pressure, and from a fluid of known and constant composition. Microthermometry of synthetic fluid inclusions often reveals T_h variations of about ± 1- 4 degrees Centigrade (Fig. 1.1), or one order of magnitude larger than the precision of the measurement for an individual inclusion (Bodnar and Sterner, 1985, 1987). The same range in T_h was observed in well-constrained natural FIAs where the inclusions are assumed to have been trapped at the same time (i.e., the same temperature and pressure). A question that this study addresses is whether these variations reflect real variations in the PTX trapping conditions, or if these variations might be due to other physical or chemical processes operating during trapping and/or homogenization in the laboratory.

1.2. Analytical methods

The samples used in this study are quartz containing synthetic fluid inclusions (Fig. 1.2a) (Sterner and Bodnar, 1984), and fluorite from the MVT deposits of the Cave-in-Rock fluorspar district, southern Illinois, that contains both primary and secondary natural fluid inclusions (Fig.

1.2b) (Richardson and Pinckney, 1984). The experimental procedure to produce synthetic fluid inclusions in quartz was described previously by Sterner and Bodnar (1984) and Bodnar and Sterner (1987), and, therefore, only the details relevant to this study are reported here. The synthetic fluid inclusions studied contain pure H_2O or 20 wt% KCl solutions and were trapped at 300 and 400°C and 100 to 500 MPa (Table 1). Sterner and Bodnar (1984) previously studied these samples to determine the PVT properties of H_2O and 20 wt% KCl solutions. The fluorite samples contain healed fractures decorated by abundant secondary fluid inclusions of varying sizes. The salinity of the inclusions is about 20 wt% NaCl equivalent, and they contain significant amounts of calcium. These secondary inclusions are rounded or negative crystal shaped, and do not show evidence for necking or any other re-equilibration processes. The fluorite samples also contain less abundant isolated, negative crystal-shaped primary inclusions.

Homogenization temperatures of the inclusions were determined with a USGS type gas-flow heating and cooling stage (Werre et al., 1979) mounted on either an Olympus BX 51 microscope equipped with a 40x objective (N.A. = 0.55) with 10x oculars, or a Leitz Orthoplan microscope using the same objective and 15x oculars. The stage was calibrated using pure H_2O synthetic fluid inclusions that homogenized by critical behavior at 374.1°C (Sterner and Bodnar, 1984). Previous studies (c.f., Bodnar et al. 1985; Sterner et al., 1988; Sterner and Bodnar, 1991) in this laboratory have shown that the accuracy of homogenization temperature measurements decreases with increasing temperature and ranges from ±0.1degrees Centigrade at room temperature to ±2.5 degrees Centigrade at 374°C. The precision (reproducibility) of T_h measurements is ±0.1 degrees Centigrade over this entire temperature range.

The size of each inclusion studied was determined by measuring the diameter of the spherical vapor bubble at room temperature, calculating the vapor bubble volume, and then using this information to determine the volume of the inclusion using the PVTX properties of the inclusion fluid and mass balance constraints (Bodnar, 1983). For example, a pure H_2O inclusion that homogenizes to the liquid phase at 250°C has a density of 0.79907 $g \bullet cm^{-1}$ (Haar et al., 1984). At room temperature (22°C), liquid H_2O has a density of 0.9975 $g \bullet cm^{-1}$. Thus, the liquid H_2O at 22°C occupies 80.1% of the volume that it did at 250°C (= 0.79907/0.99775). Therefore, at 22°C the inclusion will contain a vapor bubble that occupies 19.9 volume percent of the inclusion. If the spherical vapor bubble diameter at 22°C is 5 μm, then the bubble volume is 65.45 μm^3, and the inclusion volume is 328.9 μm^3. The vapor bubble diameters were determined by viewing the

inclusions on a high-resolution monitor and measuring the diameter using a millimeter scale. The monitors had previously been calibrated using a micrometer scale viewed through the microscope using the same conditions as was used to examine the inclusions. Two different microscopes were used during the course of this study. On one microscope (Leitz) the monitor calibration was 1 mm on the monitor equals 0.435 μm, and on the other (Olympus) 1 mm = 0.562 μm. Several fluid inclusions were measured in each FIA, ranging in size from the smallest inclusions for which a precise homogenization temperature could be measured (≈2 μm diameter) to the largest inclusions in the FIA. Vapor bubble diameters at room temperature for all the inclusions examined in this study ranged from several micrometers (<10) to about 0.5 μm. Smaller inclusions with even smaller bubbles were present in the samples but the bubble size could not be measured with sufficient accuracy.

1.3. Results and discussion

Results of the T_h measurements on synthetic fluid inclusions are shown in Table 1. Average T_h varies from 136 to 250°C for the different FIAs trapped under different P-T conditions. As an example, the distribution of T_h for one FIA in one sample is shown in histogram form in Figure 1.1. The inclusions were trapped at 300°C and the estimated temperature variation in the pressure vessel during the run was less than ±0.5 degrees Centigrade. As such, the expected variation in T_h should not exceed the variation in temperature of formation (±0.5 degrees Centigrade). Note that the actual variation in T_h depends on the P-T conditions of trapping of the inclusion owing to the changing slope of the isochores as a function of temperature, pressure and composition. For example, consider three different fluid inclusion assemblages, all trapped at different temperatures (T_t) but at the same pressure and having the same temperature (ΔT_t) variation during trapping (Fig. 1.3). Owing to the differing isochore slopes, the range in T_h for the FIA trapped at the lowest temperature will be larger than the range for the inclusions trapped at the higher temperature, even though the absolute variation in trapping temperature was the same for all three assemblages.

The observed total range in T_h (±1.5 degrees Centigrade) for the inclusions shown on Figure 1.1 is significantly larger than the estimated fluctuation in trapping temperature (±0.5 degree Centigrade). Also shown on Figure 1.1 is the precision of the T_h determination for individual

inclusions (±0.1 degree Centigrade). It is clear that the T_h range is larger than the precision of individual measurements. One possible explanation for the variation might be that the inclusions have reequilibrated after trapping (Bodnar, 2003c). However, the experimental runs were quenched isochorically to avoid subjecting the inclusions to pressure differential during the experiments, and the samples were not heated during cutting and polishing to prepare them for microthermometry. Additionally, previous tests in this laboratory confirm that, while the measured T_h of fluid inclusions will vary depending upon the position of the thermocouple relative to the inclusions, the relative difference in T_h between any two inclusions is independent of the thermocouple position. The accuracy of the T_h measurement is affected by the distance of the tip of the thermocouple from the inclusions, and in all cases in this study the tip of the thermocouple was within 100 μm of the inclusions being measured, resulting in errors of $\leq \pm$ 0.05 degrees Centigrade. These observations suggest that the measured T_h variation is not the result of measurement error or reequilibration of the fluid inclusions.

Upon further inspection, it is found that the temperature variation shown in Figure 1.1 is not random. Rather, when the homogenization temperature is plotted as a function of the fluid inclusion volume a remarkable correlation is observed (Fig. 1.4), with smaller inclusions homogenizing at lower temperatures compared to the larger inclusions in the same FIA. The correlation between T_h and inclusion volume is most obvious at lower temperatures (Fig. 1.4a-d) and becomes poorer with increasing temperature (Fig. 1.4e, f). At 250°C the correlation between inclusion size and T_h is no longer present (Fig. 1.4f). The relationship between inclusion volume and T_h was observed for both synthetic fluid inclusions containing pure H_2O (Fig. 1.4a) and 20 wt% KCl (Fig. 1.4b, d, e), and natural fluid inclusions in fluorite (Fig. 1.4c).

During heating of a liquid-rich inclusion (i.e., an inclusion that homogenizes by shrinking and disappearance of the vapor bubble at T_h) it is generally assumed that the bubble volume decreases continuously with increasing temperature. In practice, however, the bubble will shrink until its radius reaches the critical radius at which point the bubble will "blink out" and the inclusion will homogenize. Consider three fluid inclusions with identical compositions and densities, but varying sizes (volumes) (Fig. 1.5a). The volume percent vapor in the inclusions at room temperature is a function of the total density of the inclusions and the density of the liquid phase at room temperature. Because each inclusion has the same density, the volume percent vapor in every inclusion will be the same. As the inclusions are heated the vapor bubble in each

inclusion will decrease in size, but at any temperature the volume percent vapor in every inclusion will be identical. Thus, as the inclusions approach the homogenization temperature and the bubble size decreases, the absolute size (radius) of the bubble in the small inclusion will be less than the radius of the bubble in the larger inclusion, and the bubble in the smaller inclusion will reach the critical radius at a lower temperature compared to the bubble in the larger inclusion. The bubble in the smaller inclusion will "blink out", i.e., the inclusion will homogenize, at a lower temperature compared to the larger inclusion.

The existence of a bubble in a liquid can be described in terms of the surface free energy ($\Delta_f G_{(r)}$) of the bubble. The bubble can reduce its surface free energy by shrinking to reduce its surface area. However, as this happens the vapor pressure inside of the bubble increases and causes the bubble radius to increase until the surface free energy is balanced by the energy associated with the vapor inside of the bubble "pushing" outward (Fig. 1.5b). This situation results in a pressure differential across the bubble-liquid interface. The force across the liquid-vapor interface represents the surface tension of the system, and the relationship between pressure and surface tension is described by the Laplace equation (Loucks, 2000; de Gennes et al., 2004):

$$\Delta P = 2\sigma/r \tag{1}$$

where ΔP is the difference between the pressure of the vapor bubble and the confining pressure of the inclusion, σ is the surface tension of the solution, and r is the radius of the vapor bubble (Fig. 1.5b). Forming (or collapsing) a bubble with radius r is controlled by the Gibbs free energy change (ΔG_r) that is described by the following equation:

$$\Delta G_r = 4\pi r^2\sigma - (4/3)\pi r^3 \Delta P \tag{2}$$

where the first term on the right side of the equation represents the work done by the liquid in increasing its surface area by an amount corresponding to the surface area of the bubble (A = area of sphere = $4\pi r^2$). The second term on the right side of the equation is the PV work (V = volume of sphere = $4/3\pi r^3$) done by the liquid to decrease its volume by an amount equal to that of the bubble (Loucks, 2000). The "blinking out" of the bubble at homogenization occurs when

the bubble reaches the critical radius, r_c, and the bubble becomes unstable owing to the large pressure differential, ΔP, across the liquid-vapor interface. If r is replaced by the critical radius, r_c, in equation (1), and then entered into equation (2), this gives the variation of Gibbs free energy of a bubble with radius r relative to the smallest stable radius, r_c:

$$\Delta G_r = 4\pi r^2 \sigma[1 - 2r/3r_c)] \quad (3)$$

ΔG_r achieves its maximum value for $r = r_c$, and at this value

$$\Delta G_{rc} = (4/3)\pi r_c^2 \sigma \quad (4)$$

If the radius of vapor bubble becomes smaller than this critical radius, r_c, the bubble will instantly collapse to reduce its Gibbs free energy. The effect of surface tension on the collapse of a vapor bubble was previously demonstrated by numerical simulation (Atchley, 1988; Kuvshinov, 1991).

According to the above description the relation between the vapor bubble radius, vapor and liquid pressure and the surface tension controls the stability of the bubble, and, therefore, the homogenization of fluid inclusions. And, as described above, smaller inclusions achieve the critical bubble radius at a lower temperature compared to larger inclusions with the same density, resulting in a good correlation between inclusion volume and homogenization temperature, especially at lower temperatures. The diminished correlation between the fluid inclusion volume and T_h at higher temperatures can be explained by the temperature dependence of surface tension. The surface tension of pure H_2O decreases with increasing temperature (Fig. 1.6), reaching a value of zero at the critical point of water, 374.1°C, where the distinction between liquid and vapor disappears. As $\sigma \rightarrow 0$, $\Delta G_{rc} \rightarrow 0$ and the effect of bubble radius decreases.

Most natural fluid inclusions do not contain pure H_2O but rather contain various amounts of salts and gases (Roedder, 1984; Bodnar, 2003b; Diamond, 2003b). The surface tension of electrolyte solutions differs from that of pure H_2O (Weissenborn and Pugh, 1996; Jungwirth and Tobias, 2001; Edwards and Williams, 2006) and may affect the relationship between inclusion volume and homogenization temperature. Weissenborn and Pugh (1996) measured the surface tension of electrolyte solutions at various concentration ≤1 M, and compared the surface tension

of these solutions to that of the pure H_2O. Their results show that adding salt to H_2O increases the surface tension relative to pure H_2O (Fig. 1.7). They also observed that the increase in surface tension from divalent electrolytes ($CaCl_2$, $MgCl_2$) was about twice that for the monovalent electrolytes (NaCl, KCl, LiCl). The measurements were carried out at 24°C and the authors did not consider the temperature dependence of surface tension. However, it is generally known that the surface tension of aqueous solutions decreases with increasing the temperature (Palmer, 1976), just as it does for pure H_2O. Hence, fluid inclusions containing aqueous salt solutions should also show a decreasing correlation between inclusion volume and homogenization temperature, as evidenced by the results for synthetic fluid inclusions containing 20 wt% KCl solutions described above (Figs. 1.4b, d, e).

Chiquet et al. (2007) studied the surface tension of the CO_2-water system at different pressures and temperatures to test the feasibility of CO_2 storage in deep geological formations. Their results show that adding CO_2 to water generally decreases the surface tension compared to pure H_2O (Fig. 1.8). Over the temperature range 35° to 110°C the surface tension varied from about 45 to 25 mN/m – for comparison the surface tension of pure H_2O varies from about 72 to 57 mN/m over this same temperature range (see Fig. 1.6). They demonstrated that increasing CO_2 pressures to about 20 MPa decreases the surface tension to about 30 mN/m, and temperature increase has little effect. Above 20 MPa the surface tension is nearly independent of pressure and decreases slowly with increasing temperature. These workers also observed that adding a small amount of salt to the CO_2-H_2O system did not significantly affect the surface tension (Fig. 1.8). The presence of CH_4 also decreases the surface tension of water (Jennings et al., 1971; Sachs and Meyn, 1996), however, its effect is slightly less than that of CO_2 (Fig. 1.9). The results of these various studies show that the rate of surface tension decrease for gas-bearing systems is greatest at low to moderate pressures and becomes less sensitive to gas content at higher pressures, for both CH_4 and CO_2. For both gases, the surface tension decreases with increasing temperature. The effect of CH_4 and CO_2 on surface tension described above is consistent with observations of gas-bearing fluid inclusions. While we have not conducted careful studies of this effect, our experience suggests that gas-rich inclusions require smaller amounts of under-cooling (compared to gas-free inclusions) to re-nucleate the vapor bubble after homogenization, and this is consistent with a lower surface tension for the gas-bearing fluid system.

According to Equation (4), the critical radius for all of the fluid inclusions in an FIA should be the same because the surface tension is assumed to be constant (at a fixed temperature, pressure and composition). We have based our interpretation of the fluid inclusion size-dependence of the homogenization temperature (Fig. 1.4) on the assumption that the critical radius is the same for all inclusions in the FIA (see Fig. 1.5), and we may test this assumption using data obtained from fluid inclusions in this study. The total range in homogenization temperature for one synthetic fluid inclusion FIA containing pure H_2O inclusions was 1.4 degrees Centigrade (from 135.9° to 137.3°C; Fig. 1.4a). The density of liquid H_2O at 135.9°C is 0.92982 g•cm^{-1}, and the density at 137.3°C is 0.92861 g•cm^{-1}. The observed range in homogenization temperatures corresponds to a range in the apparent density of the fluid inclusions of about 0.15%, and the percent change in density as a function of inclusion volume has been plotted on Figure 1.10. If we assume that at homogenization the largest inclusion in this FIA contains a bubble with a volume of 0.5 μm^3 (corresponding to a bubble diameter of ≈1 μm), the corrected or "true" density of the inclusion would be 0.92841 g•cm^{-1}, which corresponds to a "true" homogenization temperature of 137.4°C (Haar et al., 1984).

If we now assume that the critical radius of the vapor bubble is constant (= 0.5 μm) and independent of inclusion size and that all inclusions in the FIA homogenize when the bubble radius reaches this value, we can then estimate the effect of this bubble on the fluid inclusion density at homogenization for all of the inclusions in this FIA. For example, one inclusion in this FIA homogenized at 136.8°C and had a vapor bubble radius at room temperature of 1.4 μm, corresponding to a total inclusion volume of 170.4 μm^3. If this inclusion contained a vapor bubble with a volume of 0.5 μm^3 that "blinked out" at the homogenization temperature and if the "true" density of this inclusion was the same as that of the other inclusions in the FIA, i.e., 0.92841 g•cm^{-1}, then the apparent density would be 0.93115 g•cm^{-1}. This density corresponds to a homogenization temperature of about 134.1°C (Haar et al., 1984). The density of this inclusion, calculated assuming that the vapor bubble critical radius at homogenization was the same as the critical radius for the bubble in the largest inclusion in the FIA, is 0.294% larger than the true density and ≈44 times greater than the density based on the measured homogenization temperature. The relationship between inclusion volume and the change in density required if the critical bubble radius is identical in all inclusions is shown in Figure 1.10. Clearly, the measured homogenization temperatures are not consistent with the interpretation that the critical radius is

constant for all of the inclusions in the FIA. In other words, the density variation predicted by the measured homogenization temperatures is significantly less than that estimated based on a constant critical radius, and the difference increases with decreasing inclusion volume.

One explanation for the trend and the magnitude of the T_h and density variation as a function of inclusion volume is that the critical radius varies with the inclusion size, i.e., is smaller in smaller inclusions. Alternatively, the data could also be explained if the surface tension is a function of inclusion size.

To test the hypothesis that the critical radius varies with inclusion size we have to examine Equation (1) more carefully. Based on Equation (1) if we can define ΔP, and r is substituted with r_c, then the critical radius r_c can be calculated. ΔP represents the pressure difference between the pressure of the vapor bubble and confining pressure in the inclusion according to the following equation:

$$\Delta P = P_V - P_i \tag{5}$$

where P_V is the vapor pressure of the fluid along the L-V curve and P_L is defined as the pressure along the metastable extension of the isochore defined by the true T_h of the inclusion, according to Figure 1.11.

Figure 1.11 showing a segment of a phase diagram for a two-phase liquid vapor fluid inclusion in the P-T field. The L-V curve is the P-T path along which liquid-vapor inclusions follows as the inclusion is heated and defined by a slope of $(dP/dT)_L$. When the inclusion is homogenized (in this case to the liquid phase) the P-T path that the inclusion follows is the isochore corresponding to T_h with a slope of $(dP/dT)_i$. When the temperature is increased both the P_V and P_i increase and ΔP decreases. As P_V follows the slope of the L-V curve and P_i follows the slope of the isochore with the temperature change, ΔP can be describe based on the following equation:

$$\Delta P = [(dP/dT)_i - (dP/dT)_L] \times (T_{h,\,true} - T_{h,\,obs}) \tag{6}$$

where $T_{h,\,true}$ represents the true homogenization temperature at which, theoretically, all fluid inclusions within an FIA should homogenize, and $T_{h,\,obs}$ represents the observed homogenization temperature.

Based on this if the Laplace equation (1) is modified by ΔP and r substituted as describe above, the r_c can be calculated as follows:

$$r_c = \frac{2\sigma}{(dP/dT)_i-(dP/dT)_L]\times(T_{h,\,true}-T_{h,\,obs})} \tag{7}$$

Based on equation (7), and if we know how the volume of the vapor bubble is changing within a fluid inclusion in function of temperature, we can determine the temperature at which the vapor bubble will reach the critical radius r_c, and how the r_c is varying based on varying inclusion volumes. For example, we assume that the true homogenization temperature of H_2O fluid inclusions within an FIA is 150°C. At this temperature the mass of the inclusion can be calculated as the product of the density of H_2O at T_h and the volume of the inclusion. Knowing the mass of the H_2O in the inclusion the volume of the vapor bubble can be determined at any temperature as follows:

$$M(H_2O)_I = M(H_2O)_L + M(H_2O)_V \tag{8}$$

$$M(H_2O)_L = V_L\rho_L \tag{9}$$

$$M(H_2O)_V = V_V\rho_V \tag{10}$$

$$V_L + V_V = V_I \tag{11}$$

$$V_L = V_I - V_V \tag{12}$$

where $M(H_2O)$ is the mass of H_2O, V is the volume, ρ is density and the subscriptions represent the inclusion (I), liquid (L), and vapor (V), respectively.

If equation (12) is substituted in equation (10) and then equations (10) and (9) are substituted into equation (8) results the follow:

$$M(H_2O)_i = (V_i - V_V)\rho_L + V_V\rho_V \quad (14)$$

Solving for equation (14) results the volume of the vapor bubble in the inclusion in function of the inclusion volume according to the following equation:

$$V_V = \frac{-\rho_L+\rho_V}{M(H_2O)_i - \rho_L V_i} \quad (15)$$

The calculations were repeated at different temperatures between room temperature and the true homogenization temperature and the change in the volume of the vapor phase is determined as the inclusion is heated and the homogenization temperature is approached. Assuming a spherical vapor bubble the radius of the bubble can be calculated:

$$r = V_V/(4/3)\pi \quad (16)$$

The results of the calculations for different fluid inclusion volumes are shown on Figure 1.12. The figure illustrates that at low temperatures the decrease of the radius is slow over a specific temperature increment and as the temperature approaches the true homogenization temperature the radius decreases considerably more over the same temperature increment. On Figure 1.12 is also shown the hyperbolic function of the critical radius calculated based on equation (7) as a function of the difference between the true and observed homogenization temperatures. The intersection of the critical radius curve and the curve of the vapor radius change with temperature results the possible homogenization temperatures.

Based on Figures 1.11 and 1.12 the critical bubble radius of fluid inclusions is varying as a function of the inclusion volume. As the inclusions are heated the vapor pressure and the confining pressure in the inclusion increase, and the pressure difference decreases as the radius of the vapor bubble decreases. At a certain temperature the bubble radius reaches a size where the bubble cannot maintain the built-up pressure difference and collapses, this point results the observed homogenization temperature. For a true homogenization temperature of 150°C the critical radii calculated as describe above vary about an order of magnitude from about 0.1 to 3.0 μm for 145.0 to 149.9°C observed homogenization temperature range. As the critical radius is

smaller for smaller inclusion, and the critical pressure difference is larger for smaller inclusions, the small inclusions will homogenize at a lower temperature then the large inclusions within the same FIA.

In the larger inclusions it was possible to observe the vapor bubble all the way to the homogenization temperature (Fig. 1.13). However, in the smallest inclusions the vapor bubble became too small to observe well before homogenization was achieved. For these inclusions, the homogenization temperature was determined using the cycling technique whereby the inclusions were heated in 0.1 degree Centigrade increments after the bubble was no longer resolvable, and then cooling the sample to determine if the bubble grew back immediately (homogenization not achieved) or if the inclusion had to be cooled by some tens of degrees before the bubble "popped" back (homogenization achieved). Because it was possible to resolve bubbles as small as about 0.1-0.3 μm diameter, and because the bubbles could not be resolved in the smallest inclusions, it is likely that the critical radius is a function of the inclusion size, and that the decrease in critical bubble size as a function of inclusion volume shown on Figure 1.12 supported by this observation. Several workers have determined the critical bubble radius for various fluid systems (Atchley, 1988; Kuvshinov, 1991), and they range from 0.01 to 3.0 μm.

The critical bubble radius affects the pressure differential across the liquid-vapor interface according to equation (1). Assuming that the critical radius for the inclusions studied here is less than about 1 μm, we can estimate the pressure differential at the moment of homogenization. As shown on Figure 1.14, the critical radius varies from essentially zero at the critical temperature where the surface tension becomes zero, to ≈0.1 to 10 MPa at lower temperatures. For all critical radius values the pressure differential increases with decreasing temperature (increasing surface tension). At a given temperature, the pressure differential increases with decreasing critical bubble radius.

Equation (4) describes the relationship between the Gibbs free energy change associated with the growth or shrinkage of a vapor bubble as a function of the critical bubble radius, r_c, surface tension of the fluid and the pressure differential across the liquid-vapor interface. When $r = r_c$, the Gibbs free energy achieves a maximum value. If $r < r_c$ the bubble will immediately collapse to lower its surface free energy; if $r > r_c$ the bubble will continue to grow to lower its surface free energy (Loucks, 2000). As noted above, the critical radius observed in fluid inclusions in this study is ≤1 μm – it is not possible to determine a lower limit for r_c but is likely to be greater

than 0.01 μm (Atchley, 1988). The Gibbs surface free energy associated with the growth and collapse of vapor bubbles in pure H_2O has been calculated assuming critical radii ranging from 0.01 to 1 μm, and the results are shown on Figure 1.15. For each critical radius the surface free energy associated with the critical radius decreases with increasing temperature, reflecting the decrease in surface tension with increasing temperature. Additionally, for any temperature, the maximum surface free energy at the critical radius decreases with decreasing critical radius.

1.4. Summary

Homogenization temperatures of synthetic fluid inclusions show a systematic variation as a function of inclusion volume (size). Within the same FIA, small fluid inclusions homogenize at slightly lower temperature than larger inclusions. This behavior contradicts the generally-held belief that fluid inclusions trapped at the same temperature (and pressure, and having the same composition) should have the same T_h. The size dependency documented for synthetic fluid inclusions was also observed in natural fluid inclusions in fluorite. The size dependency can be explained by the Laplace equation that relates vapor and liquid pressures to the surface tension of the liquid-vapor interface and the radius of the vapor bubble. During heating of the fluid inclusion the vapor bubble is continuously reduced in size, increasing the vapor pressure within the bubble. The bubble reaches a critical radius at which the pressure difference causes the bubble to collapse, and homogenization of the inclusion occurs by "blinking out" of the bubble. The size dependency of T_h decreases with increasing temperature and is not observed for homogenization temperatures higher than about 230°C. This is expected as the surface tension decreases with increasing temperature, allowing the bubble to collapse with a lower pressure differential across the liquid-vapor interface. The observed relationship between T_h and inclusion volume requires that the critical radius of the vapor bubble cannot remain constant but must decrease with decreasing inclusion volume to produce the observed densities. At a given temperature, electrolyte solutions show higher surface tension, while gas-rich solutions show lower surface tension relative to that of pure H_2O. In both cases, the surface tension decreases with increasing temperature.

Results of this study suggest that homogenization temperatures of fluid inclusions may vary by a few degrees, even when the inclusions are trapped at exactly the same temperature and

pressure and from a fluid of the same composition. In most fluid inclusion studies this variation in T_h is sufficiently small that it can be ignored (and would likely not be recognized in most studies). However, the fluid inclusion size effect is most pronounced at low temperatures and should be considered for low temperature, diagenetic environments (Goldstein and Reynolds, 1994; Goldstein, 2003). Similarly, the synthetic fluid inclusion technique has become an acceptable and widely used technique to determine PVTX properties of fluids over a wide range of PTX conditions. In such studies, homogenization temperature differences of a few degrees may be significant, and the homogenization temperature of the largest inclusion in the FIA will most closely represent the correct homogenization temperature and fluid density.

REFERENCES

Atchley, A. A. (1988) The Blake threshold of a cavitation nucleus having a radius dependent surface tension. Journal of Acoustical Society of America, 85, p. 152-157.

Bodnar, R. J. (1983) A method to calculating fluid inclusion volumes based on vapor bubble diameters and P-V-T-X properties of fluid inclusions, Economic Geology, 78, p. 535-542.

Bodnar, R. J. (2003a) Introduction to fluid inclusions. In I. Samson, A. Anderson, and D. Marshall, Eds., Fluid Inclusions: Analysis and Interpretation, Mineralogical Association of Canada Short Course, 32, p. 1-8.

Bodnar, R. J. (2003b) Introduction to aqueous-electrolyte fluid inclusions. In I. Samson, A. Anderson, and D. Marshall, Eds., Fluid Inclusions: Analysis and Interpretation, Mineralogical Association of Canada Short Course, 32, p. 81-100.

Bodnar, R. J. (2003c) Re-equilibration of fluid inclusions. In I. Samson, A. Anderson, and D. Marshall, Eds., Fluid Inclusions: Analysis and Interpretation, Mineralogical Association of Canada Short Course, 32, p. 213-231.

Bodnar R. J. and Sterner S. M. (1985) Synthetic fluid inclusions in natural quartz II. Application to PVT studies. Geochimica et Cosmochimica Acta, 49, p. 1855-1859.

Bodnar, R. J. and Sterner, S. M. (1987) Synthetic fluid inclusions, In Ulmer, G.C., and Barnes, H.L., Eds., Hydrothermal experimental techniques, New York, Wiley-Interscience, p. 423–457.

Bodnar, R. J., Burnham, C. W. and Sterner, S. M. (1985) Synthetic fluid inclusions in natural quartz. III. Determination of phase equilibrium properties in the system H_2O-NaCl to 1000°C and 1500 bars, Geochimica and Cosmochimica Acta, 49, p. 1861-1873.

Brantley, S. L., Evans, B., Hickman, S. H. and Crerar, D. A. (1990) Healing of microcracks in quartz: implication for fluid flow, Geology, 18, p. 136-139.

Chiquet, P, Daridon, J.-L., Broseta, D. and Thibeau, S. (2007) CO_2/water interfacial tension under pressure and temperature conditions of CO_2 geologic storage. Energy Conservation and Management, 48, p. 736-744.

de Gennes, P.-G., Brochard-Wyart, F. and Quéré, D. (2004) Capillary and wetting phenomena: drops, bubbles, pearls, waves. Springer-Verlag, New York, 291 p.

Diamond, L. W. (2003b) Introduction to gas-bearing, aqueous fluid inclusions. In I. Samson, A. Anderson, and D. Marshall, Eds., Fluid Inclusions: Analysis and Interpretation, Mineralogical Association of Canada Short Course, 32, p. 101-158.

Edwards, S. A and Williams, D. R. M. (2006) Surface tension of electrolyte solutions: comparing the effect of ionic dispersion forces and solvation. Europhysics Letters, 74, p. 854-860.

Goldstein, R. H. (2003) Petrographic analysis of fluid inclusions. In Samson, I., Anderson, A. and Marshall, D. Eds., Fluid Inclusions: Analysis and Interpretation, Mineralogical Association of Canada Short Course, 32, p. 9-53.

Goldstein, R. H. and Reynolds, T. J. (1994) Systematics of fluid inclusions in diagenetic minerals. Society for Sedimentary Geology, SEPM Short Course, 31, 199 p.

Haar, L, Gallagher, J. S. and Kell, G. S. (1984) NBS/NRC Steam tables. Thermodynamic and transport properties and computer programs fro vapor and liquid states of water in SI units. Taylor and Francis, 320 p.

Hollister, L. S., Crawford, M. L., Roedder, E., Burruss, R. C., Spooner, E. T. C. and Touret, J. (1981) Practical aspects of microthermometry. In Hollister, L. S., Crawford, M. L., Eds., Fluid inclusions: applications to petrology, Mineralogical Association of Canada Short Course, 6, p. 13-38.

Jennings, H. Y. and Newman, G. H. (1971) The effect of temperature and pressure on the interfacial tension of water against methane-normal decane mixtures. Society of Petroleum Engineers Journal, 171-175.

Jungwirth, P. and Tobias, D. J. (2001) Molecular structure of salt solutions: a new view of the interface with implications for heterogeneous atmospheric chemistry. Journal of Physical Chemistry, 105, p. 10468-10472.

Kuvshinov, G. I. (1991) Effect of surface tension on the collapse of a cavitation bubble. Institute of Applied Physics, Academy of Science of the Belorussion SSR, Minsk. Translated from Inzhenerno-Fizicheskii Zhurnal, 60, p. 41-46

Loucks, R. R. (2000) Precise geothermometry on fluid inclusion populations that trapped mixtures of immiscible fluids. American Journal of Science, 300, p. 23-59.

Palmer, S. J. (1976) The effect of temperature on surface tension. Physics Education, 11, p. 119-120.

Richardson, C. K. and Pinckney, D. M. (1984) The chemical and thermal evolution of the fluids in the Cave-in-Rock fluorspar District, Illinois: mineralogy, paragenesis, and fluid inclusions. Economic Geology, 79, p. 1833-1856.

Roedder, E. (1984) Fluid inclusions. Mineralogical Society of America, Reviews in Mineralogy, 12, Ed. Ribbe, P. H. 646 p.

Sachs, W. and Meyn, V. (1995) Pressure and temperature dependence of the surface tension in the system natural gas/water. Principles of investigation and the first precise experimental data for pure methane/water at 25°C up to 46.8 MPa. Colloids and Surfaces A: Physicochemical and Engineering Aspects, 94, p. 291-301.

Shepherd, T. J., Rankin, A. H. and Alderton, D. H. M. (1985) A practical guide to fluid inclusion studies. Blackie & Son, Glasgow, UK, 239 p.

Sterner, S. M. and Bodnar, R. J. (1984) Synthetic fluid inclusions in natural quartz I. Compositional types synthesized and applications to experimental geochemistry. Geochimica et Cosmochimica Acta, 48, p. 2659-2668.

Sterner, S. M. and Bodnar, R. J. (1991) Synthetic fluid inclusions. X: Experimental determinations of P-V-T-X properties in the CO_2-H_2O system to 6 kb and 700°C, American Journal of Science, 291, p. 1-54.

Sterner, S. M., Hall, D. L. and Bodnar, R. J. (1988) Synthetic fluid inclusions. V. Solubility relations in the system NaCl-KCl-H_2O under vapor-saturated conditions, Geochimica et Cosmochimica Acta, 52, p. 989-1005.

Voigt, D.E. and Brantley, S. L. (1991) Inclusions in synthetic quartz. Journal of Crystal Growth, 113, p. 527-539.

Weissenborn, P. K. and Pugh, R. J. (1996) Surface tension of aqueous solutions of electrolytes: relationship with ion hydration, oxygen solubility, and bubble coalescence. Journal of Colloid and Interface Science, 184, p. 550-536.

Werre, R. W., Jr., Bodnar, R. J., Bethke, P. M. and Barton, P. B. (1979) A novel gas-flow fluid inclusion heating/freezing stage, Geological Society of America Program with Abstracts, 11, p. 539.

Tables

Table 1.1. Experimental conditions and T_h results for synthetic fluid inclusions

1	2	3	4	5
H_2O	300	300	135.9-137.6	136.7 (27)
	400	200	249.2-251.8	250.3 (29)
	400	300	208.1-212.8	210.0 (26)
	400	500	173.0-176.0	174.1 (43)
20 wt% KCl	300	100	228.5-231.8	230.7 (39)
	300	200	184.0-185.7	184.6 (31)
	300	300	140.5-143.5	141.7 (28)

(1) fluid composition; (2) formation temperature (°C);
(3) formation pressure (MPa); (4) T_h range (°C);
(5) average T_h (°C) and number of inclusions in parentheses

Figures

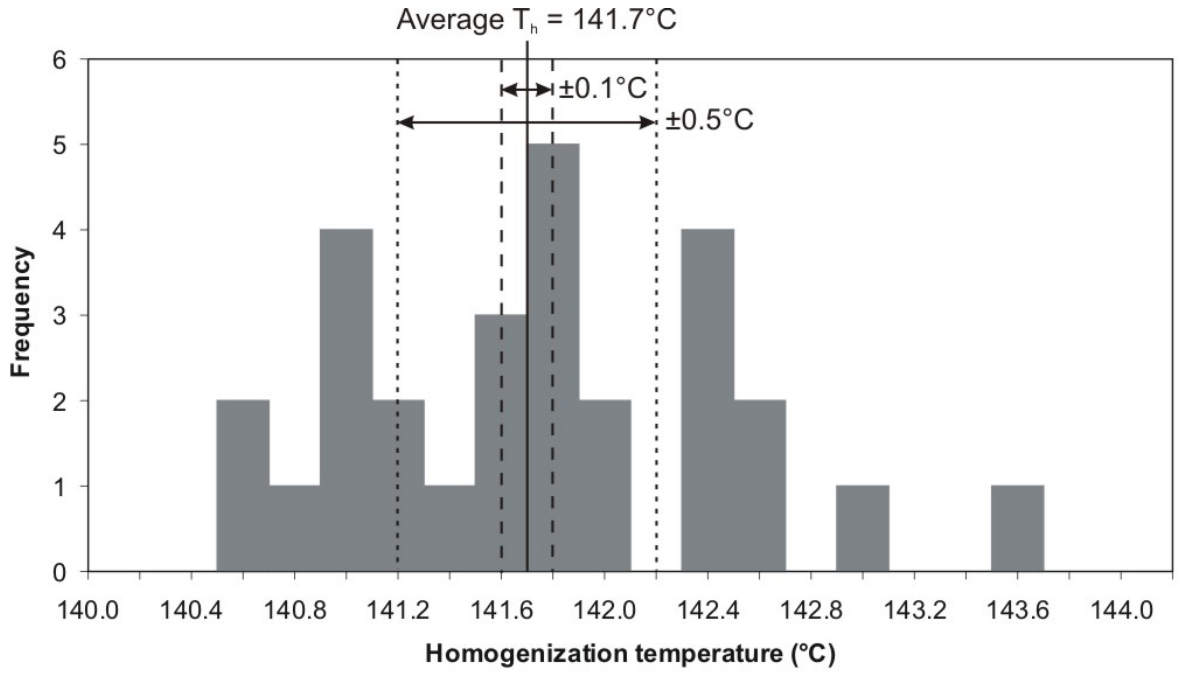

Figure 1.1 Histogram showing the distribution of homogenization temperatures of 28 synthetic fluid inclusions from a single fluid inclusion assemblage. The inclusions contain a 20 wt% KCl aqueous solution and were trapped at 300°C and 300 MPa (see Bodnar and Sterner, 1985, their Table 2). Also shown is the estimated temperature variation in the pressure vessel during inclusion trapping (±0.5°C) and the precision of the T_h measurement (±0.1°C).

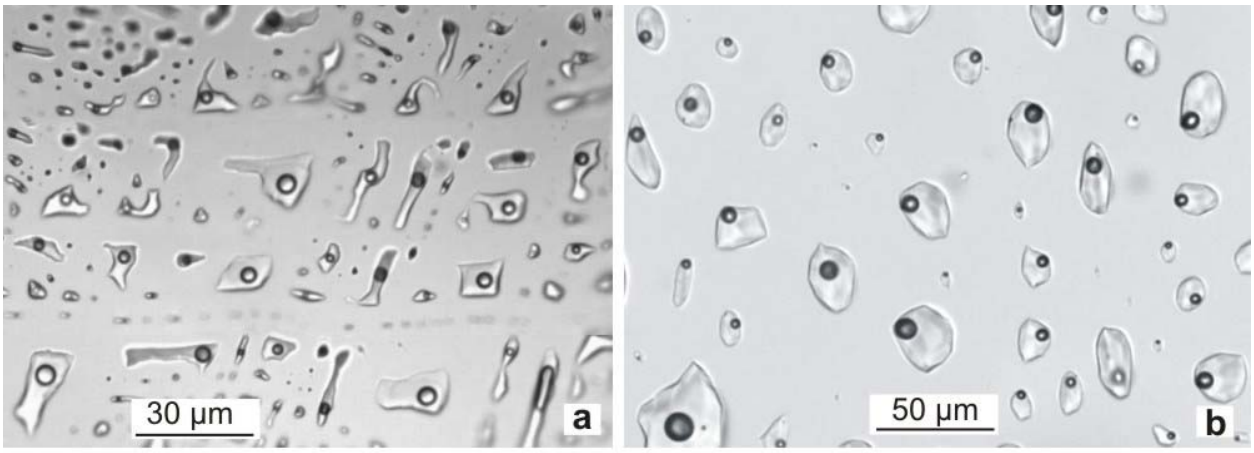

Figure 1.2. Photomicrographs of (a) synthetic fluid inclusions in quartz and (b) a secondary plane of fluid inclusions in fluorite from the Deardorff Mine, Cave in Rock District, Illinois.

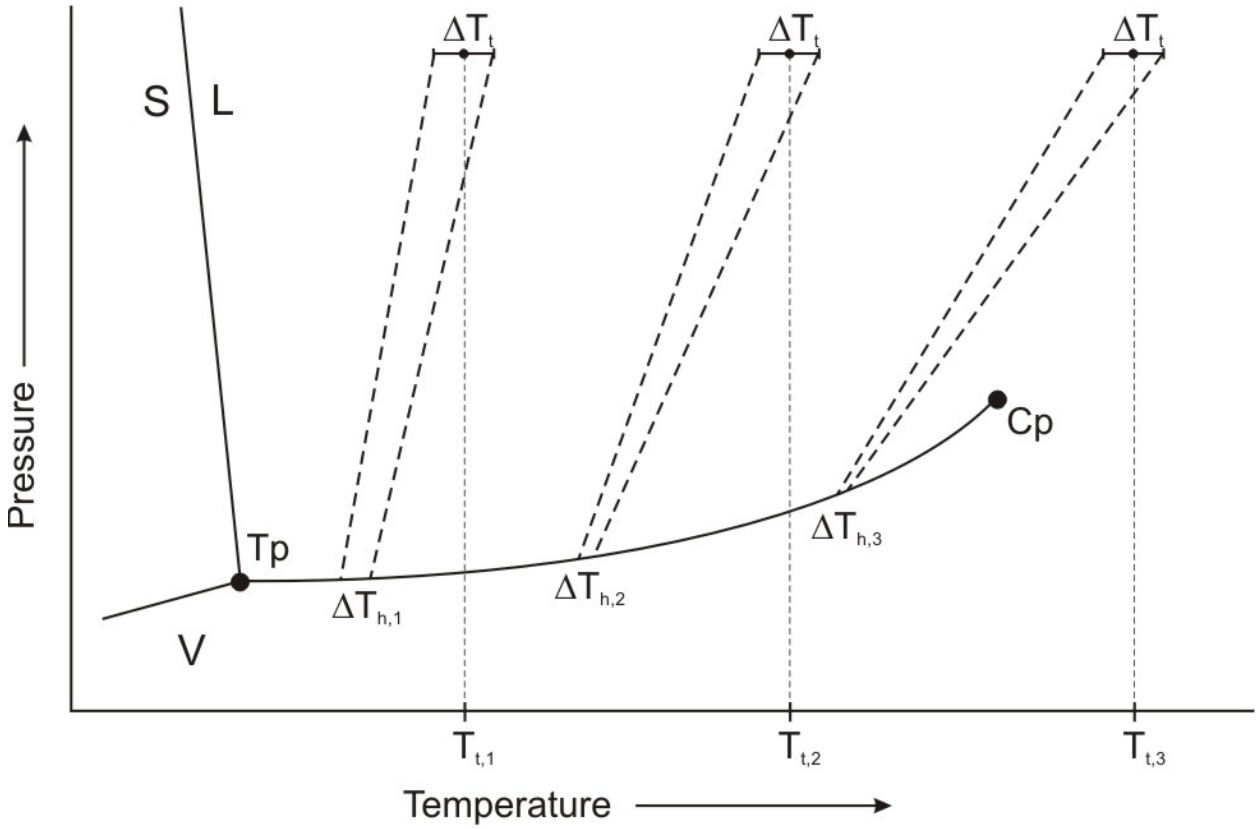

Figure 1.3. Schematic phase diagram of H_2O (solid lines) showing the isochores (dashed lines) for different fluid inclusion trapping temperatures at the same pressure. The range in trapping temperatures is identical for all three inclusions, but the range in T_h for the inclusions trapped at the lowest temperature is larger than the range for the inclusions trapped at the higher temperature due to the differing isochore slopes. S-solid; L-liquid; V-vapor; T_p-triple point; C_p-critical point; T_t-trapping temperature; T_h-homogenization temperature.

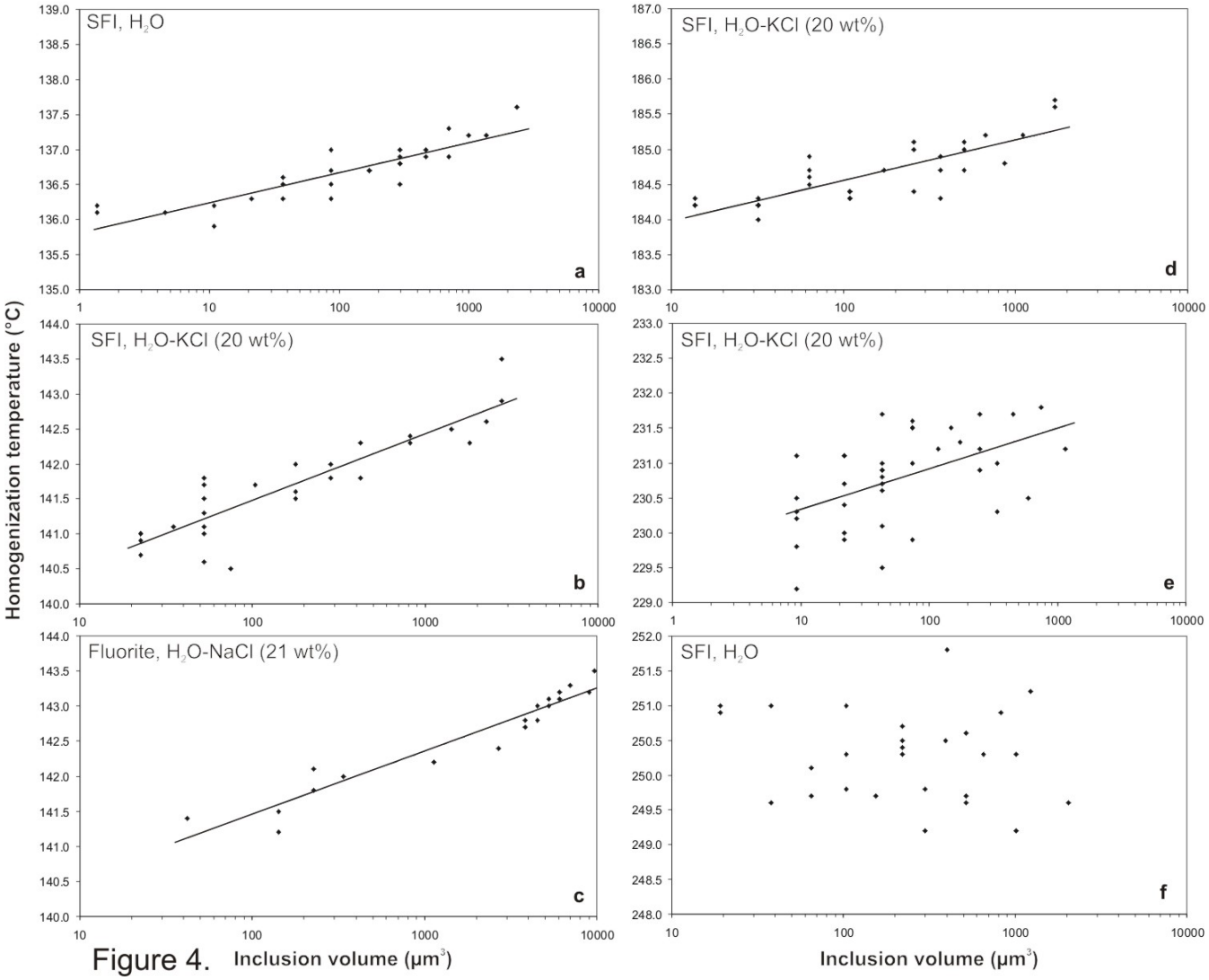

Figure 4.

Figure 1.4. Relationship between fluid inclusion volume and homogenization temperature for (a, f) pure H_2O synthetic fluid inclusions, (b, d, e) 20 wt% KCl synthetic fluid inclusions, (c) and natural fluid inclusions in fluorite.

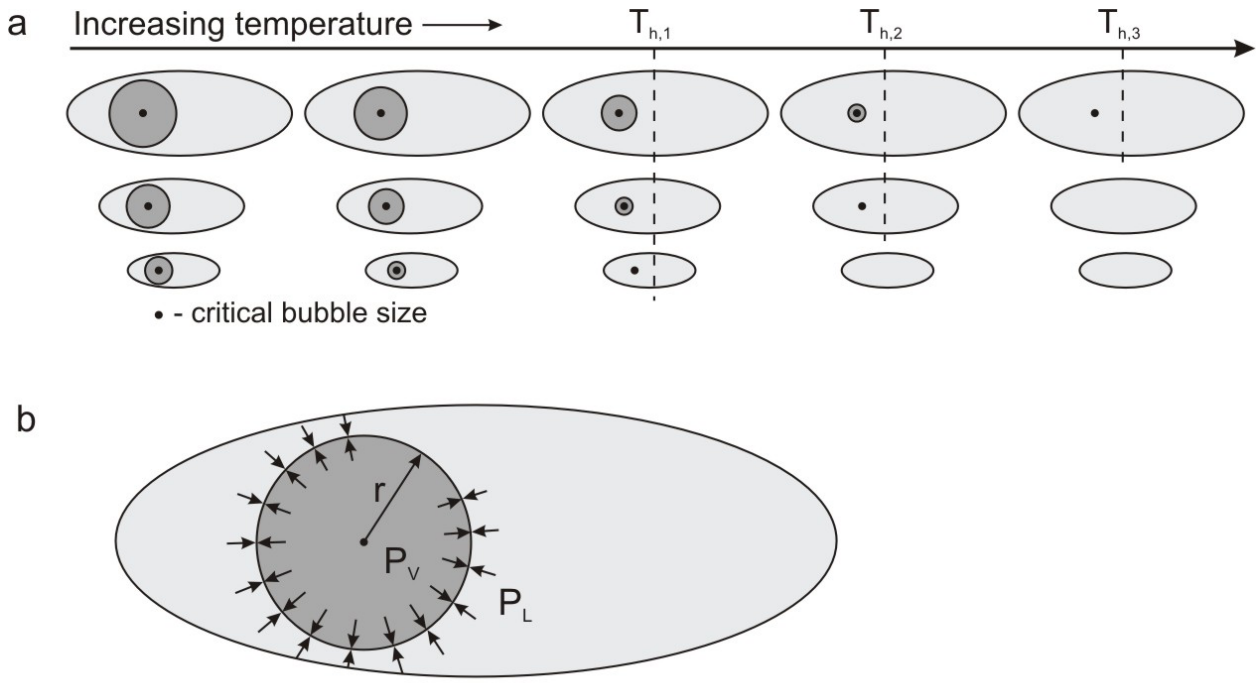

Figure 1.5. (a) Schematic representation of the relationship between inclusion volume, vapor bubble size and homogenization temperature for three liquid-rich inclusions with identical densities. As the inclusions are heated, the vapor bubble shrinks until the critical bubble radius necessary to maintain the bubble is reached. At that point the bubble "blinks out" and the inclusion homogenizes to liquid. The bubble in smaller inclusions reaches the critical radius at a lower temperature compared to bubbles in larger inclusions of the same density. (b) Relationship between vapor bubble radius (*r*), the pressure inside of a vapor bubble (P_V) and the pressure outside of the bubble (P_L) described by the Laplace equation.

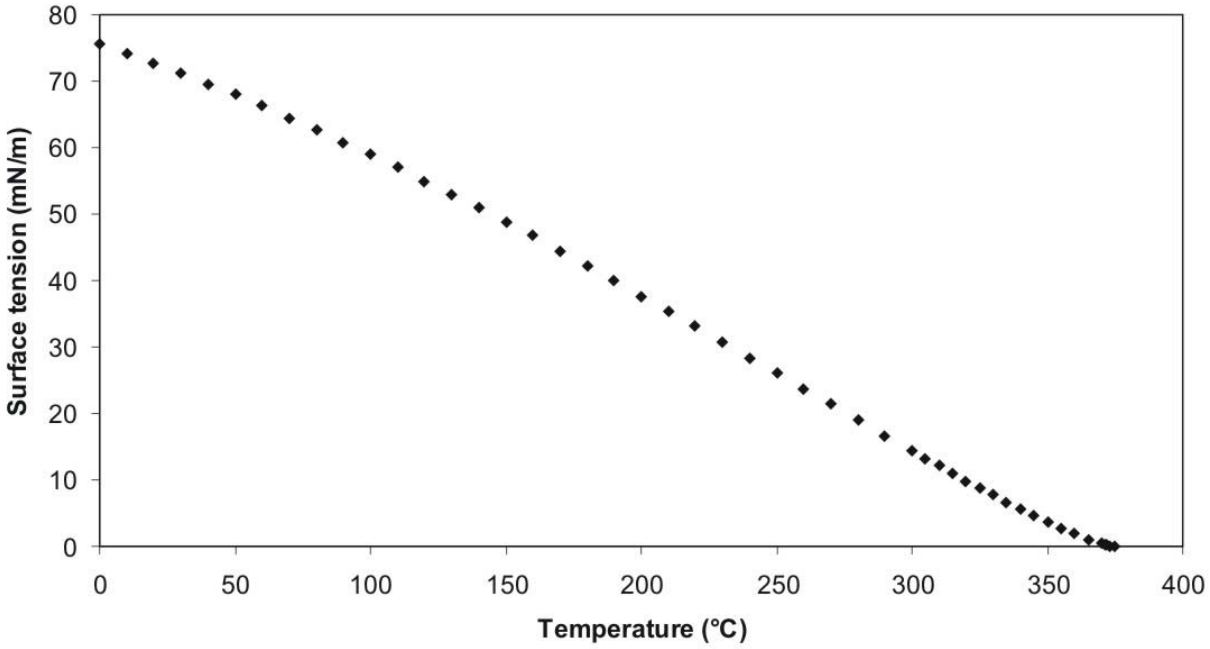

Figure 1.6. Temperature dependence of the surface tension of pure H_2O (data from Haar et al., 1984).

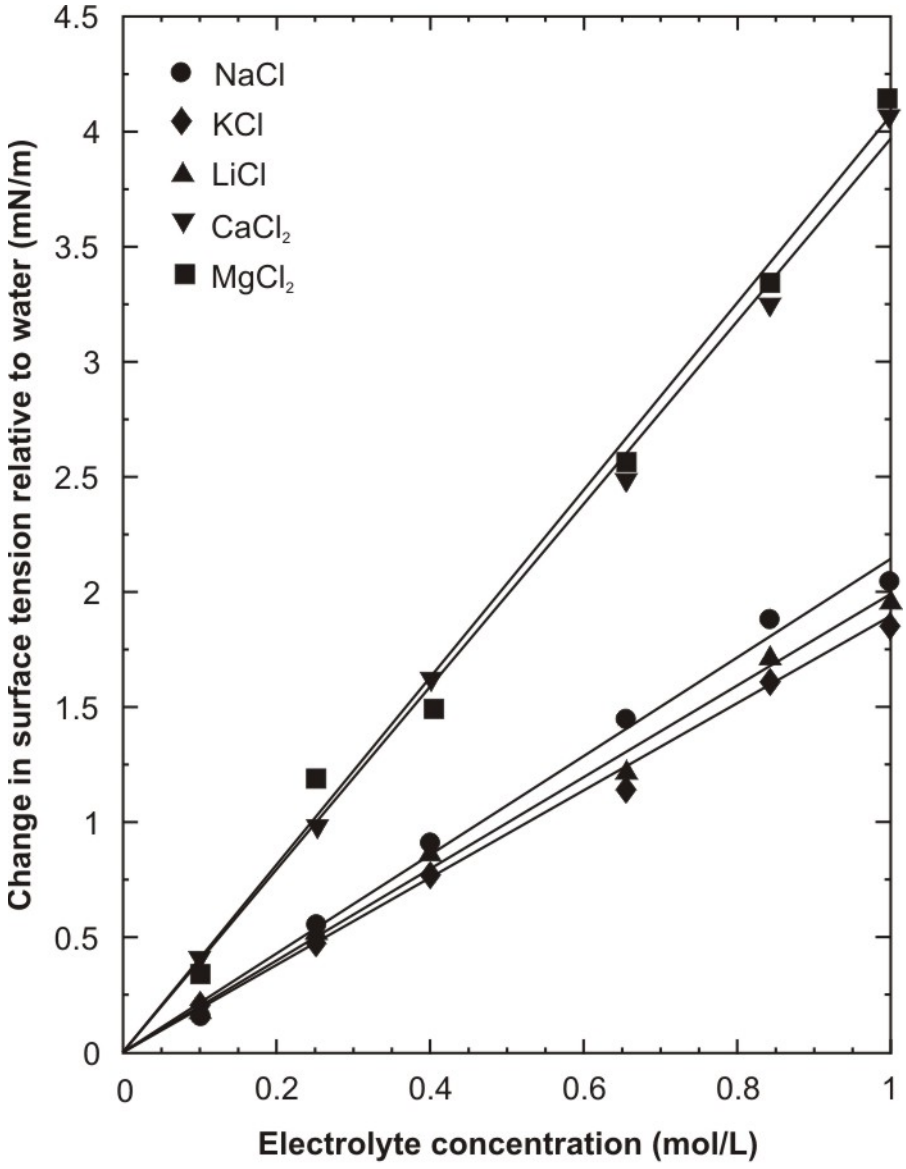

Figure 1.7. Effect of various electrolytes on the surface tension of aqueous solutions relative to pure H_2O (modified after Weissenborn and Pugh, 1996).

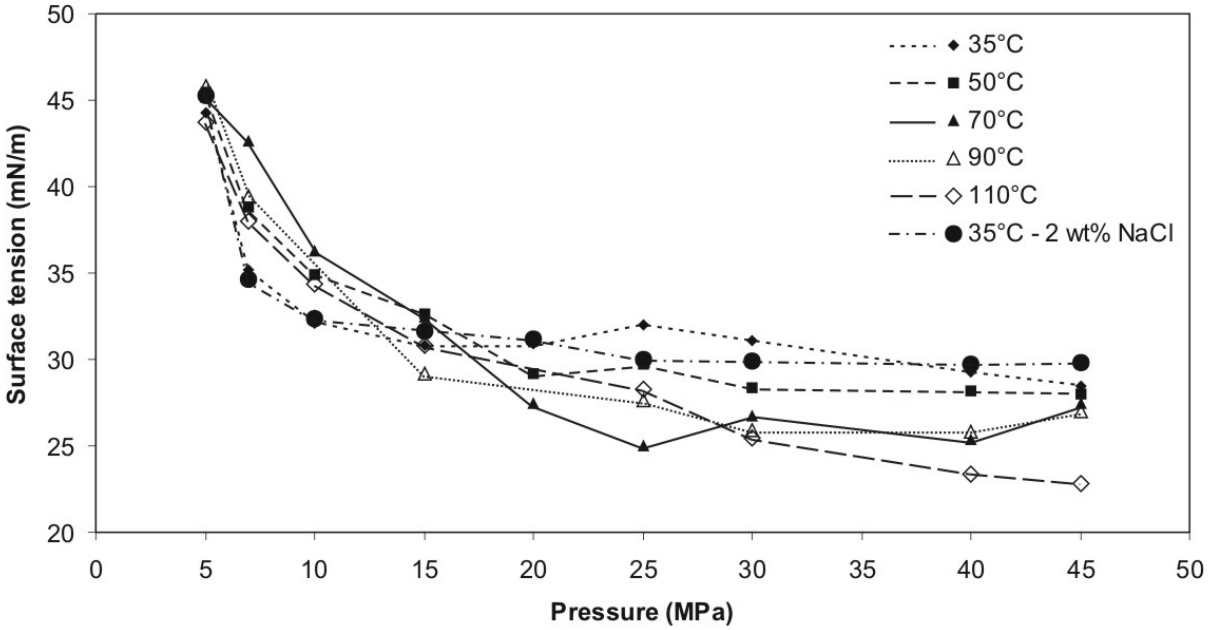

Figure 1.8. Variation in surface tension of CO_2-bearing aqueous solutions as a function of pressure and temperature (modified after Chiquet et al., 2007). The fluid is saturated in CO_2 at each P-T point.

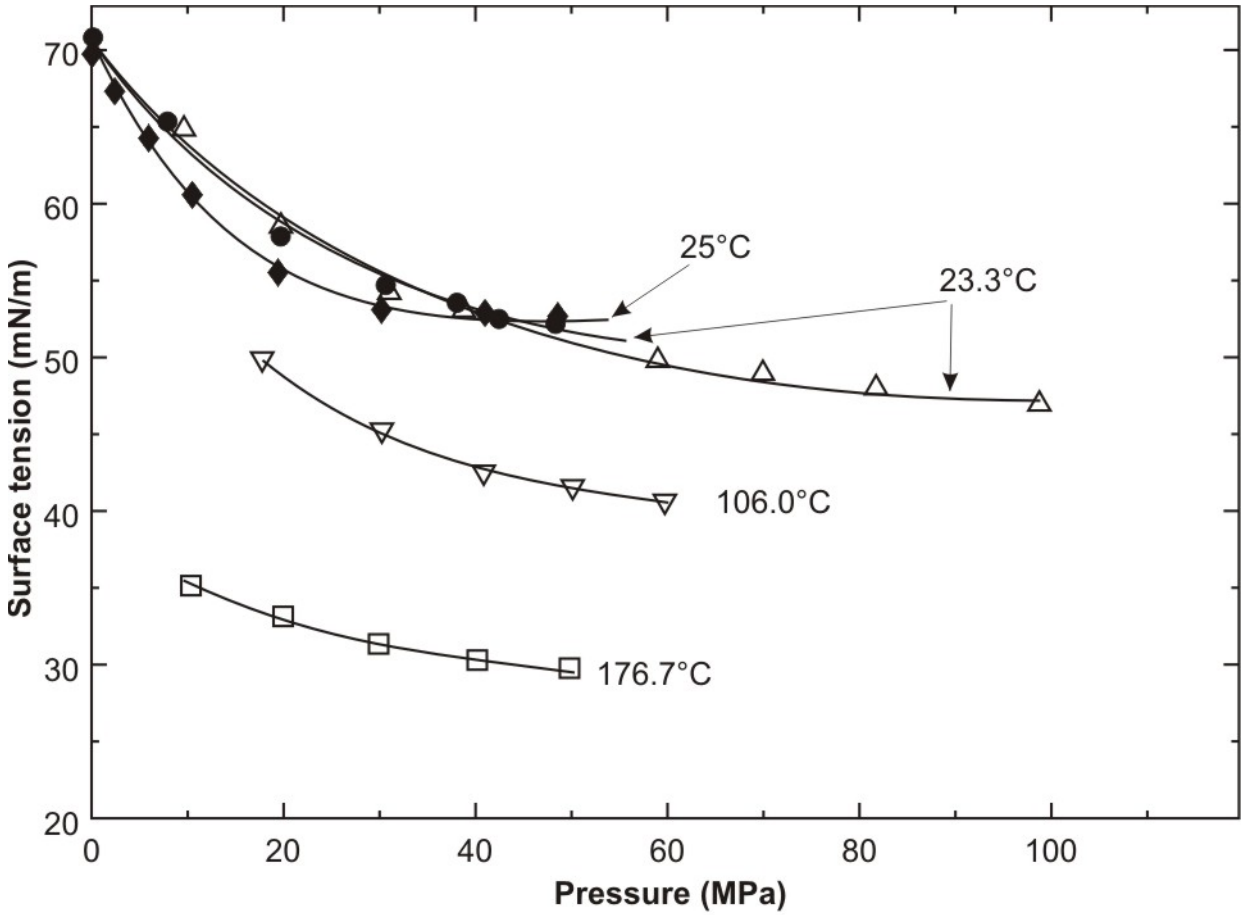

Figure 1.9. Variation in surface tension of CH_4-bearing aqueous solutions as a function of pressure and temperature [data from Jennings et al., 1971 (open symbols) and Sachs and Meyn, 1995 (filled symbols)]. The fluid is saturated in CH_4 at each P-T point and the CH_4 content of the liquid phase varies between $0.00021 < X_{CH4} < 0.0042$.

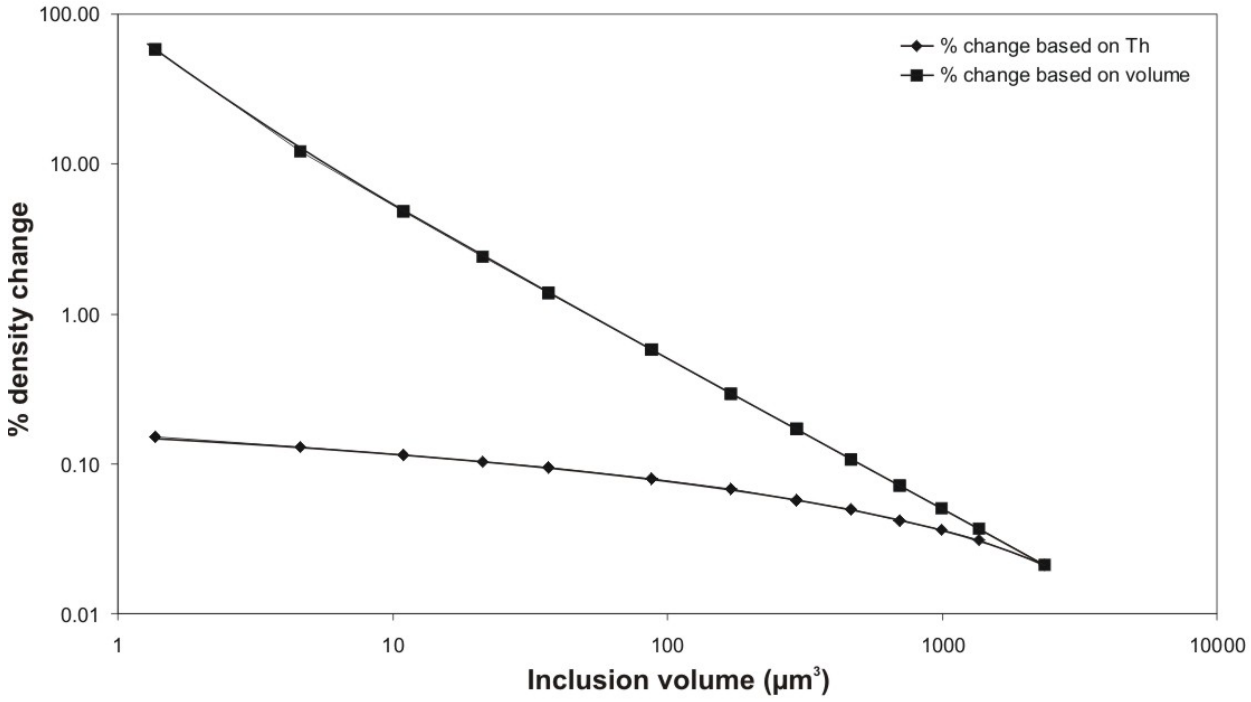

Figure 1.10. The relationship between inclusion volume and the change in density based on the homogenization temperature of the inclusions shown in Figure 4a. Also shown is the change in density that would result for these same inclusions assuming that the critical radius of the vapor bubble (= 0.5 μm) in all inclusions is the same as the critical radius for the largest inclusion.

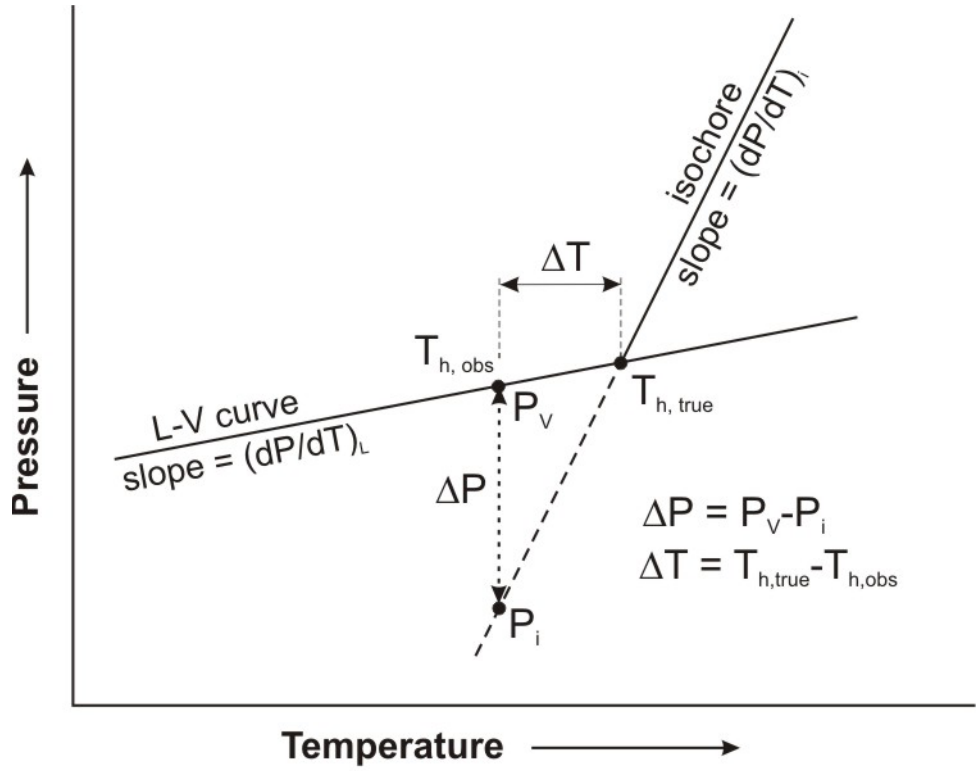

Figure 1.11. Sketch of the P-T filed of a homogenizing two-phase liquid-vapor fluid inclusion. As the inclusion approaches homogenization along the L-V curve the pressure difference between the vapor pressure and the confining pressure (as defined in the text) decreases. $T_{h,\,obs}$ – observed homogenization temperature; $T_{h,\,true}$ – true homogenization temperature.

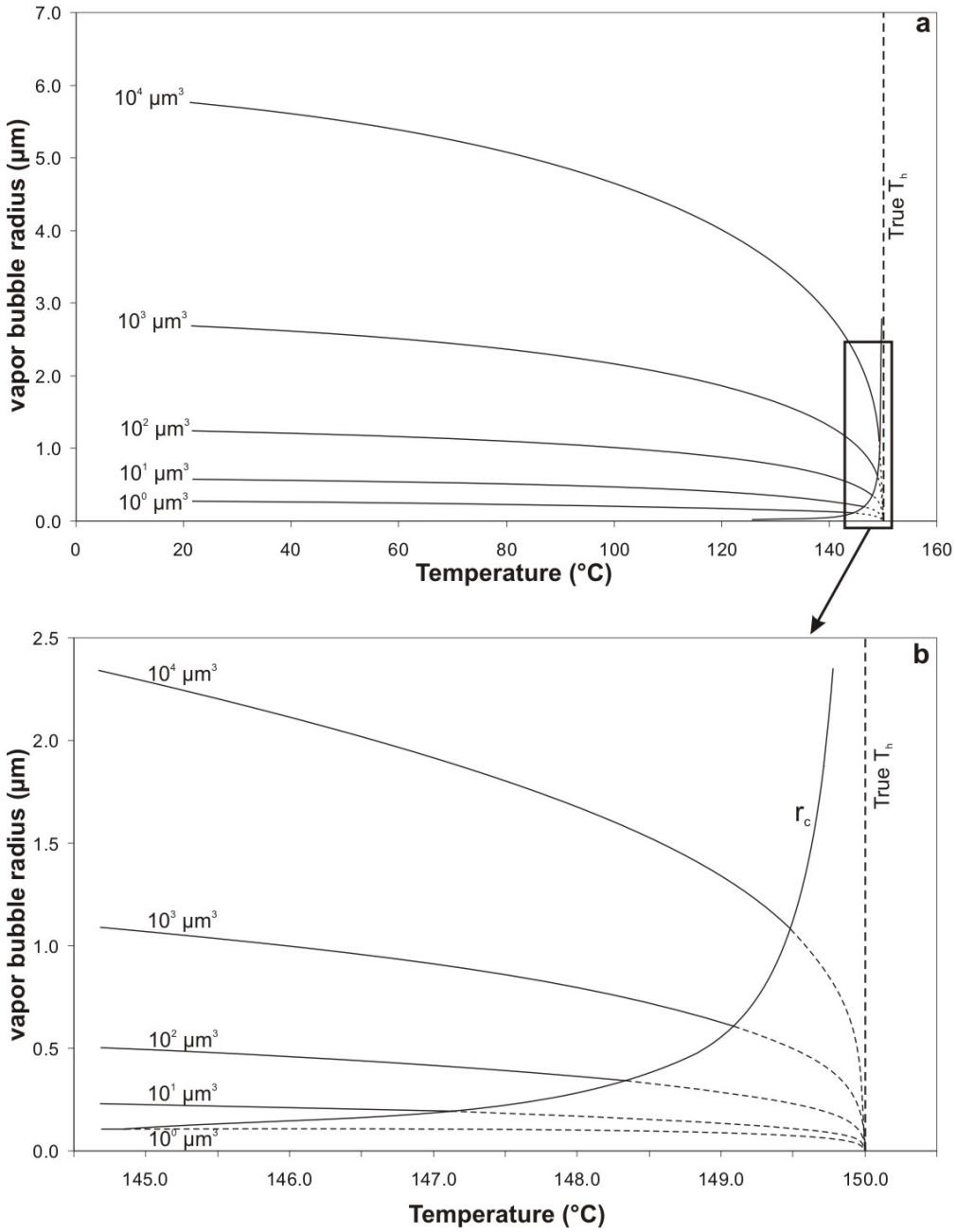

Figure 1.12. (a) The change in vapor bubble radius as the different sized fluid inclusions are heated. (b) A segment of the figure focusing on a temperature range that can be observed as homogenization temperature variation within a single synthetic FIA. The change in critical bubble radius as a function of inclusion volume is also shown, the intersections of the curves defining the critical bubble radii for the respective fluid inclusion volume.

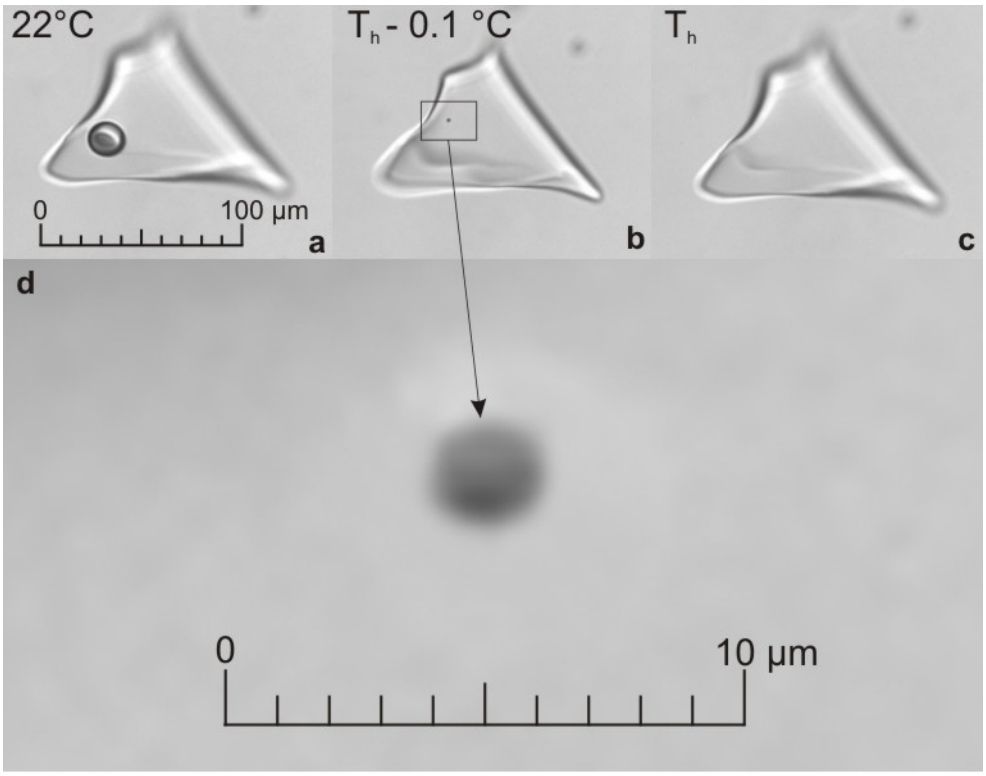

Figure 1.13. Photomicrograph of a synthetic fluid inclusion in quartz during microthermometry. The inclusion is shown (a) at room temperature, (b) at the moment before "blinking-out" (0.1 degree Centigrade below the homogenization temperature), and (c) at homogenization. An enlargement (d) of the area shown in (b) shows the vapor bubble immediately before homogenization.

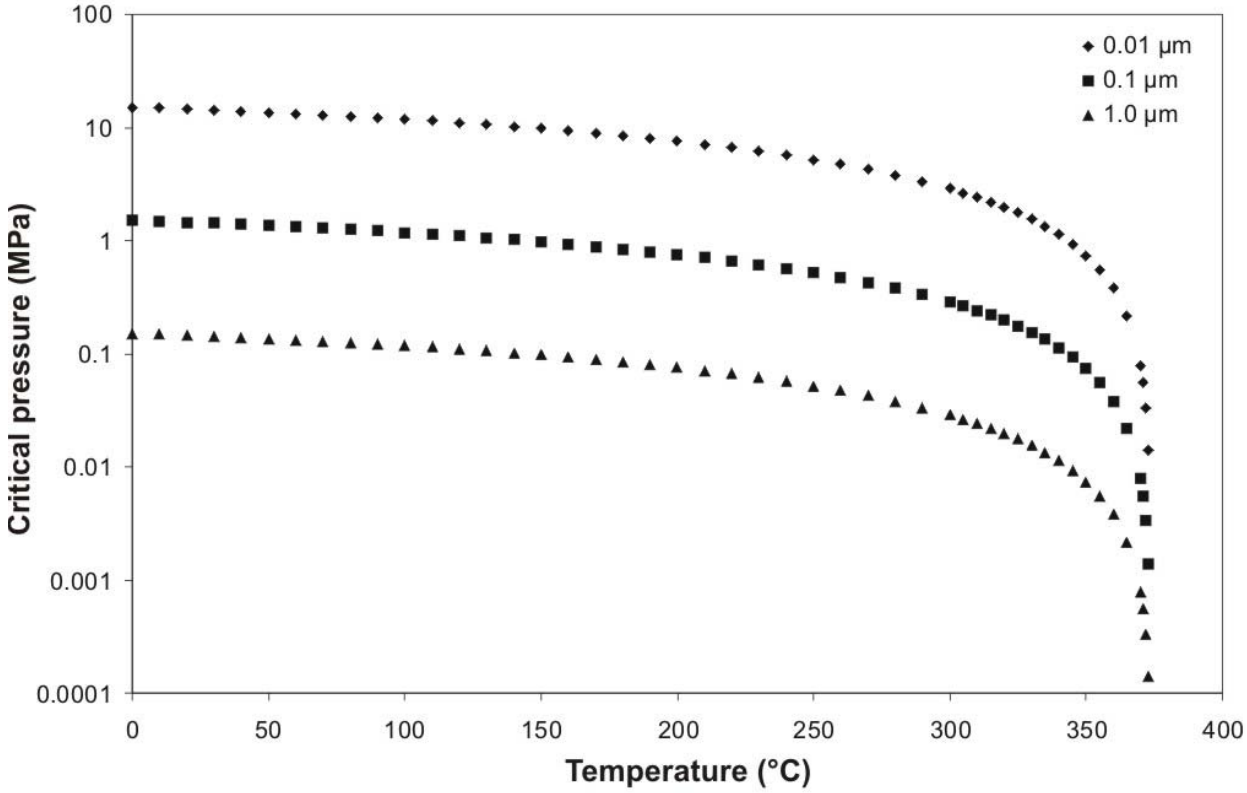

Figure 1.14. The effect of the critical bubble radius on the pressure differential across the liquid-vapor interface. For all critical bubble radii the pressure differential increases with decreasing temperature (increasing surface tension). At a given temperature, the pressure differential increases with decreasing critical bubble radius.

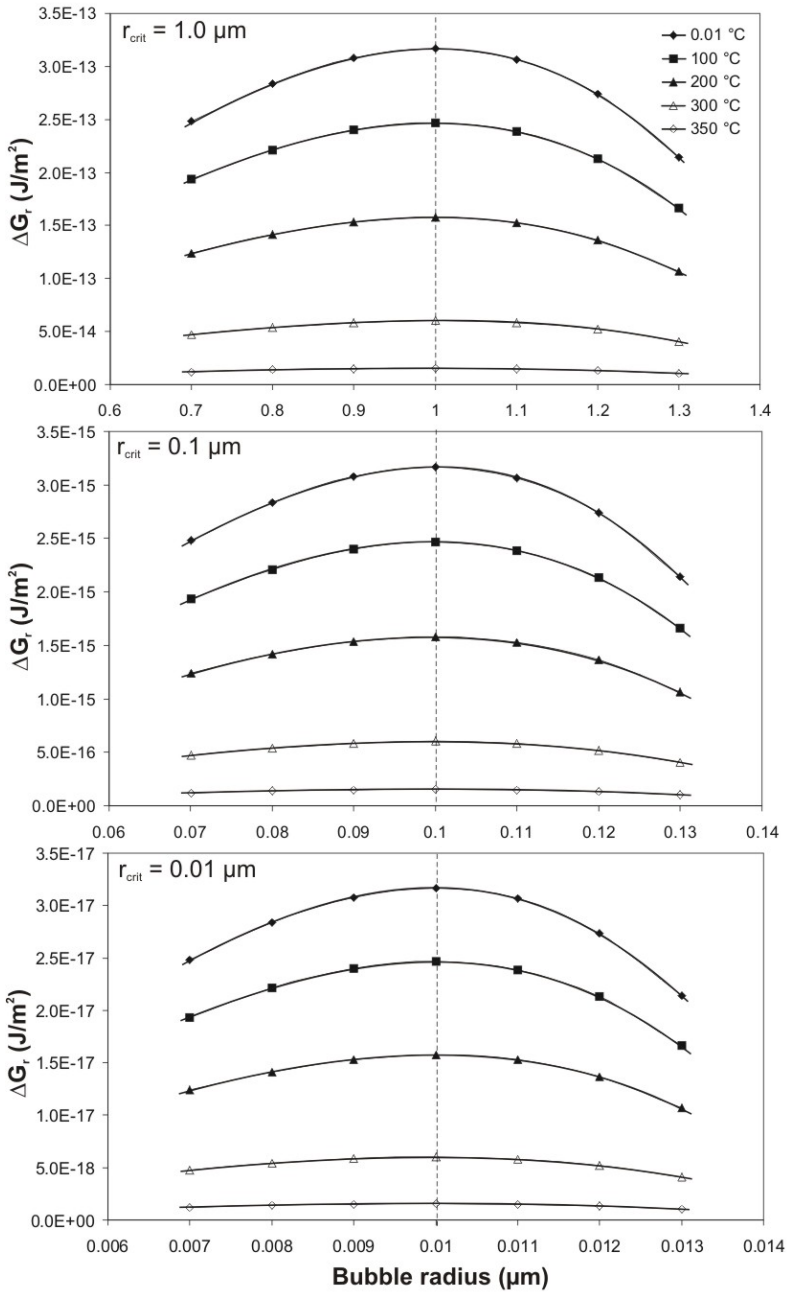

Figure 1.15. The relationship between the Gibbs free energy change associated with the growth or shrinkage of a vapor bubble as a function of the critical bubble radius (1.0 to 0.01 µm) described by Equation (4). The Gibbs free energy achieves a maximum value when $r = r_c$. If $r < r_c$ the bubble will immediately collapse to lower its surface free energy, whereas if $r > r_c$ the bubble will continue to grow to decrease its surface free energy.

CHAPTER 2

Thermal history reconstruction in magmatic, metamorphic and hydrothermal ore-forming environments using fluid inclusions

2.1. Introduction

Fluid inclusion microthermometric data provide information on the thermal history of geological events (Roedder, 1984; Goldstein and Reynolds, 1994; Bodnar, 2003a). In this study a "geological event" is defined as a discrete time step that can be identified and characterized using fluid inclusions, and these events are manifest as growth zones in crystals (Fig. 2.1a), or close-packed 3D clusters of inclusions (Fig. 2.1b), or as healed fractures (Fig. 2.1c). Fluid inclusions offer information on the pressure, temperature and composition (PTX) and origin of the fluids associated with formation of the host mineral and its subsequent history. Microthermometric data obtained from the inclusions represent the original trapping conditions only if the inclusions obey three simple rules or assumptions referred to as Roedder's Rules (Bodnar, 2003a). The assumptions state that: 1) the inclusion trapped a single, homogeneous fluid, 2) nothing is added to or lost from the inclusion after trapping, and 3) the inclusions are isochoric (the volume or density of the inclusions remained constant after the trapping). It is not possible to test whether or not an individual fluid inclusion, or group of paragenetically unrelated inclusions, obey Roedder's Rules. However, if the inclusions are contained within Fluid Inclusion Assemblages (FIAs) (Goldstein and Reynolds, 1994), then it is possible to test for conformity with Roedder's Rules.

Fluid Inclusion Assemblages (FIAs) are the most finely discriminated fluid inclusion trapping events that can be identified based on petrography (Goldstein and Reynolds, 1994), or, as an extension to this definition, a group of fluid inclusions that were trapped at the same time (Bodnar, 2003a). This implies that all inclusions within an FIA were trapped at the same temperature and pressure, and all trapped a fluid with the same chemical composition. If there has been no post-entrapment reequilibration (Bodnar, 2003c), all inclusions within an FIA *should* have the same homogenization temperature (T_h). However, fluid inclusions within a well defined FIA frequently show variations in T_h, even when there is undisputable evidence that the

inclusions were all trapped at the same time. For example, synthetic fluid inclusions represent the ideal case in which the inclusions are all trapped at the same time and at a known temperature and pressure. However, FIAs of synthetic fluid inclusions often show T_h variations of up to several degrees (Sterner and Bodnar, 1984). The variation has been shown to be mostly related to the fluid inclusion size, with smaller inclusions homogenizing at a lower temperature compared to larger inclusions within the same FIA (Fall and Bodnar, in prep). The variation in T_h as a function of inclusion size is related to surface tension of the fluid in the inclusion and varies with temperature (Fall and Bodnar, in prep).

The most common means of displaying microthermometric data from fluid inclusions is to plot homogenization temperatures and freezing point depressions (or salinities) on histograms. While the histograms do represent the complete range in T_h and salinity during formation, such plots provide no information concerning the evolution in temperature and salinity of the hydrothermal fluid during crystal growth. However, if the fluid inclusion data are collected within a well-defined paragenetic framework, then it should be possible to constrain the evolution of temperature and fluid salinity during crystal growth. For example, T_h and salinity data obtained from fluid inclusions in a chemically and color-zoned sphalerite (Fig. 2.2a) from the OH vein of the Creede, Colorado, epithermal deposit (Roedder, 1974, Woods et al., 1982) are plotted as histograms in Figures 2.2b and 2.2c. The results show T_h ranges from about 200 to 270°C, with an average at 240°C, and salinity ranges from about 5 to 11 wt% NaCl equiv., with an average around 8.5 wt% NaCl (Table 1). Based on the data in the histograms, the complete range in temperature and salinity during formation of the sphalerite crystal are known, but how these parameters varied during crystal growth cannot be inferred from the histograms. However, the microthermometric data shown in Figures 2.2b and 2.2c were obtained from FIAs that were identified based on their location within individual color bands of the crystal (Fig. 2.2a), thus establishing a stratigraphic succession and the relative ages of the different FIAs in the crystal. If the data are plotted on a salinity versus homogenization temperature diagram and the relative ages of the individual FIAs are labeled (Fig. 2.2d), the results reveal a complex history of fluid evolution during mineralization. For example, FIA 14 is characterized by inclusions with T_h of ≈240-245°C and salinity of about 7.5-8.0 wt% NaCl equiv., followed by later FIA 15 which is characterized by inclusions with T_h of ≈195-200°C and salinity of about 5-6 wt% NaCl equiv. Then, both the homogenization temperature and salinity *increase* in the later FIA 16, to T_h of

≈200-210°C and salinity of about 7-7.5 wt% NaCl equiv. Other reversals in T_h and/or salinity are also observed on Figure 2.2d, for example between FIA 6 and FIA 7.

If microthermometric data were not collected within a paragenetic framework and the T_h and salinity data were only displayed in histogram format (Fig, 2.2b and 2.2c) we would only know the total range in T_h and salinity during growth of the sphalerite crystal and not how they varied during growth. Similarly, if the data were plotted on a T_h versus salinity diagram (Fig. 2.2d) but without the paragenetic control, one would likely interpret the data to indicate a smooth and continuous decrease in both salinity and temperature during crystal growth. However, if the data are collected and plotted within the paragenetic framework, we observe the true temperature and salinity history of the fluids, with reversals in both temperature and salinity during crystal growth.

Fluid inclusions have been used for over one hundred years to determine the temperatures associated with various geological processes (Hollister et al., 1981; Roedder, 1984; Bodnar, 2003a). And, while much work has been done to understand the precision (and accuracy) with which the homogenization temperature (T_h) of an individual fluid inclusion can be determined (Hollister et al., 1981; Roedder, 1984), our understanding of the acceptable ranges in T_h for FIAs in various geologic environments is poor. The purpose of this study is to describe achievable and acceptable minimum ranges in T_h for FIAs from different geologic environments. The results shown here illustrate the precision with which the temperature of a geologic event can be constrained if data are obtained from FIAs that can be placed into a well-defined paragenetic framework.

2.2. Methods

2.2.1. Sample Preparation and Microthermometry

The samples used in this study were from previously well-documented magmatic, metamorphic and hydrothermal environments. All samples contained well-constrained FIAs, and in most cases the FIAs could be placed into a rigorous paragenetic framework. That is, the FIAs could be related to a specific event (i.e., growth zone or mineralization stage), but the relative ages of FIAs within each growth zone or stage generally could not be determined. Doubly

polished thick sections were prepared from each sample to exclude mechanical or thermal damage to the inclusions.

Natural samples often contain several different FIAs within the same field of view under the microscope. Identifying and distinguishing FIAs from one another was critical for this study. FIAs are defined based only on petrography, and often many different polished sections had to be examined in order to identify groups of inclusions that were clearly trapped along crystal growth zones (Fig. 2.1a), or in 3D clusters (Fig. 2.1b), or in healed microfractures (Fig. 2.1c). Some samples (e.g., fluorite, quartz in pegmatites) permitted easy recognition of FIAs because the mineral was clear and contained relatively few inclusions along either well-defined growth zones or fractures, or both. Other samples (e.g., quartz in porphyry copper deposits and metamorphic rocks) showed so many fluid inclusions within a field of view or small area of the polished section that no single inclusion or group of inclusions could be unambiguously related to a particular FIA. For these samples it was sometimes possible to make the polished section thinner, thus removing many fluid inclusions and making it easier to recognize FIAs. The initial thick sections were prepared to about 1mm thickness. At this thickness the abundance of fluid inclusions sometimes precluded the identification of FIAs. Such samples were further thinned and continuously monitored under the microscope until the section was sufficiently thin to be able to identify individual FIAs. In some cases, even this thinning technique did not allow individual FIAs to be identified with confidence and the sample was eliminated from further study. After FIAs were identified, the samples (still mounted on the glass slide) were cut into small pieces that contained one or a few FIAs to be measured. Data were only collected from fluid inclusions (FIAs) that were measured during the initial heating of the sample. This method prevented overheating of the inclusions that might lead to stretching to produce T_h higher than the original or true T_h (Bodnar, 2003c).

Microthermometric analysis of fluid inclusions was carried out using a FUID INC.-adapted USGS type gas-flow heating/freezing stage (Werre et al., 1979) mounted on an Olympus BX 51 microscope equipped with a 40x objective (N.A. = 0.55) and 10x oculars. The stage was calibrated using the CO_2-ice melting temperature at -56.6°C of H_2O-CO_2 synthetic fluid inclusions, and the ice melting temperatures at 0°C and critical homogenization temperature at 374.1°C of pure H_2O synthetic fluid inclusion standards (Sterner and Bodnar, 1984). Liquid-vapor homogenization temperatures were determined to ±0.05 degree Centigrade by thermal

cycling using temperature steps of 0.1°C. The thermal cycling technique is necessary to accurately determine T_h in some inclusions because, as the bubble gradually shrinks during heating and moves toward the wall or into a dark corner of the inclusion, it is often difficult to recognize the final disappearance if the inclusion is heated continuously (Goldstein and Reynolds, 1994). With the thermal cycling technique, the inclusion is heated until the bubble is no longer detectable. Then, the inclusion is cooled a few degrees. If the bubble had not completely disappeared, the bubble will become visible at the same location where it was last observed in the inclusion and will grow in size as the inclusion cools. If the inclusion had homogenized, it will appear unchanged during cooling of several tens of degrees until eventually the bubble "pops" back. For fluid inclusions in fluorite from the Cave-in-Rock District, Illinois, the diameter of the vapor bubble at room temperature was measured in order to calculate the inclusion size (Bodnar, 1983) to examine the relationship between inclusion size and T_h. These results are presented elsewhere (Fall and Bodnar, in prep).

2.2.2. Data presentation

As noted above, various methods have been used to present data obtained from fluid inclusions, the most common being histograms and homogenization temperature versus salinity plots (Fig. 2.2b-d). In fluid inclusion studies, histograms present the frequency of homogenization temperature or salinity measurements within a particular interval. However, this approach provides no information on salinity or temperature evolution, or values for the individual FIAs. A more preferred method is to plot salinity (freezing-point depression) versus homogenization temperature for individual FIAs that are labeled according to relative age as shown on Figure 2.2d. Each T_h – salinity field represents the range in salinity and T_h for that FIA, and the evolution in time is shown by relative ages of the FIAs. As one can observe on Figure 2.2d, many FIA fields overlap and knowledge of the relative ages of the FIAs is necessary to define the T-X path, as shown by arrows indicating the T_h-salinity path.

In this study, homogenization temperatures of individual FIAs, including the total range in T_h within the FIA as well as the average T_h and the standard deviation (1σ) are plotted along with the genetic order of the FIAs. Figure 2.3a shows homogenization temperatures of the same FIAs that are shown on Figure 2.2 for the Creede sphalerite. The short thick lines represent the average

homogenization temperature for each FIA, the error bars show the standard deviation (1σ) of the data within each FIA, and the grey boxes show the complete range in homogenization temperature for the FIA. In addition, the data for the different FIAs are plotted in their order of trapping to show the temporal evolution in homogenization temperatures for this sample. As also shown in Figure 2.2d, the results plotted on Figure 2.3a highlight the complex thermal history of the sample.

2.3. Results

In order to determine achievable ranges in T_h within an FIA that one might expect in different geologic environments we have examined samples from various sedimentary basins, metamorphic environments and magmatic-hydrothermal systems. The samples include fluorites from the Cave-in-Rock fluorspar district in southern Illinois, representing Mississippi Valley-type deposits (MVT) (Richardson and Pinckney, 1984), quartz veins from lode-gold deposits in the Maguma metamorphic terrane in Nova-Scotia, Canada (Kontak et al., 1990; 2001), quartz from the Marble Canyon Pegmatite, California, representing the earliest magmatic fluids exsolved from a crystallizing magma (James J. Student, personal communication), hydrothermal quartz veins from the Bingham Canyon porphyry Cu-Au-Mo deposit, Utah (Roedder, 1971; Redmond et al., 2004; Landtwing et al., 2005) and the Copper Creek, Arizona, porphyry system (Anderson et al., 2009), and sphalerite from the Creede, Colorado, Ag-Pb-Zn-Cu epithermal vein deposit (Roedder, 1974).

2.3.1. Cave-in-Rock, Illinois, Mississippi Valley-type deposit

Mississippi Valley-type (MVT) deposits are epigenetic hydrothermal lead-zinc ore deposits that are generally hosted by carbonates and occur in sedimentary basins (Leach and Sangster, 1993; Leach et al., 2001; Leach et al., 2005). These deposits form at low to moderate temperatures (usually 75-250°C) and are associated with highly saline basinal brines (10-30 wt% NaCl). The carbonate-hosted Pb-Zn-fluorite-barite deposits of the grater Mississippi Valley in central North America, including the Cave-in-Rock fluorspar district in southern Illinois, represent the best studied MVT deposits in the world. The Cave-in-Rock fluorspar district is a

classical example of the fluorite subtype of the MVT deposits, where fluorite is either the main gangue mineral or is present in economic concentrations. At Cave-in-Rock the fluorite mineralization occurs in veins, breccias and large bedded replacement deposits (Richardson and Pinckney, 1984; Richardson et al., 1988; Spry et al., 1990; Spry and Fuhrmann, 1994; Kendrick et al., 2002). Fluorite is the main ore mineral, however smaller amounts of sphalerite, galena, and chalcopyrite also occur. The fluorite crystals are color banded and range from an early yellow variety to late, alternating, purple and white zones. Some crystals in large vugs have diameters of up to 30 cm.

The fluorites contain two types of primary and one type of secondary inclusions. One type of irregularly-shaped primary inclusion ("primary irregular") (Figs. 2.4a, b) occurs along thin growth bands usually mixed with solid inclusions. The other type of cubic, tabular or wedge-shaped (negative crystal-shaped) primary inclusion ("primary cubic") (Fig. 2.4d) occurs within colored growth bands of the fluorites as isolated inclusions or in small clusters. The secondary inclusions occur along healed microfractures (Figs. 2.1c, 2.3c), usually parallel to the octahedral cleavage directions, and have rounded, oval or elongated shapes or negative crystal (most of the times gyroid) shapes. The inclusions contain aqueous solutions with about 20 wt% NaCl equiv. salinity, however low initial ice melting temperatures suggest the presence of a divalent cation, most likely Ca^{++} Some primary and secondary inclusions contain oil (petroleum) or aqueous-oil mixtures and are yellow brown in appearance, and usually contain dark brown opaque solids that are the result of thermal degradation of the oil (Richardson and Pinckney, 1984). At least some of the primary irregularly-shaped inclusions are earlier than some of the primary negative-crystal shaped inclusions, but we cannot prove based on petrography that all of the irregularly-shaped primary inclusions are earlier than all of the negative crystal-shaped inclusions. However, all (or at least most) of the secondary inclusions appear to post-date all of the primary inclusions based on their occurrence on fractures that crosscut all or most of the growth zones. Within each sub-type of FIA, i.e., the irregularly-shaped primary inclusions, the cubic and negative crystal-shaped primary inclusions, and the secondary inclusions, the relative ages of FIAs could not be determined with confidence.

Microthermometry was carried out on 33 FIAs that could be related to either a growth zone or a healed fracture. Each FIA contained between 9 and 56 fluid inclusions (Fig. 2.5). Ten FIAs of the irregular primary inclusions trapped along thin growth zones in fluorite show average T_h

ranging from 152.0 to 156.1°C with Th variations within an FIA of ranging from 5.5 to 9.4°C, and standard deviations of 1.5 to 3.2. Nine small clusters of the primary negative crystal-shaped inclusions yield average T_h ranging from 143.8 to 148.5°C with T_h variation within an FIA ranging from 3.6 to 7.7°C, and standard deviations of 1.0 to 3.0. Average T_h for fourteen secondary FIAs trapped along healed microfractures varies from 142.0 to 145.2°C with Th variations within individual FIAs ranging from 1.2 to 2.8°C, and standard deviations of 0.3 to 1.0 (Fig. 2.5).

2.3.2. Meguma, Nova Scotia, metamorphic lode-gold deposit

The mesothermal (orogenic) lode gold deposits of the Meguma metamorphic terrane in Nova Scotia, Canada, represent Au-rich quartz veins in metaturbiditic rocks of the Meguma Group (Kontak et al., 1990; Kontak and Kerrich, 2002; Kontak et al., 2005). The Meguma group was deformed into tight- to open-, chevron- to box-shaped folds and metasomatized to greenschist-amphibolite facies. The fold belt was reactivated by a brittle-ductile deformation ca. 375 Ma, followed by late syntectonic intrusion of ca. 370 Ma, meta- to peraluminous, crust-derived granitic plutons. The veins are confined to fold hinges and adjacent steep limbs and were emplaced during flexural-slip folding late in the history of the Meguma Group. The emplacement of the veins was in some places coincident with the granite intrusion (Kontak et al., 2001). The veins are dominated by white, crystalline quartz, but calcite, mica and feldspar are also present. The genetic model of Kontak et al. (2001) indicates that the vein-forming fluids where not entirely magmatic and were in part exotic to the Meguma Group, and show variable amounts of interaction with wall rocks, as indicated by alteration, replacement textures, and isotopic data. The generation of CO_2-rich aqueous ore-forming fluids, characteristic of this environment, is associated with metamorphic devolatilization of subcreted hydrated crust (Bierlein and Crowe, 2000). The initial temperatures of the vein-fluids approached about 450°C in the early stage and cooled continuously to about 300±50°C during the later stage.

Fluid inclusions from 27 FIAs in quartz from the Meguma metamorphic lode-gold deposit show relatively large T_h variations (Fig. 2.6) compared to those previously described for the Cave-in-Rock MVT deposit. There is no petrographic evidence for primary inclusions, and three different types of secondary inclusions, based on chemical composition, are present. One type

contains H_2O-CO_2 with 10-15 mol% CO_2 (Fig. 2.4e). A second type contains low salinity H_2O-NaCl (<1-2 wt% NaCl) (Fig. 2.4f). The third, less common, type of inclusion contains halite daughter minerals in addition to liquid and vapor. This latter type showed extremely heterogeneous phase ratios within the same FIAs, and good petrographic evidence of necking is observed. For this reason T_h data were not collected from these FIAs. All three types of fluid inclusions occur along healed microfractures; however textural properties of the host observed under crossed polars (different extinction angles of the quartz along healed microfractures) suggest that the low salinity H_2O-NaCl inclusions are later than the carbonic inclusions. This paragenesis is consistent with the observations of Robert et al. (1995) for similar lode-gold quartz veins in the Val d'Or district of the southeastern Abitibi greenstone belt, Canada. The fourteen H_2O-NaCl FIAs show average T_h ranging from 207.9 to 307.8°C, with T_h variations ranging from 5.7 to 125°C, and standard deviations of 1.6 to 24.8. The thirteen H_2O-CO_2 FIAs show average T_h ranging from 272.5 to 308.6°C, with T_h variations from 3.6 to 24.9°C, and standard deviations of 1.1 to 6.5 (Fig. 2.6).

2.3.3. Marble Canyon Granitic Pegmatite

Pegmatites form from residual melts generated during crystallization of granitic magmas, and are enriched in incompatible components, fluxing agents, volatiles and rare earth elements (Černý, 1991; Černý and Ercit, 2005; Simmons and Webber, 2008). Granitic pegmatites are usually characterized by their large crystal sizes. Chemical fluxes (B, F, P, Li) and volatiles (H_2O) lower the crystallization temperature, decrease nucleation rates, increase diffusion rates and solubility and are all genetically critical to the development of the large crystals and pegmatitic textures. Primary and pseudosecondary FIAs in pegmatitic minerals represent early magmatic fluids associated with crystallization of hydrous magma.

The Marble Canyon Pegmatite (MCP) is an intrusion in the contact aureole of the composite EJB pluton (James J. Student, personal communication) in the Deep Springs Valley-Eureka Valley region of the White-Inyo Mountains of eastern California. The Jurassic EJB is characterized by three principal units: the Eureka Valley monzonite, the Joshua Flat quartz monzonite, and the Beer Creek granite (Coleman et al., 2005; Jackson et al., 2007; Reynolds et al., 2007; Straathof et al., 2007). The recently discovered pegmatitic body contains large crystals

of feldspars, quartz, micas and minor schorl. Also small pockets with quartz, axinite and associated fluorite were observed. Much of the axinite is massive and occurs in fractures associated with pneumatolytic fracturing of the pegmatite. The pegmatite is on strike with the aplite dikes of EBJ pluton, which have been boudinaged in the aureole. This relation suggests that the pegmatite is associated with the EJB magmatism (James J. Student, personal communication).

The large quartz crystals found in pockets in the Marble Canyon Pegmatite are zoned with a smoky quartz core and a clear outer rim, separated by a thin dark growth zone. The quartz crystals contain well-defined FIAs of primary, pseudosecondary and secondary inclusions. The core contains secondary, two-phase liquid-vapor inclusions, and pseudosecondary halite-bearing inclusions along trails that start in the dark growth zone and extend into the core (Fig. 2.4g). The dark growth zone contains primary halite-bearing inclusions, similar to the pseudosecondary inclusions that occur in the core. The outer light rim contains secondary halite-bearing inclusions that represent a later generation of high salinity fluids.

The fluid inclusions in this sample contain a solution approximated by the system H_2O-NaCl-$CaCl_2$, confirmed by low initial ice melting temperatures (~-52°C), with varying amount of $CaCl_2$ and NaCl. The secondary inclusions restricted to the core (Fig. 2.4h,i)contain solution with a salinity below halite saturation, and with high $CaCl_2$ concentration that was confirmed by formation of antarcticite ($CaCl_2$•$6H_2O$) during cooling (Fig. 2.4h). The primary inclusions trapped along the growth zone, and the pseudosecondary trails that start in the growth zone and extend into the core, contain halite-saturated solution, with a salinity (determined from the halite dissolution temperature) of around 30 wt% NaCl (Bodnar and Vityk, 1994). The outer clear zones of the crystals contains secondary, halite-bearing inclusions with a salinity of about 33 wt% NaCl equiv. (Fig. 2.4j) and no antarcticite formation during cooling. This succession suggests the presence of Ca-rich salt solutions early in the crystallization history that evolved toward a more Na-rich and Ca-poor solution with time. The high salinities of the magmatic fluids in the MCP is consistent with chlorine partitioning data that suggest that in deeper magmatic systems the early fluids should have high salinities (Cline and Bodnar, 1994). Four secondary FIAs in the core show average T_h ranging from 255.6 to 276.6°C, with T_h variations ranging from 2.9 to 14.6°C and standard deviations of 0.7 to 7.5. Two primary and three pseudosecondary FIAs show average T_h ranging from 234.4 to 254.5°C, with T_h variations

ranging from 5.3 to 28.3°C and standard deviation of 2.2 to 7.1. The secondary inclusions in the clear rim have average T_h ranging from 253.8 to 284.5°C, with T_h variations ranging from 2.6 to 15.3°C and standard deviations of 0.8 to 2.6 (Fig. 2.7).

2.3.4. Bingham Canyon, Utah, and Copper Creek, Arizona, porphyry copper deposits

Porphyry copper deposits are large, relatively low-grade, epigenetic, intrusion related copper deposits. Numerous workers have studied the structural, geochemical and economic aspects of these deposits (e.g., Sillitoe, 1973, 2000; Norton, 1978; Titley and Beane, 1981; Beane and Titley, 1981; McMillan and Panteleyev, 1988; Beane and Bodnar, 1995, Landtwing et al., 2005; Seedorff et al., 2005). These studies generally agree on several aspects of the porphyry copper deposits: they are spatially and genetically related to felsic intrusions that range widely in composition, the intrusions are epizonal and porphyritic, are characterized by multiple intrusive events, the intrusions and surrounding rocks are intensely fractured, and exhibit laterally zoned mineralization and alteration. Magmatic-hydrothermal fluids play an important role in the formation and evolution of porphyry copper deposits. Most of the information on the physical and chemical evolution of these hydrothermal fluids results from fluid inclusion studies (Roedder, 1971; Moore and Nash, 1974; Reynolds and Beane, 1985; Bodnar, 1995; Beane and Bodnar, 1995; Redmond et al., 2004, Landtwing, 2005).

One of the classic and most studied porphyry copper deposits is the Bingham Canyon porphyry ore deposit in Utah. A euhedral quartz crystal that has previously been referred to as quartz type Q1 (Redmond et al., 2004; Landtwing et al., 2005) and comes from the quartz monzonite porphyry intrusion that represents the earliest and largest porphyry intrusion, was used for this study. A quartz sample from the quartz-cemented granodioritic breccia of the Copper Creek porphyry deposit in Arizona was also examined (Anderson et al., 2009). The hydrothermal quartz veins from these deposits contain a large number of fluid inclusions that precluded the distinction of primary inclusions from secondary or pseudosecondary inclusions; hence the data were obtained from FIAs trapped along healed microfractures where the contemporaneity of the inclusions was clear. Fluid inclusions from 34 FIAs in quartz from these deposits show relatively large T_h variation within FIAs (Fig. 2.8). At room temperature four types of inclusions can be observed: liquid-vapor inclusions with a large vapor bubble and

opaque phase and intermediate salinity of around 7-12 wt% NaCl eqv., (Fig. 2.4k), inclusions containing brine and halite and sylvite daughter minerals and sometimes anhydrite daughter crystals (Fig. 2.4l), vapor-rich inclusions (Fig. 2.4l), and liquid-vapor inclusions with smaller vapor bubble and salinities of around 15-20 wt% NaCl Eqv. (Fig. 2.4m). The two-phase inclusions with large vapor bubbles (Fig. 2.4k) showed evidence for CO_2 during cooling by the formation of a clathrate phase. Three FIAs of the two-phase inclusions with a large vapor bubble, representing fluid trapped in the early stage of the porphyry system evolution (Roedder, 1971; Landtwing et al., 2005), show average T_h ranging from 360.2 to 378.2°C, with T_h variation ranging from 10.1 to 11.4°C, and standard deviations from 2.7 to 3.9. Twenty FIAs of brine inclusions that homogenized by vapor disappearance (brine 1) show average T_h ranging from 264 to 563°C, with T_h variations ranging from 2.6 to 62.1°C, and standard deviations from 1.0 to 17.8. Seven FIAs of brine inclusions that homogenize by halite disappearance (brine 2) show average vapor-to-liquid T_h ranging from 260.4 to 397.7°C, with T_h variations ranging from 9.1 to 75.1°C, and standard deviations from 3.0 to 32.1. Four FIAs, representing the late post-ore stage (Landtwing et al., 2005) at Copper Creek show average Th ranging from 339.4 to 346.6°C, with Th variations ranging from 3.5 to 10.1°C, and standard deviations from 2.5 to 2.8 (Fig. 2.8).

2.3.5. Creede, Colorado, epithermal deposit

Epithermal deposits develop in shallow volcanic settings as a result of intrusion-related hydrothermal activity. They are important deposits of Au and Ag as well as Zn, Pb, and Cu (Simmons et al., 2005). Fluid inclusions in epithermal environments are distinctively different than those in the deeper intrusive environments (e.g., porphyry). They typically contain two phase liquid-vapor, low salinity fluids, daughter minerals are absent. A common feature in the epithermal deposits is the coexistence of liquid-rich and vapor-rich fluid inclusions, demonstrating the occurrence of boiling in this low-pressure environment (Bodnar et al., 1985).

The Creede, Colorado, deposit is a well known epithermal deposit and was the subject of many studies of the geologic and hydrologic settings (Steven and Eaton, 1975), geochemical aspects (Roedder, 1974; Barton et al., 1977; Bethke and Rye, 1979; Hayba, 1997), and duration and age (Bethke et al, 1976; Campbell and Barton, 2005) of the ore deposition. One of most studied segments of the ore deposit was the OH vein, which is a steeply dipping series of

connected tension fractures up to 2 m wide, that at depth become an open breccia with minor quartz, chlorite and sulfide mineralization (Barton et al., 1977). The vein was formed through five paragenetic stages, labeled by Bethke and Rye (1979) from "A" (youngest) to "E" (oldest). The "D" stage was the most studied of these, consisting of large, zoned sphalerite crystals that made possible correlations of crystal growth zones throughout the deposit (Hayba, 1997). The sphalerite crystals are coarse grained (some are 10 cm or more in diameter) and zoned, reflecting variations in iron content, and on this basis was subdivided onto 3 sub-stages: inner white-yellow (IWY), orange-brown (OB), and outer yellow-white (OYW) (Fig. 2.1a). Roedder (1974) documented the fluid inclusions in one such zoned sphalerite crystal, demonstrating the changes in temperature and salinity of the ore fluid over time studying FIAs in 20 different stratigraphic zones.

The homogenization temperature data presented here are from Roedder (1974). The analyzed fluid inclusions were mostly primary (Fig. 2.4n) and pseudosecondary (Fig. 2.4o), and are mostly large, elongated and negative crystal-shaped. Fluid inclusions from 20 FIAs in sphalerite show relatively small T_h variation within FIAs (Fig. 2.3). Salinities vary between 5 to 11 wt% NaCl. The 20 FIAs show average T_h ranging from 198.3 to 268.1°C, with T_h variations ranging from 0 (only two inclusion in the FIA with same T_h) to 6.3°C, and standard deviations of 0 to 2.3.

2.4. Potential causes of T_h variations within FIAs

As we have shown above, there is always a measurable range in T_h within an FIA that is significantly larger than the analytical precision (±0.05°C). Several factors influence the extent of the homogenization temperature ranges in FIAs and therefore affect the precision and accuracy with which the temperature of a geologic event can be constrained using fluid inclusions. These factors may include the size of the fluid inclusions, natural temperature and pressure fluctuations during, and after, inclusion trapping, physical properties of the host mineral, sample collection and preparation, and microthermometric procedures.

Even in the ideal situation in which every fluid inclusion in the FIA is trapped at exactly the same temperature and pressure, the homogenization temperatures of those inclusions still show a small variation related to the size of the fluid inclusion (Fall and Bodnar, in prep.). As inclusions are heated the vapor bubble shrinks and reaches a critical bubble radius at which point the bubble

will "blink out" to cause homogenization. Within the same FIA small fluid inclusions homogenize at slightly lower temperature than larger inclusions. This behavior is largely a function of the surface tension of the liquid-vapor interface and the radius of the vapor bubble. For aqueous inclusions that homogenize at temperatures less than about 230°C, the maximum range in T_h resulting from variations in inclusion size should be no more than a few degrees. The size dependency of T_h decreases with increasing temperature and is not observed for homogenization temperatures higher than about 230°C for aqueous inclusions. This is expected as the surface tension decreases with increasing temperature and becomes nil at the critical point (Fall and Bodnar, in prep.).

The geological environment to a large extent defines the temperature and pressure fluctuations that might occur during and after the formation of an FIA. If the temperature and/or pressure varies while fluid inclusions are being trapped to produce the FIA, a range in T_h will result, with the magnitude of the range being a function of the PTX formation conditions and their variation during inclusion trapping. Goldstein and Reynolds (1994) describe examples in which FIAs are trapped in relatively thick growth zones that form during temperature fluctuations. In this case, petrographic evidence to determine which inclusions may be early or late might be absent, so all of the inclusions would be grouped into the same FIA which would show some measurable range in T_h. If fluid inclusions with similar sizes and shapes show a consistent decrease in T_h from the interior towards the outer edge of the growth zone, a decreasing temperature trend as the growth zone formed is suggested.

Perhaps a more important factor than temperature and pressure changes during FIA formation is the amount of time required for all of the inclusions in an FIA to form. As was mentioned above, FIAs represent fluid inclusions that were trapped at the same time. The "same time" is a relative term and the actual amount of time required for an FIA to form is expected to vary depending on the geologic environment. The question then is how much time does it take for a growth zone to form during crystallization of a mineral, or how much time is required to heal a microfracture and trap inclusions? If the temperature and pressure remain constant during crystal growth or during healing of a fracture, then the amount of time required for these processes to occur will not affect the T_h. However, if the temperature and/or pressure do change while the FIA is forming, the variation in T_h will be a function of the magnitude of the temperature and pressure changes. How fast a growth zone is formed or a microfracture is healed

depends on the solubility of the host mineral and this is related to the temperature, pressure and fluid chemistry in the specific environment (Rimstidt, 1997). An experimental study of diffusional crack healing in quartz by Smith and Evans (1984) showed that fractures in single quartz crystals healed in hours to two days in the presence of pore fluid at 200 MPa pressure at 200°, 400°, and 600°C temperatures. They observed that the amount of healing depends on the temperature (almost complete healing at temperatures ≥400°C), initial silica concentration of the pore fluids, and the initial crack dimension. Similar experimental studies (Brantley et al., 1990; Brantley, 1992) related to crack healing in quartz at hydrothermal conditions showed that microfractures 100 μm long and 10 μm wide heal in about 4 hours at 600°C and 200 MPa in the presence of pure water, and at 200°C the cracks heal in about 40 days to 1000 years (Fig. 2.9). They also report that fluid composition can affect the healing time. The presence of salts (NaCl, $CaCl_2$) decreases healing time, while CO_2 increases the healing time compared to pure H_2O. In a similar study, Teinturier and Pironon (2003) showed that microfractures in fluorite healed in 82 and 257 hours in the presence of an NH_4Cl-H_2O solution at 200°C and saturation pressure. They also showed that microcracks in quartz healed in about 3 days in the presence of NaCl-H_2O solution at 400 bars as the temperature of the system decreased from 400 to 300°C, while a quartz overgrowth band of about 20 μm formed in about 2 days.

After an FIA forms, inclusions might be exposed to different pressure and temperature conditions during burial or uplift, or during sample preparation in the lab, and the inclusions might reequilibrate (Bodnar, 2003c). This process can affect the homogenization temperatures of fluid inclusions within the FIA and affect the range in T_h because fluid inclusions within the same FIA might respond differently to changes in pressure and/or temperature. Some inclusions may show more evidence for reequilibration, while others may show less, or no evidence at all, and maintain their original volume and fluid content. Several factors determine the ease with which fluid inclusions reequilibrate, including the inclusion size and shape, the physical and chemical properties of the host mineral, fluid composition, and the P-T path followed by the host rock after the entrapment (Bodnar, 2003c). Inclusions are most likely to reequilibrate when the P-T path followed after trapping differs from the path defined by the isochore of the inclusions. The P-T path followed by the inclusions after trapping determines if the internal pressure in the inclusion exceeds, or is less than the confining pressure (Fig. 2.10), resulting in different diagnostic textures for the fluid inclusions (Vityk et al., 1994; Vityk et al, 2000; Bodnar, 2003c).

As the inclusion volume or composition changes, the microthermometric behavior of inclusion will change accordingly. When the mineral follows a P-T path that results in an internal overpressure in the inclusions the volume of the inclusions can change by stretching the inclusion, decreasing the density in the fluid and resulting in an increase in the homogenization temperature. As larger inclusions are more susceptible to internal overpressure, these inclusions will reequilibrate to the largest extent, resulting in higher homogenization temperatures and greater homogenization temperature variations within an FIA. Another important factor related to reequilibration of fluid inclusions is the physical and chemical properties of the host mineral. The type of reequilibration is related to the mineral hardness. For example fluid inclusions in soft cleavable minerals (fluorite, sphalerite, and barite) are more likely to stretch and leak if the inclusions are overheated in nature or in laboratory (Bodnar and Bethke, 1984; Ulrich and Bodnar, 1988), while fluid inclusions in hard minerals, such as quartz, are more likely to resist the increase in internal pressure with increasing temperature and maintain their original shape and fluid content until they decrepitate with total loss of the fluid (Bodnar, 2003c).

A "text book" example of the effect of stretching on fluid inclusions within an FIA was observed in quartz from the Meguma metamorphic lode-gold deposits (Figure 2.11). Thirty eight fluid inclusions, containing a low salinity H_2O-NaCl solution and located along a healed fracture (fifteen shown on Figure 2.11a) have similar sizes and apparent liquid-to-vapor ratios at room temperature. These inclusions clearly represent an FIA and were trapped at the same time, and one would expect them to show similar homogenization temperatures. However, the inclusions show a large T_h variation, ranging from 163.3 to 245.5°C (Fig 2.10b). The distribution of T_h for this FIA is similar to that shown by both natural and synthetic fluid inclusions that have reequilibrated by stretching (Vityk and Bodnar, 1995). In their experimental study H_2O-rich synthetic fluid inclusions in natural quartz that were originally trapped at 700°C and 500 MPa were reequilibrated at 625°C and 200 MPa for a period of 180 days. Fluid inclusions that originally homogenized around 284°C subsequently homogenized between 305 and 330°C, and up to 372°C, after the experiment, as a result of stretching (Fig. 2.11c). Comparing the histogram for the Meguma FIA with the results of these experiments shows similarities in the distribution of homogenization temperatures (Fig. 2.11b, c). The comparison suggests that the large T_h variation range in the Meguma FIA is a result of stretching, and the higher homogenization temperatures in the FIA are the result of a lower density within those inclusions. This

observation is important when interpreting these data. The lowest homogenization temperatures (highest densities) are those that most closely represent the original trapping conditions and not the grouping of homogenization temperatures around 215°C (Fig. 2.11b). In many fluid inclusion studies in which homogenization temperature distributions similar to those shown in Figures 2.10b and 10c are reported, the authors select the "average" homogenization temperature (i.e., ≈220°C at Meguma and ≈315°C in the experimental sample) as most closely representing the original trapping conditions – this interpretation is clearly incorrect.

Another common process that can lead to variations in T_h is "necking down" of the fluid inclusions (Roedder, 1984), which is defined as the dissolution and re-precipitation of the host mineral, usually resulting in the generation of numerous smaller inclusions from one or a few larger inclusions. Necking down is most commonly associated with secondary fluid inclusions formed along healed microfractures (Roedder, 1962). However, it is important to emphasize that *all* inclusions "neck-down" and change their shapes following trapping and tend to become more regularly-shaped (Bodnar et al., 1989). If necking of the inclusions occurs at the P-T trapping conditions, or in a closed (isochoric) system in the one phase fluid field, the inclusions will all have similar phase ratios and microthermometric behavior. If the inclusion does not remain an isochoric system during necking, or if necking occurs in the presence of two or more phases, the inclusions will likely show a range in microthermometric data. For example, assume a fluid inclusion traps a homogeneous phase in a cooling system. As the temperature decreases and the isochore intersects the liquid-vapor curve, a vapor bubble will nucleate. During further cooling the vapor bubble will increase in size as the liquid contracts. If the inclusion necks down at this point to produce two inclusions, only one of the inclusions will trap the vapor bubble, with the other inclusion containing only liquid. If the cooling continues the inclusion that trapped only liquid may nucleate a small vapor bubble, and the process could be repeated if the inclusions neck again. This process will produce an FIA with widely variable phase ratios, and different densities, and as a consequence the homogenization temperature variation within the FIA will be significant. For example, a density variation of about 5% could produce homogenization temperature variations within the FIA of at least 50°C in the diagenetic environment (Goldstein and Reynolds, 1994).

Other factors that could have an influence on T_h variations within FIAs are the sample collection and preparation methods, and thermal gradients in the heating-cooling stage during T_h

measurements. These laboratory effects can be eliminated through careful processing of the samples. As mentioned above fluid inclusions tend to reequilibrate volumetrically when the internal pressure in the inclusion exceeds the strength of the host mineral. Generally, heating the samples above room temperature or above the homogenization temperature can generate pressures high enough to change the original volume of the inclusions, especially in soft minerals such as calcite, barite, sphalerite, etc.

Aqueous fluid inclusions that homogenize at low temperature may also reequilibrate during cooling to measure the ice-melting temperature. Because the volume of the ice is larger than that of the liquid by 9.06%, when liquid water freezes to form ice the volume of the "fluid" increases. If the vapor bubble in the inclusion occupies less than 9.06 volume percent of the inclusion before freezing, the ice will expand to fill the entire inclusion volume and "push" on the inclusion walls to generate high pressures that can stretch the inclusions (Lawler and Crawford, 1983). A pure H_2O inclusion containing 9.06 volume percent vapor at the pure H_2O triple point (0.01°C) (or 8.9 volume% vapor at 22°C) will homogenize at 158°C – thus any aqueous fluid inclusion that homogenizes at ≤150°C may stretch during freezing. Therefore, the homogenization temperatures of low temperature inclusions should be measured *before* the ice-melting temperature is measured. In this study, all freezing measurements were made after T_h was measured, so freeze stretching could not be the cause of T_h variations observed in the study.

Drill core temperatures may reach 110-230°C during core drilling (Goldstein and Reynolds, 1994). Fluid inclusions in outcrop samples can also be overheated by solar heating, or by forest or grass fires. Such samples should be avoided as the inclusions may have reequilibrated and will produce elevated T_h values. Thermal or structural damage to the sample introduced during cutting, grinding and polishing of the thick sections and during mounting on the glass slide, if thermally activated adhesives are used, can also lead to anomalous T_h values. With care these effects can be minimized or eliminated.

2.5. Discussion

In the above discussion we have outlined some of the processes that could lead to T_h variations in FIAs. These processes include the effect of inclusion size, variations in temperature and/or pressure during inclusion formation, and reequilibration of the inclusions after trapping.

The size effect does contribute to the variation in T_h, especially for inclusions that homogenize at relatively low temperatures ($\leq\approx$250°C) and most of the T_h variation observed for the secondary inclusions in the Cave-in-Rock samples can be attributed to the effect of inclusion size. However, the maximum variation that can be attributed to size is on the order of a few degrees (Fall and Bodnar, in prep.) and cannot account for the total variation observed in all environments studied here.

Variations in temperature and/or pressure during inclusion formation will obviously lead to variations in T_h. However, experimental and theoretical studies of crack healing and mineral precipitation indicate that the time required to heal a fracture or to precipitate a growth zone on the order of 10s to 100s of micrometers is short relative to the time scale over which significant temperature changes are likely to occur. For example, Brantley et al. (1990) report that cracks in quartz will heal in less than one year at 300°C, and in significantly shorter times at higher temperature. Similarly, Teinturier and Pironon (2003) report that microfractures in fluorite healed in 82 and 257 hours at 200°C. It is clear that growth zones can form and microfractures can heal in short periods of time (instantaneously on a geologic time scale), and it is therefore necessary to understand the rate of temperature change in different geological environments to assess whether temperature changes could be responsible for the variations in T_h observed here.

Mississippi Valley-type deposits are associated with fluid flow in sedimentary basins, with no obvious relation to igneous activity (Leach et al., 2001). The fluids migrated large distances in relatively undisturbed rocks and ore formation usually takes place at the margin of the sedimentary basin or near basement "highs". The Cave-in-Rock deposit is estimated to have formed over a time span of 10^6 to 10^7 years (Richardson and Pinckney, 1984), and Garven (1985) estimated similar time-scales for ore formation (0.5 – 5 Ma) at the Pine Point Deposit, Canada.

Garven and Raffensperger (1997) describe a numerical fluid flow model for the formation of ore deposits in sedimentary basins, including the MVT deposits. Their results predict the time-temperature evolution in the Appalachian and Illinois Basins. At a location on the flanks of the Nashville Dome, near the location of the southern Illinois fluorspar district, their results predict a transient thermal high of 148°C after 70,000 years of fluid flow, and the temperature at this location decreases linearly to 115°C after 700,000 years of flow. This corresponds to an average temperature decrease (148-115/700,000-70,000) of 5.2×10^{-5} °C/yr. The primary negative crystal-

shaped inclusions at Cave-in-Rock show minimum T_h variations of 3 to 4 degrees Centigrade (Fig. 2.12a), with the majority varying between 4 to 7 degrees Centigrade. At a cooling rate of 5.2×10^{-5} °C/yr, between 50,000-135,000 years would be required to produce temperature changes of 3-7 degrees Centigrade. The time to produce the temperature ranges observed in the irregularly-shaped primary inclusions would be even longer, up to 150,000 years. The secondary inclusion temperature variations could occur in ≈20,000 years. However, Teinturier and Pironon (2003) have shown that microfractures in fluorite can heal in as little as 82 hours at 200°C. Thus, it appears that temperature variation alone cannot account for the observed variation in T_h, even for those FIAs that show the smallest T_h variation.

Orogenic *lode gold deposits* in metamorphic rocks generally form at relatively deep levels in the crust during active tectonism. Lode gold quartz veins in metamorphic terranes provide evidence for large volume fluid circulation during deformation of metamorphic rocks. At Meguma (Kontak, 1990) the temperature decreased from about 450°C in the early stages of mineralization to about 300°C in the later stages. The amount of time for the temperature to decrease from 450 to 300°C (and to form the deposit) is unknown, but the duration of mineralization in orogenic lode gold deposits is generally less than the uncertainty on the age determinations, which in the case of Meguma translates to about 5×10^6 years, from 370 -375 Ma. If we assume that it took at least 10,000 years and less than 10,000,000 years to form the Meguma mineralization, and for the temperature to decrease from 450°C to 300°C, the average temperature decrease ranges from 0.015 °C/year to 1.5×10^{-5} °C/year. At Meguma, the carbonic FIAs show minimum T_h variation within an FIA of about 3 to 4 degrees Centigrade, with the majority around 6 to 12 degrees Centigrade. The H_2O-NaCl inclusions show minimum T_h variations between 5 to 7 degrees Centigrade, with the majority between 20 to 30 degrees Centigrade (Fig. 2.12b). Assuming a cooling rate of 0.015 °C/year (i.e., the mineralization formed in 10,000 years), the observed ranges in T_h could be produced in 200-2,000 years, or in 200,000 to 2,000,000 years (assuming that the entire mineralization event lasted 10,000,000 years). As noted above, experimental studies by Brantley et al. (1990) show that cracks in quartz heal in less than one year at temperatures >300°C. Thus, it appears that temperature decrease cannot account for the complete range in T_h observed at Meguma.

The *Marble Canyon Pegmatite* is a granitic pegmatite associated with the EJB pluton that was emplaced at depths on the order of 8-10 km (Morgan et al., 2007). Primary FIA trapped in

the dark growth zones of the quartz crystals show large T_h variations of 18 and 28°C. The observed minimum T_h variation for the early secondary inclusions restricted to the core of the quartz is around 3 degrees Centigrade with the majority ranging between 5 and 10 degrees Centigrade. The late secondary inclusions in the rim show minimum T_h variations in the range of 2 to 3 degrees Centigrade, with the majority around 5 to 8 degrees Centigrade (Fig. 2.12c).

Numerical models of cooling pluton environments (Knapp and Norton, 1981) indicate that in the core of the pluton (~10 km) it requires about 100,000 years for the temperature to decrease from 600 to 400°C. Using these values the average temperature decrease is about 2×10^{-3} °C/year. This, in turn, would require from 1,000 years ($\Delta T_h = 2$°C) to 14,000 years ($\Delta T_h = 28$°C) to produce the observed temperature variations if they were the result of temperature decrease alone. However, assuming that the depth of formation was ≈10 km, the temperature at trapping would have been about 500°C. At this temperature fractures in quartz would heal in a matter of days. Again, it does not appear that the observed variations in homogenization temperature in the Marble Canyon Pegmatite are the result of temperature variation alone.

Porphyry deposits are magmatic-hydrothermal deposits that form in response to the emplacement and cooling of hydrous intermediate composition magmas. The presence of multiple intrusions and crosscutting vein systems characteristic to porphyry deposits make it possible to determine relative ages of hydrothermal events (Seedorff et al., 2005). The duration of hydrothermal activity is believed to be on the order of 5×10^4 to 5×10^5 years, although large porphyry copper deposits with multiple intrusions and fluid events may span several millions of years (Norton, 1978; Seedorff et al., 2005). The observed homogenization temperature variations of early two-phase, vapor-rich FIAs from Bingham Canyon are around 10 degrees Centigrade (Fig. 2.12d). The brine inclusions show minimum T_h variations in the range of 2 to 3°C, with the majority around 20 to 30 degrees Centigrade. The late fluids at Bingham Canyon show minimum T_h variation around 3 degrees Centigrade with the majority showing variations of around 10 degrees Centigrade (Fig. 2.12d).

In many porphyry copper systems the main mineralization stages occurs in the temperature range from about 500°C to 300°C (Roedder and Bodnar, 1997; Landtwing et al., 2005). Numerical models of the cooling history for a location near the top of a shallow pluton (Knapp and Norton, 1981) corresponding to the H_2O-saturated solidus where porphyry-type mineralization forms (Becker et al., 2009) shows that the temperature decreases from 500 to

300°C in about 71,000 years, corresponding to a cooling rate of 2.8×10^{-3} °C/year. Thus, the observed temperature variations at Bingham Canyon would require from about 700 to 11,000 years to be produced by temperature decrease alone. As with previous examples, these times are not consistent with known rates of fracture healing at these temperatures.

Epithermal deposits form in the shallow volcanic environment above a cooling pluton. The formation of the OH vein at Creede, Colorado, was controlled by an overlying aquitard. The low permeable zone forced the upwelling hydrothermal fluids to flow laterally along the vein (Hayba, 1997), consistent with zoning of the sphalerite crystals along the length of the vein. The abrupt color changes between the growth zones of the crystals suggest that the nature of the ore fluid changed abruptly. Within each growth zone, however, the nature of the fluid was constant along the entire vein (Roedder, 1974; Hayba, 1997), as demonstrated by the similar compositions of the fluid inclusions within the same FIA.

FIAs within the studied sphalerite show homogenization temperature variations as low as 1 degree Centigrade, with majority ranging between 1 to 3 degrees Centigrade (Fig. 2.12e). Barton et al. (1977) suggested that with a flow rate of 0.5 cm/sec one cycle of the fluid flow would cover the 2 km length ore body in 500 days, and during each cycle about 50 μm of sphalerite would precipitate. A sphalerite crystal with an overall thickness of about 8 cm would have been deposited in about 2000 years. If we assume that the sphalerite crystal shown in Figure 2.2a formed in 2000 years as the temperature decreased from 275 to 200°C, the average rate of temperature decrease would be 0.0375 °C/year. Conversely, numerical modeling of the thermal history of a point above a cooling pluton that corresponds to the epithermal environment (Knapp and Norton, 1981) indicates that the temperature will decrease from about 275 to 200°C in about 135,000. This corresponds to rate of temperature decrease of 5.5×10^{-4} °C/year. Using these two rates of temperature change as limiting values, the observed variation in T_h would require from 30 to 1,800 years to produce a one degree variation, to about 90 to 5,400 years to produce a three degree variation. Owing to the fact that the sphalerite crystal is zoned allowing the relative ages of the FIAs to be determined, it is quite clear that the temperature (as well as the salinity) of the ore-forming fluids at Creede did vary with time. The small T_h variations in this shallow system, where deeper magmatic fluids are mixing with cooler meteoric fluids, may reflect these natural temperature fluctuations during crystallization of the sphalerite and trapping of the inclusions.

While it is unlikely that temperature variations during the formation of an FIA can explain the observed variations in T_h in most of the samples studied, it is possible that some or all of the variation might be related to pressure fluctuations during FIA formation, at least in some environments. In the epithermal environment, it is well known that pressure fluctuates between nearly lithostatic and hydrostatic conditions as a result of repeated sealing and fracturing (Cooke and Simmons, 2000). Similarly, in the orogenic lode gold deposits, Robert et al. (1995) has shown that pressure fluctuations and concomitant phase separation (boiling) is often associated with gold deposition. Hydraulic fracturing and brecciation related to pressure are also common in the porphyry environment. Fournier (1985) also notes that quartz solubility decreases with decreasing pressure at constant temperature, and the effect is especially significant at temperatures >340°C. As a result, FIAs could form at constant temperature as quartz precipitates during a fracturing event that results in decreased pressure. Thus, in the epithermal, porphyry copper and lode gold environments, at least some of the observed variation in T_h may be the result of pressure fluctuations during the formation of FIAs.

While inclusion size and pressure fluctuations might account for some of the observed variation in T_h, most of the variation observed in natural samples is likely the result of reequilibration of the inclusions following trapping. This interpretation is supported by the fact that the major cause of fluid inclusion reequilibration is pressure differential between the inclusion and surrounding environment (Fig. 2.9) (Bodnar, 2003c). And, inclusions that are most likely to be exposed to pressure differentials large enough to initiate reequilibration during transport from the PT formation conditions to the earth's surface are those that form at higher pressure (and temperature). In this study, the environments that show the greatest variation in T_h are those that represent the highest temperature and/or pressure conditions.

Bodnar (2003c) describes the various types of reequilibration that fluid inclusions experience, and relates these to the strain rate (high vs low), deformation mechanism (plastic vs brittle) and open versus closed system reequilibration (volume change without fluid loss vs partial to complete fluid loss). In a low strain environment, fluid inclusions will reequilibrate via plastic deformation without fluid loss. In other words, the volume of the fluid inclusion will change. This reequilibration process has been referred to as "stretching", although it should be noted that the fluid inclusion volume may increase or decrease during reequilibration, depending on whether the internal pressure in the inclusion is greater then or less than the confining

pressure. Stretching results in an increase in T_h within an FIA, and the magnitude of the variation is related to the magnitude of the pressure differential (Bodnar and Bethke, 1984). And, not all inclusions begin to stretch at the same time (i.e., the same amount of pressure differential), resulting in a "smearing" or broadening of the T_h range for the FIA – this is exactly what is observed for most inclusions in this study. We interpret the T_h variations observed here to be the result of various amounts of post-trapping stretching of the inclusions during cooling and uplift of the host phase to the surface. Moreover, it is likely that most fluid inclusions in most samples, especially those from higher pressure and high temperature environments, have stretched to some extent.

2.6. Conclusions

Fluid inclusions have been used for over a hundred years to determine temperatures of geological environments. The precision with which fluid inclusions constrain the temperatures of geologic events depends on the precision with which the temperature of a fluid inclusion assemblage can be determined. Applying the FIA approach in fluid inclusion studies provides the most detailed and accurate analysis of P-T-X history and is the most important step in any fluid inclusion study. Studying FIAs is the only way to test whether the inclusions adhere to Roedder's Rules and to recognize if post-entrapment reequilibration affected the inclusions or not.

The T_h variations within an FIA are influenced by the geologic environment in which the inclusions are formed, the fluid inclusion size, properties of the host mineral and sample collection and preparation in the laboratory. It was observed that even for the smallest observed trapping temperature variations the homogenization temperatures can be determined with a precision (and accuracy) on the order of ± 0.5 to ± 2 degree Centigrade.

In natural environments, the best achievable precision ranges from 1 to 2 degrees Centigrade in MVT deposits, 3 to 4 degrees Centigrade in metamorphic lode gold environments, 2 to 3 degree Centigrade in pegmatites, 2 to 3 degree Centigrade in porphyry deposits, and 0.1 to 3 degree Centigrade in epithermal deposits. Achieving these minimum homogenization temperature variations requires careful petrographic analysis of the samples before any microthermometric analyses are conducted. And, importantly, the results obtained here may not always be achievable in other samples from similar environments, even with careful study. The

results of this study do, however, show that a systematic approach to fluid inclusion studies can produce a precise and accurate estimate of the temperatures associated with various geologic processes.

REFERENCES

Anderson, E. D., Atkinson, W. W. Jr., Marsh, T. and Iriondo, A., 2009, Geology and geochemistry of the Mammoth breccia pipe, Copper Creek mining district: evidence for a magmatic-hydrothermal origin: Mineralium Deposita, DOI 10.1007/s00126-008-0206-2

Barton, P. B., Bethke, P. M. and Roedder, E., 1977, Environment of ore deposition in the Creede mining district, San Juan Mountains, Colorado: III. Progress toward interpretation of the chemistry of the ore-forming fluid for the OH vein: Economic Geology, v 72, p. 1-24.

Beane, R. E. and Titley, S. R., 1981, Porphyry copper deposits. Part II. Hydrothermal alteration and mineralization: Economic Geology, 75th Anniversary Volume, p.235-269

Beane, R. E. and Bodnar, R. J., 1995, Hydrothermal fluids and hydrothermal alteration in porphyry copper deposits, *in* Pierce, F. W. and Bohm, J. G., eds, Porphyry copper deposits of the American Cordillera: Arizona Geological Society Digest (Tucson, AZ), v. 20, p. 83-93.

Becker, S. P., Bodnar, R. J., and Reynolds, T. J., 2009, Temporal and spatial variation in fluid inclusion characteristics in porphyry copper deposit with application to exploration: Economic Geology, in review.

Bethke, P. M., Barton, P. B., Lanphere, M. A., Jr. and Steven, T. A., 1976, Environment of ore deposition in the Creede mining district, San Juan Mountains, Colorado: II. Age of mineralization: Economic Geology, v. 71, p. 1006-1011.

Bethke, P. M. and Rye, R. O., 1979, Environment of ore deposition in the Creede mining district, San Juan Mountains, Colorado: IV. Source of fluids from oxygen hydrogen, and carbon isotopic studies: Economic Geology, v. 74, p. 1832-1851.

Bierlein, F. P. and Crowe, D. E., 2000, Phanerozoic lode gold deposits: Society of Economic Geology Reviews, v. 13, p. 103-139.

Bodnar, R. J., 1983, A method to calculating fluid inclusion volumes based on vapor bubble diameters and P-V-T-X properties of fluid inclusions: Economic Geology, v. 78, p. 535-542.

Bodnar, R. J., 1995, Fluid inclusion evidence for magmatic source for metals in porphyry copper deposits. *in* Thompson, J. F. H., ed., Magmas, fluids, and ore deposits, MAC Short Course, v. 23, p. 139-152.

Bodnar, R. J., 2003a, Introduction to fluid inclusions, *in* Samson, I., Anderson, A. and Marshall, D., eds., Fluid Inclusions: Analysis and Interpretation: Short Course 32, v. 32, Mineralogical Association of Canada, p. 81-99.

Bodnar, R. J., 2003c, Reequilibration of fluid inclusions, *in* Samson, I., Anderson, A. and Marshall, D., eds., Fluid Inclusions: Analysis and Interpretation: Short Course 32, v. 32, Mineralogical Association of Canada, p. 213-231.

Bodnar, R. J., and Bethke, P. M., 1984, Systematics of stretching of fluid inclusions I: Fluorite and Sphalerite at 1 atmosphere confining pressure: Economic Geology, v. 79., p. 141-161.

Bodnar, R. J. and Vityk, M. O., 1994, Interpretation of microthermometric data fro H_2O-NaCl fluid inclusions, *in* De Vivo, B. and Frezzotti, M. L., eds., Fluid inclusions in minerals, Methods and applications, pub. by Virginia Tech, Blacksburg, p. 117-130.

Bodnar R. J., Reynolds T. J. and Kuehn C. A., 1985, Fluid inclusion systematics in epithermal systems .*in* Berger, B. R. and Bethke, P. M., eds., Geology and Geochemistry of Epithermal Systems, Society of Economic Geologists, Reviews in Economic Geology, v. 2, p. 73-98.

Bodnar, R. J., Binns, P. R. and Hall, D. L., 1989, Synthetic fluid inclusions – VI. Quantitative evaluation of the decrepitation behavior of fluid inclusions in quartz at one atmosphere confining pressure: Journal of Metamorphic Geology, v. 7, p. 229-242.

Brantley, S. L., 1992, The effect of fluid chemistry on quartz microcrack lifetimes: Earth and Planetary Science Letters, v. 113, p. 145-156.

Brantley, S. L., Evans, B., Hickman, S. H. and Crerar, D. A., 1990, Healing of microcracks in quartz: implication for fluid flow: Geology, v. 18, p. 136-139.

Campbell, W. R. and Barton, P. B., 2005, Environment of ore deposition in the Creede mining district, San Juan Mountains, Colorado: I. Geologic, hydrologic, and geophysical setting: Economic Geology, v. 100, p. 1313-1324.

Černý, P., 1991, Rare-element granitic pegmatites. Part 1: Anatomy and internal evolution of pegmatite deposits. Part 2: Regional to global environments and petrogenesis: Geoscience Canada, v. 18, p. 49-81.

Černý, P. and Ercit, T. S., 2005, Classification of granitic pegmatites revisited: The Canadian Mineralogist, v. 43, p. 2005-2026.

Cline, J. S. and Bodnar, R. J., 1994, Direct evolution of brine from a crystallizing silicic melt in the Questa, New Mexico, molybdenum deposit: Economic Geology, v. 89, p. 1780-1802.

Coleman, D.S., Bartley, J. M., Glazner, A. F. and Law, R. D., 2005, Incremental assembly and emplacement of Mesozoic plutons in the Sierra Nevada and White and Inyo ranges, California, Field guide for field trip held in conjunction with the Field Forum "Rethinking the Assembly and Evolution of Plutons: Field Tests and Perspectives" 7–14 October 2005 Sierra Nevada and White and Inyo ranges, California: Geological Society of America, Field Forum Field Trip Guide, p. 1-51.

Cooke, D. R., and Simmons, S. F., 2000, Characteristics of epithermal gold deposits: Reviews in Economic Geology, v. 13, p. 221-244.

Fall, A. and Bodnar, R. J., An assessment of the precision of thermal history reconstruction based on fluid inclusions: The effect of fluid inclusion size, In prep.

Fournier, R.O., 1985, The behavior of silica in hydrothermal solutions: Reviews in Economic Geology, v. 2, p. 45–62.

Garven, G., 1985, The role of regional fluid flow in the genesis of the Pine Point Deposit, Western Canada sedimentary basin: Economic Geology, v. 80, p. 307-324.

Garven, G. and Raffensperger, J. P., 1997, Hydrology and geochemistry of ore genesis in sedimentary basins: *in* Barnes, H. L., ed., Geochemistry of hydrothermal ore deposits: John Wiley & Sons, Inc., New York, p. 125-189.

Goldstein, R. H. and Reynolds, T. J. (1994) Systematics of fluid inclusions in diagenetic minerals, SEPM Short Course 31. Society for Sedimentary Geology, p. 199.

Hayba, D. O., 1997, Environment of ore deposition in the Creede mining district, San Juan Mountains, Colorado: I. Epithermal mineralization from fluid mixing in the OH vein: Economic Geology, v. 92, p. 29-44.

Hollister, L. S., Crawford, M. L., Roedder, E., Burruss, R. C., Spooner, E. T. C. and Touret, J., 1981, Practical aspects of microthermometry. *in* Hollister, L. S., Crawford, M. L., eds., Fluid inclusions: applications to petrology: Mineralogical Association of Canada Short Course, v. 6, p. 13-38.

Jackson,, J. L., Matty, D. J., Reynolds, B. A., Chandonais, D. R. and Student, J. J., 2007, Petrology and geochemistry of the Eureka Valley monzonite, White-Inyo mountains, California, Geological Society of America, Abstracts with Program, v. 39, p. 318.

Kendrick, M. A., Burgess, R., Leach, D. and Pattrick, R. A. D., 2002, Hydrothermal fluid origins in Mississippi Valley type ore districts: combined noble gas (He, Ar, K) and halogen (Cl, Br, I) analysis of fluid inclusions from the Illinois-Kentucky fluorspar district, Viburnum Trend, and Tri-State district, Mid-continent United State: Economic Geology, v. 97, p. 453-469.

Knapp, R. B. and Norton, D., 1981, Preliminary numerical analysis of processes related to magma crystallization and stress evolution in cooling pluton environments: American Jourbal of Science, v. 281, p. 35-68.

Kontak, D. J., Smith, P. K., Kerrich, R. and Williams, P. F., 1990, Integrated model for Meguma Group lode gold deposits, Nova Scotia, Canada: Geology, v. 18, p. 238-242.

Kontak, D. J., Horne, R. J. and Smith, P. K., 2001 Meguma gold deposits, Nova Scotia: overview of past work with implications for future work. The Gangue, Geological Association of Canada, Mineral Deposits Division Newsletter, v. 71, p. 1-9.

Kontak, D. J. and Kerrich, R., 2002, An isotopic (C, O, Sr) study of vein gold deposits in the Meguma Terrane, Nova Scotia: implications for source reservoirs: Economic Geology, v. 92, p. 161-180.

Kontak, D. J., Horne, R. J. and Smith, P. K., 2005, Meguma gold deposits of Nova Scotia: complexities of mesothermal, sediment-hosted gold mineralization revealed: Geological Association of Canada Newfoundland Section, 2005 Annual Technical Meeting, Atlantic Geology, v. 41, p. 181.

Landtwing, M. R., Pettke, T, Halter, W. E., Heinrich, C. A., Redmond, P. B., Einaudi, M. T. and Kunze, K., 2005, Copper deposition during quartz dissolution by cooling magmatic-hydrothermal fluids: the Bingham porphyry: Earth and Planetary Science Letters, v. 235, p. 229-243.

Lawler, J. P. and Crawford, M. L., 1983, Stretching of fluid inclusions resulting from a low-temperature microthermometric technique: Economic Geology, v. 78, p. 527-529.

Leach, D. L. and Sangster, D. F., 1993, Mississippi Valley-type lead-zinc deposits: Geological Association of Canada Special Paper 40, p. 289-314.

Leach, D. L., Bradley, D., Lewchuk, M. T., Symons, D. T. A., de Marsily, G. and Brannon, J., 2001, Mississippi Valley-type lead-zinc deposits through geological time: implications from recent age-dating research: Mineralium Deposita, v. 36, p. 711-740.

Leach, D. L., Sangster, D. F., Kelley, K. D., Large, R. R., Garven, G., Allen, C. R., Gutzmer, J. and Walters, S., 2005, Sediment hosted lead-zinc deposits: a global perspective: Economic Geology 100th Anniversary Volume, p. 561-607.

McMillan, W. J. and Pantaleyev, A., 1988, Porphyry copper deposits. *in* Roberts, R. G. and Sheehan, P. A. eds., Ore deposit models, Geological Association of Canada, Geoscience Canada Reprint Series 3, p. 45-58.

Moore, W. J. and Nash, J. T., 1974, Alteration and fluid inclusion studies of the porphyry copper ore body at Bingham, Utah: Economic Geology, v. 69, p. 631-645.

Morgan, S.S., Nabelek, P., Spicuzza, M., and Valley, J., 2007, Deep contact aureoles as natural laboratories to study fluid controlled high strain zones and implications for crustal strength: Peach and Horne, Continental Tectonics Meeting, Geological Society of London, Ullapool, Scotland.

Norton, D., 1978, Sourcelines, sourceregions, and pathlines for fluids in hydrothermal systems related to cooling plutons: Economic Geology, v. 73, p. 21-28.

Redmond, P. B., Einaudi, M. T., Inan, E. E., Landtwing, M. R. and Heinrich, C. A., 2004, Copper deposition by fluid cooling in intrusion-centered systems: new insight from the Bingham porphyry ore deposit, Utah: Geology, v. 32, p. 217-220.

Reynolds, B. A., Matty, D. J., Jackson, J. L., Chandonais, D. R., and Student, J. J., 2007, Petrology and geochemistry of the Joshua Flat quartz monzonite, White-Inyo Mountains, California, Geological Society of America, Abstracts with Program, v. 39, p. 318.

Reynolds, T. J. and Beane, R. E., 1985, Evolution of hydrothermal fluid characteristics at the Santa Rita, New Mexico, porphyry copper deposit: Economic Geology, v. 80, p. 1328-1347.

Richardson, C. K. and Pinckney, D. M., 1984, The chemical and thermal evolution of the fluids in the Cave-in-Rock fluorspar District, Illinois: mineralogy, paragenesis, and fluid inclusions: Economic Geology, v. 79, p. 1833-1856.

Richardson, C. K., Rye, R. O. and Wasserman, M. D., 1988, The chemical and thermal evolution of the fluids in the Cave-in-Rock fluorspar District, Illinois: stable isotope Systematics at the Deardorff Mine: Economic Geology, v. 83, p. 765-783.

Rimstidt, J. D., 1997, Gangue mineral transport and deposition, *in* Barnes, H. L., ed., Geochemistry of hydrothermal ore deposits: John Wiley & Sons, Inc., New York, p. 487-515.

Robert, F., Boullier, A.-M. and Firdaous, K., 1995, Gold-quartz veins in metamorphic terranes and their bearing on the role of fluids in faulting: Journal of Geophysical Research, v. 100, p. 12861-12879.

Roedder, E., 1962, Ancient fluids in crystals: Scientific American, v. 207, p. 38-47.

Roedder, E., 1971, Fluid inclusion studies on the porphyry-type ore deposits at Bingham, Utah, Butte, Montana, and Climax, Colorado: Economic Geology, v. 66, p. 98-120.

Roedder, E, 1974, Changes in ore fluid with time, from fluid inclusion studies at Creede, Colorado. 4th International Association on the Genesis of Ore Deposits (IAGOD) Symposium, Varna, Bulgaria, 1974, Proceedings 2, p. 179-185.

Roedder, E., 1984, Fluid inclusions, *in* Ribbe, P. H., ed., Reviews in Mineralogy, v. 12, Washington, D.C., Mineralogical Society of America, p. 644.

Roedder, E. and Bodnar, R.J., 1997, Fluid inclusion studies of hydrothermal ore deposits: *in* Barnes, H. L., ed., Geochemistry of hydrothermal ore deposits: John Wiley & Sons, Inc., New York, p. 657-697.

Seedorff, E., Dilles, J. H., Proffett, J. M., Jr., Einaudi, M. T., Zurcher, L., Stavast, W. J., Johnson, D. A. and Barton, M. D., 2005, Porphyry deposits: characteristics and origin of hypogene features: Economic Geology 100th Anniversary Volume, p. 251-298.

Sillitoe, R. H., 1973, The tops and bottoms of porphyry copper deposits: Economic Geology, v. 68, p. 799-815.

Simmons, S. F., White, N. C. and John, D. A., 2005, Geological characteristics of epithermal precious and base metal deposits: Economic Geology, 100th Anniversary Volume, p. 485-522.

Simmons, W. B. and Webber, K. L., 2008, Pegmatite genesis: state of the art: European Journal of Mineralogy, v. 20, p. 421-438.

Smith, D. L. and Evans, B., 1984, Diffusional crack healing in quartz: Journal of Geophysical Research, v. 89, p. 4125-4135.

Spry, P. G. and Fuhrmann, G. D., 1994, Additional fluid inclusion data for the Illinois-Kentucky fluorspar district: evidence for the lack of regional thermal gradient: Economic Geology, v. 89, p. 288-306.

Spry, P. G., Koellner, M. S., Richardson, C. K. and Jones, H. D., 1990, Thermochemical changes in the ore fluid during deposition at the Denton Mine, Cave-in-Rock fluorspar district, Illinois: Economic Geology, v. 85, p. 172-181.

Sterner, S. M. and Bodnar, R. J. (1984) Synthetic fluid inclusions in natural quartz I. Compositional types synthesized and applications to experimental geochemistry, Geochimica et Cosmochimica Acta, v. 48, p. 2659-2668.

Steven, T. A. and Eaton, G. P., 1975, Environment of ore deposition in the Creede mining district, San Juan Mountains, Colorado: I. Geologic, hydrologic, and geophysical setting: Economic Geology, v. 70, p. 1023-1037.

Straathof, L. L., Matty, D. J. and Student, J. J., 2006, Petrology and geochemistry of the EJB diorite, White-Inyo Mountains, Eastern California, Geological Society of America, Abstracts with Program, v. 38, p. 353.

Teinturier, S. and Pironon, J., 2003, Synthetic fluid inclusions as recorders of microfracture healing and overgrowth formation rates: American Mineralogist, v. 88, p. 1204-1208.

Titley, S. R. and Beane, R. E., 1981, Porphyry copper deposits. Part I. Geologic setting, petrology, and tectonogenesis: Economic Geology, 75th Anniversary Volume, p. 214-235.

Ulrich, M. R., and Bodnar, R. J., 1988, Systematics of fluid inclusions stretching II: Barite at 1 atm confining pressure: Economic Geology, v. 83, p. 1037-1046.

Vityk, M. O and Bodnar, R. J., 1995, Do fluid inclusions in high grade metamorphic terranes preserve peak metamorphic density during retrograde decompression? American Mineralogist, v. 80, p. 641-644.

Vityk, M. O., Bodnar, R. J. and Schmidt, C. S., 1994, Fluid inclusions as tectonothermobarometers: relation between pressure-temperature history and reequilibration morphology during crustal thickening: Geology, v. 22, p. 731-734.

Vityk, M. O., Bodnar, R. J. and Doukhan, J.-C., 2000, Synthetic fluid inclusions. XV. TEM investigation of plastic flow associated with reequilibration of fluid inclusions in natural quartz: Contribution to Mineralogy and Petrology, v. 139, p. 285-297.

Werre, R. W., Jr., Bodnar, R. J., Bethke, P. M. and Barton, P. B., 1979, A novel gas-flow fluid inclusion heating/freezing stage: Geological Society of America Program with Abstracts, 11, p. 539.

Woods, T. L., Roedder, E. and Bethke, P. M., 1982, Fluid inclusion data on samples from Creede, Colorado, in relation to mineral paragenesis: USGS Open-File Report 82-313, p. 77.

Tables

Table 2.1. T_h and salinity data of fluid inclusions in sphalerite form the Creede, Colorado, epithermal mineralization (data from Roedder, 1977).

FIA	Nr. of inclusions in the FIA	Average T_h (°C)	ΔT_h (°C)	Salinity (wt% NaCl)
1	2	264.9	1.2	9.5
2	18	243.1	2.9	9.0
3	1	246.5	0.0	9.0
4	21	242.6	6.3	8.5
5	27	247.7	2.0	8.8
6	9	247.0	2.0	8.8
7	4	261.6	0.6	9.3
8	9	268.1	1.5	10.2
9	8	256.3	2.0	10.8
10	4	250.9	0.9	10.1
11	15	246.6	2.6	9.5
12	2	250.4	0.0	10.2
13	7	243.0	4.0	9.1
14	12	241.3	3.4	7.6
15	16	198.3	1.1	5.4
16	11	205.6	4.3	7.3
17	4	225.7	2.2	6.8
18	32	227.4	3.2	6.5
19	13	230.5	1.4	6.5
20	8	217.9	1.2	6.3

Figures

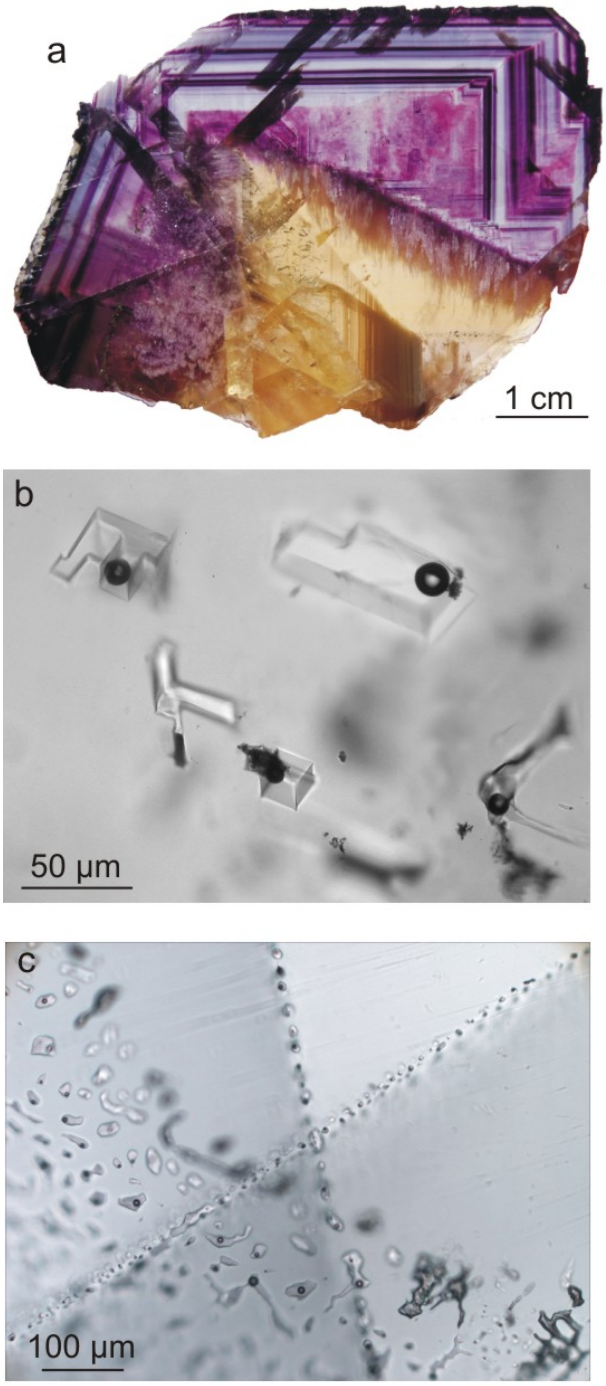

Figure 2.1. (a) Zoned fluorite crystal from the Hill mine, Cave-in-Rock fluorospar district, southern Illinois, showing distinctive growth zones; (b) close-packed small cluster of primary, negative crystal-shaped fluid inclusions in fluorite from Cave-in-Rock; (c) Planes of fluid inclusions forming secondary fluid inclusion assemblages in fluorite from Cave-in-Rock. Two of the FIAs are perpendicular to, and one FIA is at an angle of about 45° to the plane of view.

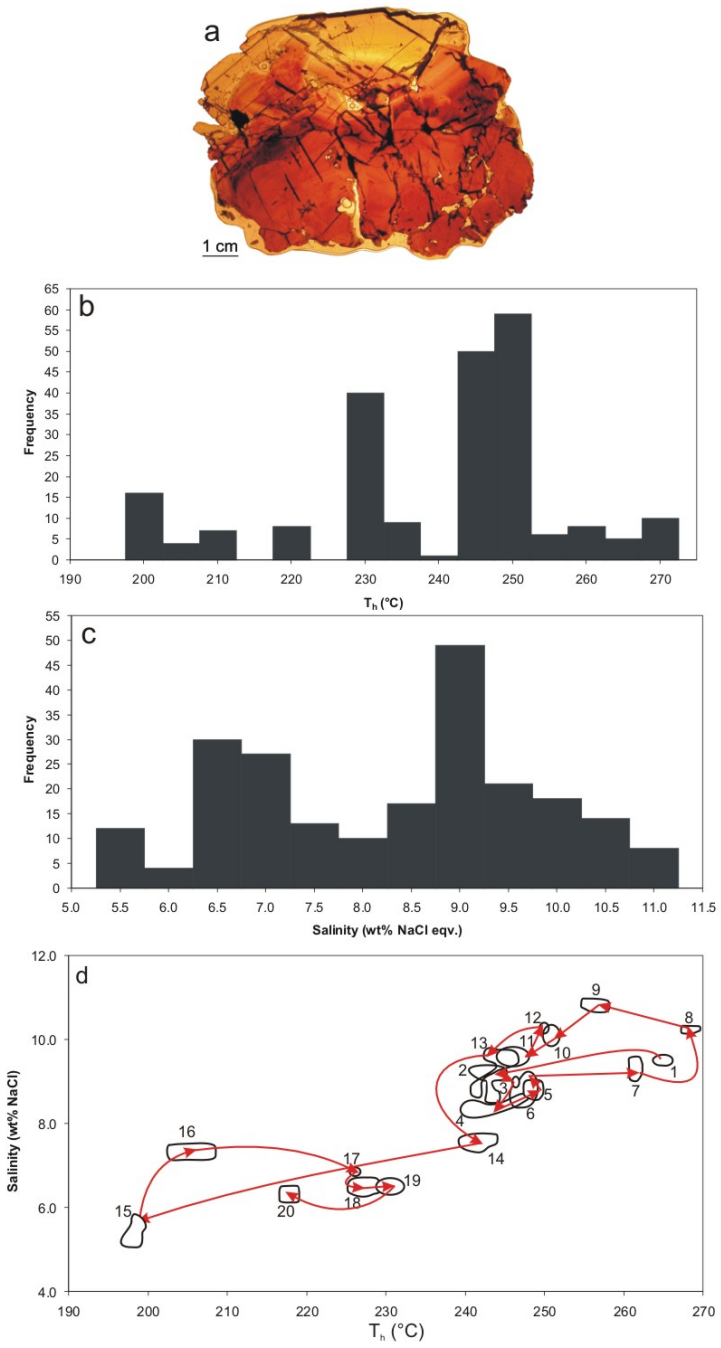

Figure 2.2. (a) Zoned sphalerite crystal (sample NJP-X) from the OH vein of the Creede, Colorado, epithermal deposit. (b) Homogenization temperature distribution of fluid inclusions from the sphalerite crystal. (c) Salinity distribution of fluid inclusions from the sphalerite crystal. (d) Homogenization temperature versus salinity relationships of fluid inclusion assemblages in different stages of the paragenesis, ranging from the earliest zone 1 (innermost) to the latest zone 20 (outermost) in the sphalerite crystal. Arrows show the temporal evolution of temperature and salinity during crystallization (based on Roedder, 1974).

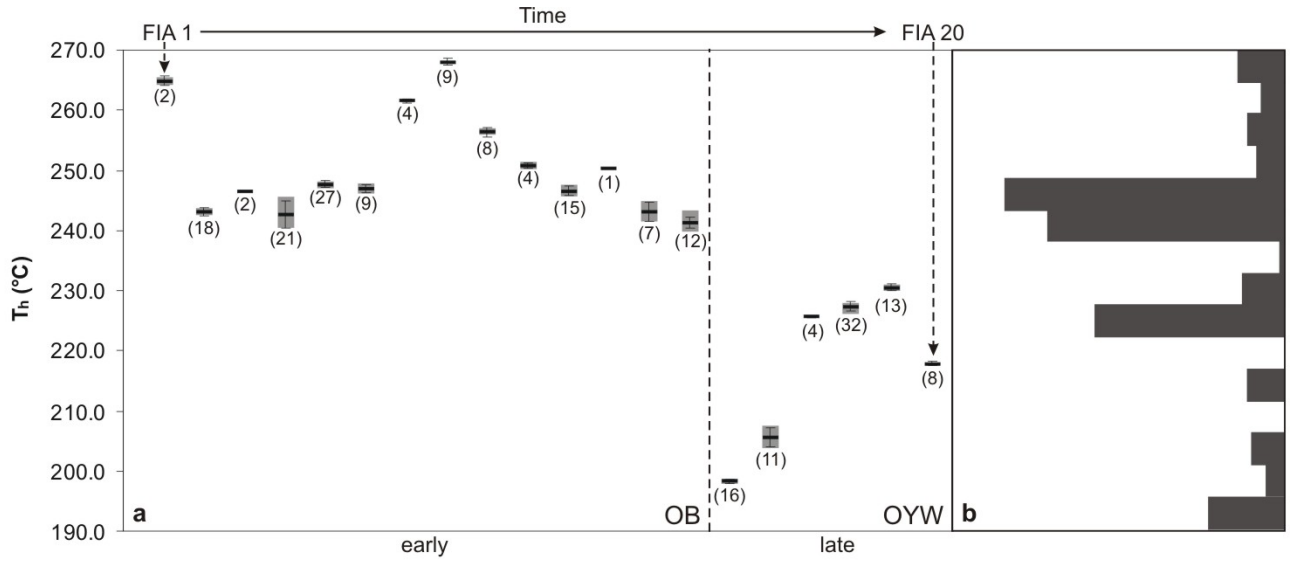

Figure 2.3. (a) Homogenization temperature variations within fluid inclusions assemblages in sphalerite from the OH vein of the Creede epithermal deposit, Colorado (data from Roedder, 1974). The short thick line shows average T_h, the small gray bars show T_h variations within the FIA, and the error bars show standard deviation (1σ) within each FIA; the number of fluid inclusions within each FIA is shown in parentheses; (b) Histogram showing the homogenization temperature distribution in the crystal.

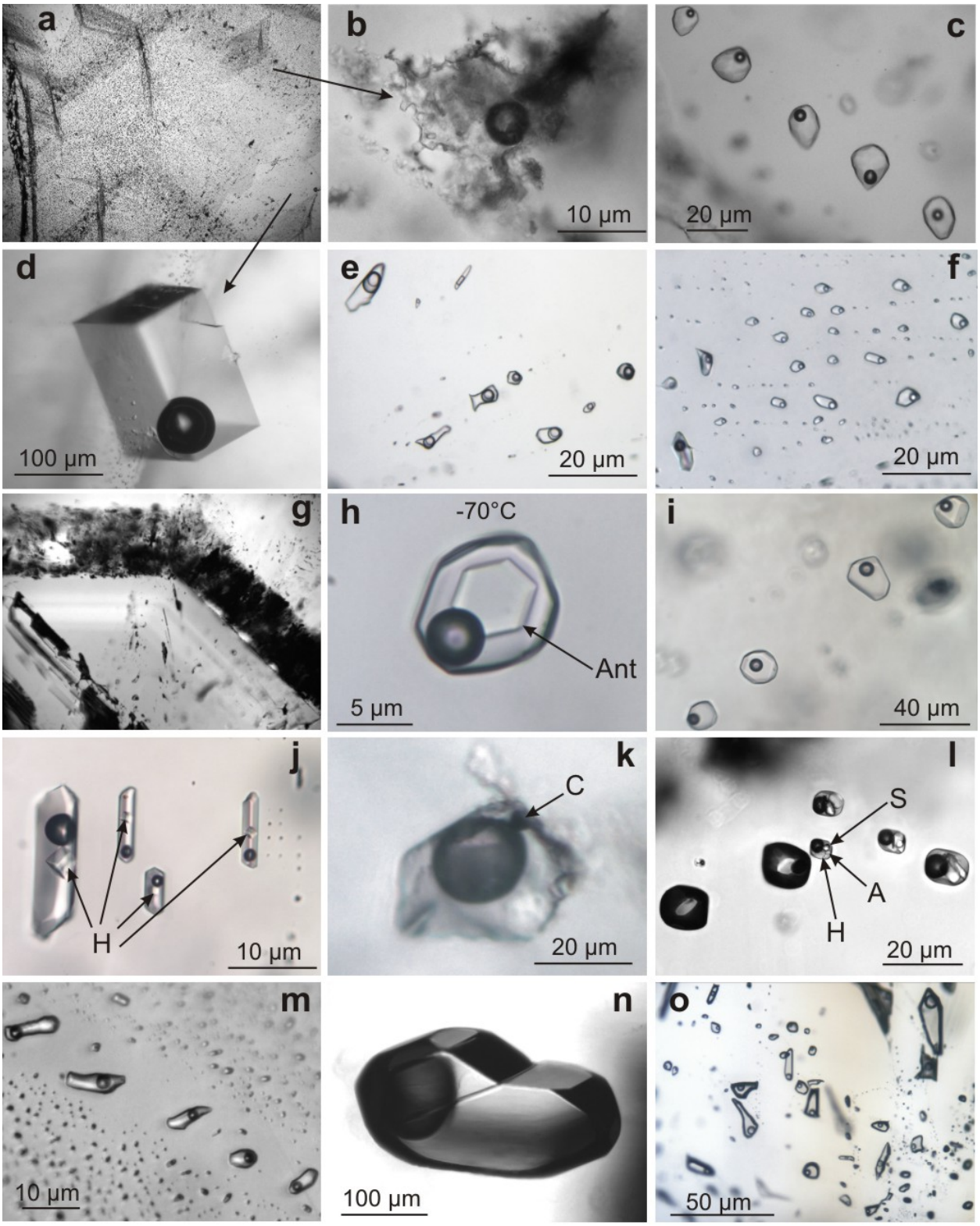
a
b
10 µm
c
20 µm
d
100 µm
e
20 µm
f
20 µm
g
h
-70°C
Ant
5 µm
i
40 µm
j
H
10 µm
k
C
20 µm
l
S
A
H
20 µm
m
10 µm
n
100 µm
o
50 µm

Figure 2.4. Photomicrographs of fluid inclusions from different geological environments: (a) growth zones in fluorite from the Hill Mine, Cave-in-Rock district, Illinois; (b) irregularly-shaped two-phase L-V fluid inclusion in fluorite from the Hill Mine, Cave-in-Rock district, Illinois; (c) trail of secondary fluid inclusions in fluorite from the Hill Mine, Cave-in-Rock district, Illinois; (d) large, negative crystal-shaped two-phase fluid inclusion in fluorite from the Hill Mine, Cave-in-Rock district, Illinois; (e) H_2O-CO_2 fluid inclusions in quartz, containing around 15-20 mol% CO_2, from the Meguma orogenic lode Au deposit, Nova Scotia, Canada; (f) low salinity, two-phase fluid inclusions in quartz from the Meguma orogenic lode Au deposit, Nova Scotia, Canada; (g) dark growth zone in quartz separating zones of clear quartz from the Marble Canyon Pegmatite, California; (h) secondary fluid inclusion in the core of the quartz from the Marble Canyon Pegmatite, California, showing evidence for Ca-rich fluids based on the presence of an antarcticite (Ant) daughter crystal ($CaCl_2 \bullet 6H_2O$) at low temperature; (i) trail of pseudosecondary fluid inclusions in quartz from the Marble Canyon Pegmatite, California; (j) trail of secondary, halite-rich (H) fluid inclusions in the rim of quartz from the Marble Canyon Pegmatite, California; (k) two-phase, liquid-vapor inclusion containing a chalcopyrite daughter mineral (C) in quartz from the Bingham Canyon, Utah, porphyry copper deposit; (l) FIA showing coexisting vapor-rich and brine-rich fluid inclusions from the Bingham Canyon, Utah, porphyry copper deposit. The brine-rich inclusions contain liquid, vapor, halite (H), sylvite (S) and anhydrite (A) daughter minerals; (m) trail of two-phase fluid inclusions in quartz from the Copper Creek, Arizona, porphyry copper deposit; (n) large primary, negative crystal-shaped, fluid inclusion in sphalerite from the Creede, Colorado, epithermal deposit; (o) plane of pseudosecondary fluid inclusions in sphalerite from the Creede, Colorado, epithermal deposit.

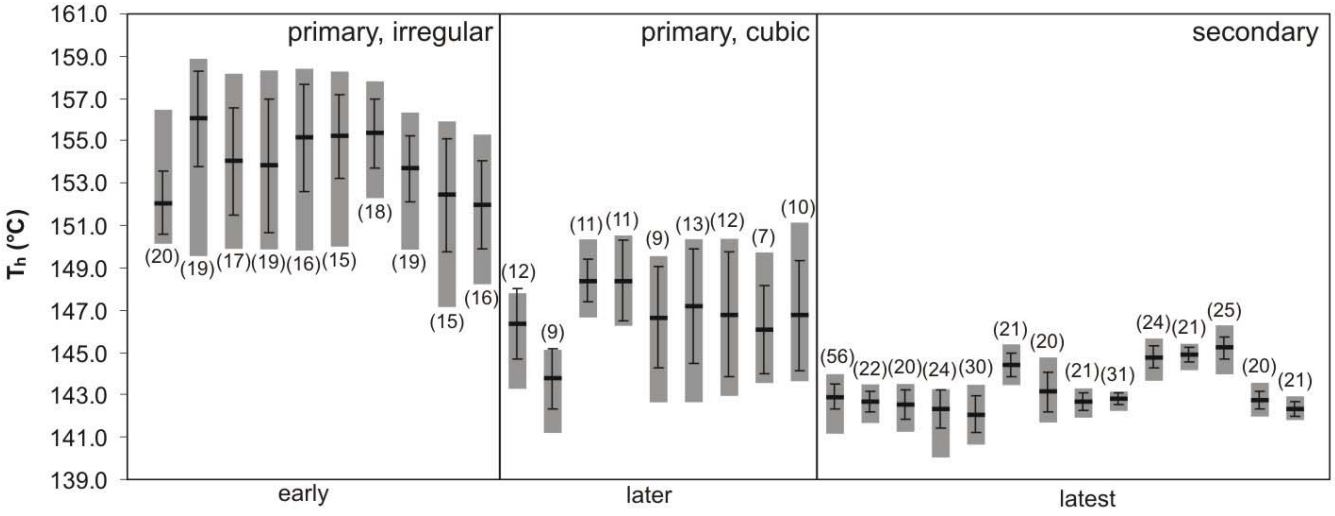

Figure 2.5. Homogenization temperature variations within fluid inclusion assemblages in fluorite from the Cave-in-Rock fluorospar deposit, southern Illinois. The short thick horizontal line shows average T_h, the gray bars show total T_h variation within the FIA, and the error bars (vertical lines) show standard deviation (1σ) within each FIA; the number of fluid inclusions within each FIA is shown in parentheses.

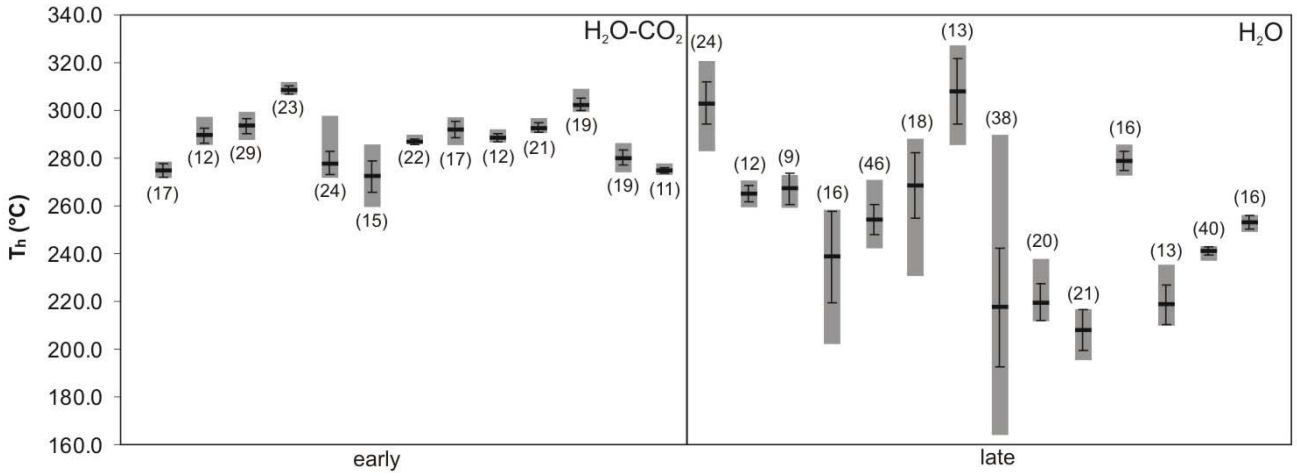

Figure 2.6. Homogenization temperature variations within fluid inclusion assemblages in quartz from the orogenic lode gold deposits of the Meguma metamorphic terrane, Nova Scotia, Canada. The short thick horizontal line shows average T_h, the gray bars show total T_h variation within the FIA, and the error bars (vertical lines) show standard deviation (1σ) within each FIA; the number of fluid inclusions within each FIA is shown in parentheses.

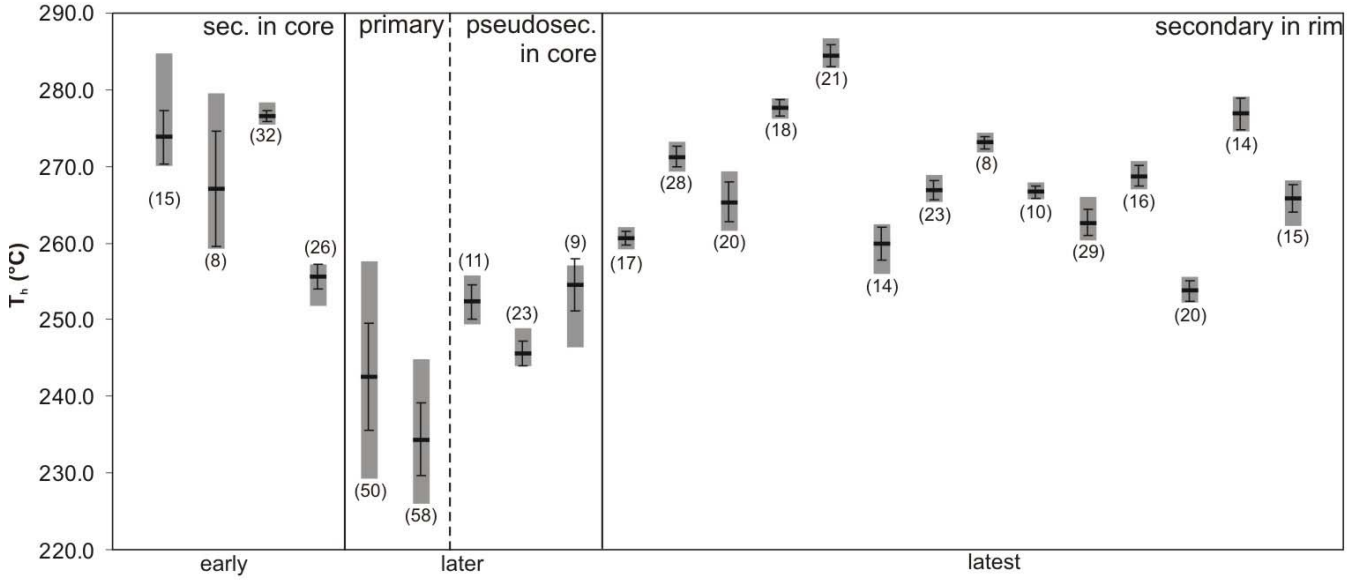

Figure 2.7. Homogenization temperature variations within fluid inclusion assemblages in zoned quartz from the Marble Canyon Pegmatite, California. The short thick horizontal line shows average T_h, the gray bars show total T_h variation within the FIA, and the error bars (vertical lines) show standard deviation (1σ) within each FIA; the number of fluid inclusions within each FIA is shown in parentheses.

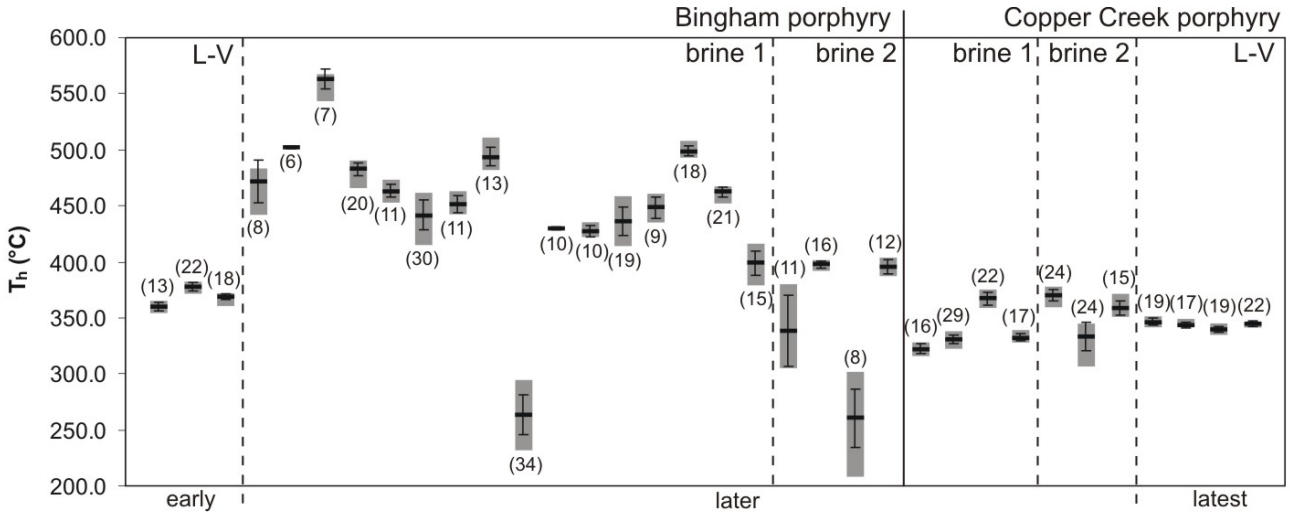

Figure 2.8. Homogenization temperature variations within fluid inclusion assemblages in quartz from the Bingham Canyon porphyry deposit, Utah, and Copper Creek porphyry, Arizona. brine 1 – halite-bearing inclusions that homogenize by vapor disappearance; brine 2 – halite-bearing inclusions that homogenize by halite disappearance. The short thick horizontal line shows average T_h, the gray bars show total T_h variation within the FIA, and the error bars (vertical lines) show standard deviation (1σ) within each FIA; the number of fluid inclusions within each FIA is shown in parentheses.

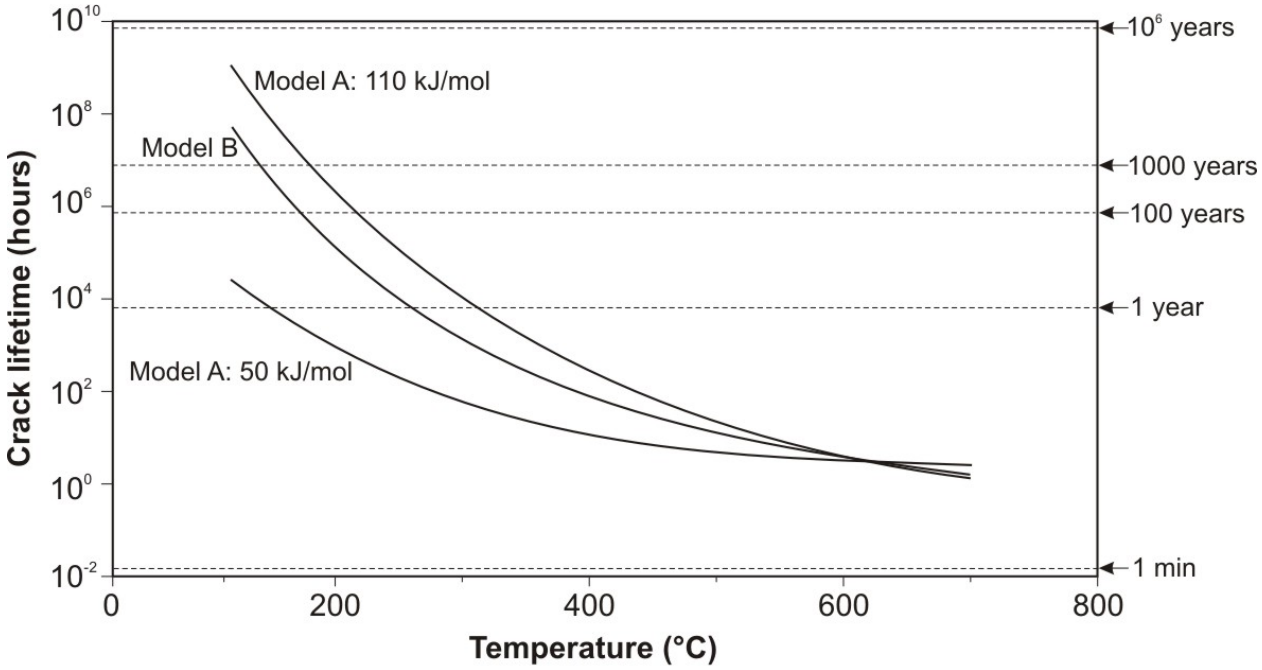

Figure 9.

Figure 2.9. Relationship between temperature and the amount of time required to heal cracks in quartz modified from Brantley et al. (1990), using two different models for the temperature dependence of crack healing and two different activation energies for surface diffusion.

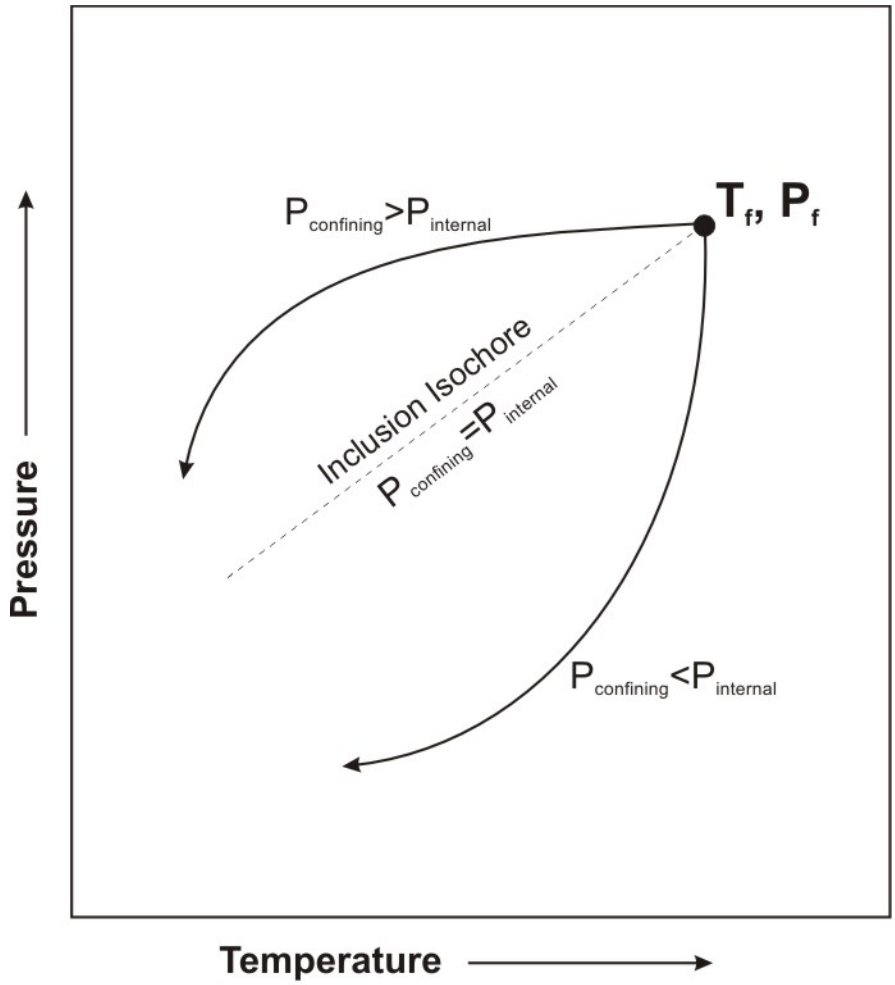

Figure 2.10. Relationship between cooling paths and the confining and internal pressures in fluid inclusions trapped at temperature (T_f) and pressure (P_f) (modified from Bodnar, 2003c).

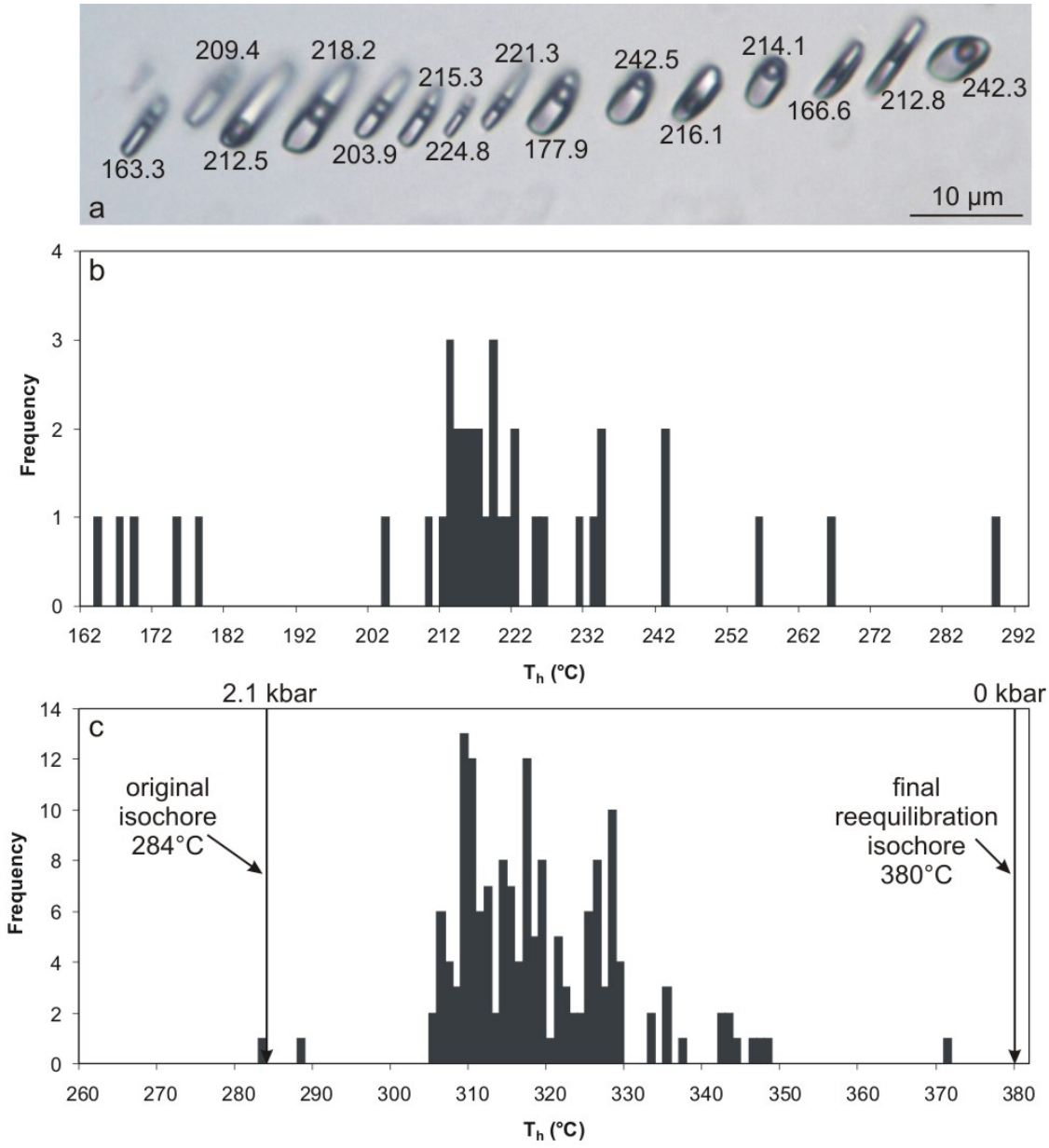

Figure 2.11. Effect of stretching on the homogenization temperature variation of a fluid inclusion assemblage in quartz from the orogenic lode gold deposit of the Meguma metamorphic terrane, Nova Scotia, Canada. (a) photomicrograph of the FIA showing similar-sized and shaped fluid inclusions; the numbers represent homogenization temperatures (in °C) for the individual inclusions in the FIA; (b) histogram showing the distribution of homogenization temperatures within the FIA; (c) histogram showing the distribution of homogenization temperatures for synthetic fluid inclusions that have reequilibrated by stretching at 625°C and 200 MPa, after 180 days (after Vityk and Bodnar, 1995).

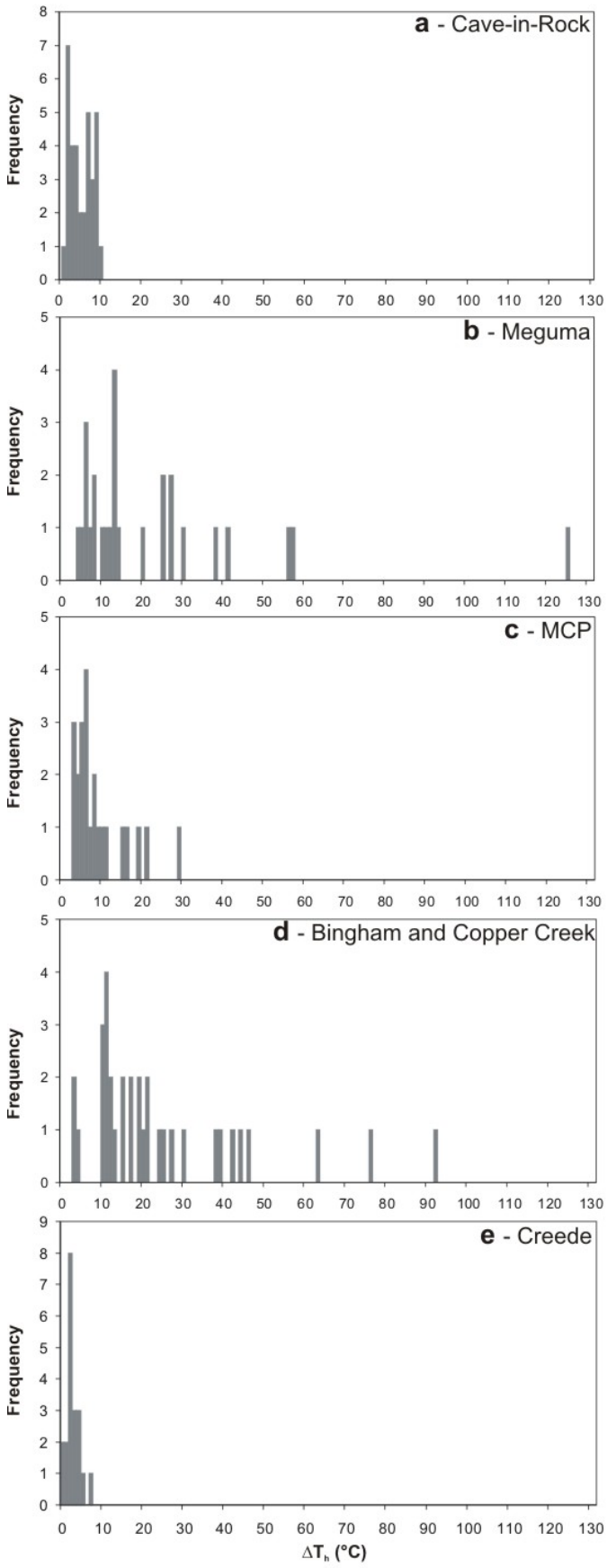
a - Cave-in-Rock
b - Meguma
c - MCP
d - Bingham and Copper Creek
e - Creede
Frequency
ΔT_h (°C)

Figure 2.12. Histograms of homogenization temperature variations (ΔT_h) within fluid inclusion assemblages for the different geologic environments investigated; (a) Cave-in-Rock, Illinois, MVT deposit; (b) Meguma, Nova Scotia, orogenic lode gold deposit; (c) Marble Canyon, California, pegmatite; (d) Bingham Canyon, Utah, and Copper Canyon, Arizona, porphyry copper deposits; (e) Creede, Colorado, epithermal deposit.

CHAPTER 3

Combined microthermometric and Raman technique for determination of salinity of H_2O-CO_2-NaCl fluid inclusions

3.1. Introduction

Fluid inclusions that contain H_2O-CO_2-NaCl are common in many different geologic environments including hydrothermal ore deposits (Roedder, 1971) and medium- to high-grade metamorphic rocks (Robert et al., 1995). Fluid inclusions provide a powerful tool to estimate pressure, temperature, and fluid composition (PTX) history related to various geological processes and accurately knowing the PTX properties and interpreting microthermometric data of H_2O-CO_2-NaCl fluid inclusions requires information on the salinity of the inclusions. The salinity of gas-free fluid inclusions is determined from the ice-melting temperatures and experimental data that relate the salinity and the freezing point depression (Bodnar, 1993). However, if gas is present in the fluid inclusion a hydrate forms when the inclusions are cooled (Fig. 3.1) (Roedder, 1963). Gas-hydrates are crystalline solids formed of water and gas, where the gas molecule is trapped inside a "cage" (clathrate) formed of hydrogen bonded water molecules (Fig. 3.2) (Sloan and Koh, 2008). The hydrate is stable above the ice melting temperature and ice melting is obscured by the hydrate, usually preventing determination of ice melting point. More importantly, as the hydrate incorporates H_2O and rejects salts or ions form its lattice structure, salinities estimated from ice melting temperature are higher then the actual salinity, precluding determination of salinity from the freezing point depression (Roedder, 1963, Collins, 1979). For this reason Collins (1979), based on the experimental data of Chen (1972) and Bozzo et al. (1975), proposed that the clathrate melting temperatures should be used to determine the salinity of the CO_2-rich fluid inclusions.

Clathrate stability in the aqueous-carbonic inclusions is controlled only by the CO_2 pressure and temperature, and in the presence of liquid CO_2, vapor CO_2, and aqueous solution the clathrate melts at +10°C, at the invariant point Q_2 (Fig. 3.3). In their experimental studies, Chen (1972) and Bozzo et al. (1975) observed that adding salt to H_2O-CO_2 solutions shifts the Q_2 point to lower temperatures and pressures similarly with the freezing point depression of H_2O-NaCl

with increasing salinity (Bodnar, 1993) (Fig. 3.3). As the clathrate stability is a function of pressure and temperature, determining the salinity of aqueous-carbonic inclusions requires knowledge of the pressure within the inclusions at the clathrate melting temperature. The point where the pressure is known at clathrate melting in the system H_2O-CO_2±NaCl is on the liquid-vapor curve for the CO_2. Previous models that estimate salinity based on clathrate melting temperature are valid only along this curve, or at the invariant point Q_2 (e. g., Darling, 1991).

The Q_2 point for saline solutions was first determined by Chen (1972) in the range +10 to 0°C (corresponding to 0-16 wt% NaCl). Bozzo et al. (1975) developed the first equation that calculated salinities based on clathrate melting temperatures over the range +10 to 0°C. Darling (1991) noted that the equation of Bozzo et al. (1975) worked well in the given temperature range, however when used over the full temperature range where clathrate melting occurs (+10 to -10°C, corresponding to 0-24.2 wt% NaCl) the equation showed discrepancies in calculating salinities below 0°C. For this reason, combining the experimental data of Chen (1972) and Bozzo et al. (1975), Darling (1991) developed a new equation that is valid at the Q_2 invariant point between +10 and -10°C. In natural fluid inclusions clathrate may dissociate also in the presence of CO_2-vapor or CO_2-liquid only and, as the methods summarized above are valid only along the CO_2 liquid-vapor curve, they cannot be used for these inclusions. For this reason Diamond (1992) developed equations that calculate salinities of aqueous-carbonic inclusions in which the homogenization of CO_2 to liquid or vapor occurs below the clathrate melting temperature ($T_hCO_2<T_mClath$) based on experimental studies on synthetic fluid inclusions. The equations require as input both the CO_2 homogenization temperature and the clathrate melting temperature, and the pressure within the inclusions is determined based on the intersection of the CO_2 isochore with the clathrate melting temperature.

As mentioned above, clathrate stability is a function of pressure and temperature, and determining the salinity of aqueous-carbonic inclusions requires knowledge of both the pressure and the temperature at the clathrate melting. The temperature of the clathrate melting is determined by microthermometry using a heating/freezing stage mounted on a microscope. The inclusions are cooled to nucleate clathrate, and then heated until the clathrate completely melts, at which point the temperature is recorded. To determine the pressure directly in fluid inclusions at the clathrate melting temperature we propose a technique that combines Raman

microspectrometry and microthermometry to determine salinity of CO_2-bearing-aqueous fluid inclusions.

The splitting of the Fermi diad in the Raman spectrum of CO_2 (Fig. 3.4) is density (pressure) dependent (Wright and Wang, 1973; 1975). In this study we determined a relationship between the Fermi diad splitting and density. Using this relationship the density at the clathrate melting temperature of individual synthetic fluid inclusions was determined. Using an equation of state for CO_2, the pressure can be determined if the temperature and density are known. The results were compared to previous models that predict salinity based on clathrate melting temperature along the CO_2 L-V curve to confirm that the proposed method that combines Raman spectrometry and microthermometry can be used to determine salinity of H_2O-CO_2-NaCl fluid inclusions.

3.2. Analytical methods

The splitting of the Fermi diad in the Raman spectrum of CO_2 was calibrated as function of pressure and temperature using a high-pressure optical cell in the Vibrational Spectroscopy Laboratory in the Department of Geosciences at Virginia Tech. The experimental set up for the calibration is similar to that used in a previous study for methane peak calibration (Lin et al., 2007). Kawakami et al. (2003) describe a similar experimental technique for density determination, and their results are similar to those presented below.

The optical cell was connected to a manual pressure generator (High-Pressure Equipment Model #50-6-15) and pressure was monitored using a Precise Instruments pressure transducer (Model 645) accurate to ±0.1% of the pressure output. Ultra-high purity CO_2 was used for calibration and the system was purged several times before each experiment to remove any other gases and/or water from the system. The Fermi diad peaks were measured in 5 bar increments in the 10–100 bar range and in 25 bar increments in the 100-300 bar range, at temperatures of -10, -5, 0, 5, 10, 15, 20, and 22°C. The mean value of two measurements, recorded during increasing and decreasing pressure cycles was taken as the Raman peak position at each pressure, although the difference between the two measurements was generally less than ±0.03 cm^{-1}. The pressure cell was immersed in a constant-temperature liquid bath to maintain a constant temperature during each analysis. An Omega type-E thermocouple, calibrated against the freezing point of

H_2O at 0°C, was inserted into a small hole drilled into the top of the pressure cell, 10 mm deep and 5 mm away from the gas chamber, to monitor the temperature. Temperature varied by <±0.05°C during an individual Raman analysis.

Raman analyses were performed using a JY Horiba LabRam HR (800 mm) spectrometer, with 600 grooves/mm gratings used for the pressure cell and 2400 grooves/mm used for fluid inclusions to achieve a better resolution of the peaks. The slit width was set to 150 µm, and the confocal aperture at 400 µm. Excitation was provided by a 514.53 nm (green) Laser Physics 100S-514 Ar^+ laser. The laser was focused through a 3.5x·objective (N.A. = 0.10) with a working distance of ~12 mm, used for the pressure cell, and a 40x·(N.A. = 0.55) objective with cover-glass correction to improve signal/background ratio (Adar et al., 2004), for fluid inclusions. The laser output was 50 mW at the source and <10 mW at the sample. The detector was an electronically cooled open electrode CCD. Two accumulations of 10 s were used for pressure cell measurements, while the accumulation time for the fluid inclusions varied from 10 seconds to 3 minutes, optimized to achieve approximately similar intensities for different sized fluid inclusions.

Due to the nonlinear behavior of the monochrometer, the spectrometer position was calibrated in the spectral region of interest to optimize precision and accuracy in the peak position determination. The emission line from a mercury (Hg) calibration lamp that was permanently fixed within the optical path of the microscope was recorded simultaneously with each Raman spectrum of the Fermi diad splitting (Fig. 3.4). The position of each measured Raman line was determined after baseline correction using Gaussian/Lorentzian peak fitting. Previous studies (Izraeli et al., 1999; Fukura et al., 2006) demonstrated that the least-square fitting applied to Raman spectra can improve the precision by ~30 times compared to that estimated based on the detector pixel resolution. Figure 3.4 shows an example of simultaneously collected Raman spectrum of the Fermi diad of CO_2 and Hg emission spectra. The 1121.03 cm^{-1} Hg line (relative to the 514.529 nm Rayleigh line of the Ar^+ laser, in air) was used for calibration (McCreery, 2000). Using the measured peak positions for the CO_2 Fermi resonance and the measured and real peak positions for the 1121.03 cm^{-1} Hg, the corrected (real) positions for the CO_2 peaks is obtained by the following expressions:

$$\nu_1 CO_2^{real} = [\nu_1 CO_2^{meas} - (\nu Hg^{meas} - \nu Hg^{real})] \quad (1)$$

and

$$2\nu_2CO_2^{real} = [2\nu_2CO_2^{meas} - (\nu Hg^{meas} - \nu Hg^{real})] \quad (2)$$

The Hg calibration peak was collected simultaneously for every measurement, both in the pressure cell and the fluid inclusions. This method of calibration is necessary to avoid errors related to random variation in the mechanical drive, expansion with temperature and optical aberrations that could influence the measured peak positions.

To determine the relationship between the pressure at the clathrate melting temperature and salinity we used synthetic fluid inclusions with known salinity, prepared by the techniques described by Sterner and Bodnar (1984; 1991) and Azbej et al. (2007). Solutions of H_2O-NaCl with 5, 10, and 20 wt% NaCl, respectively, were prepared. Pre-fractured, clear, inclusion free 15-20 mm long "Brazilian" quartz prisms, together with 100 µl solution and known amount of oxalic acid were loaded into 25 mm long and 5 mm diameter platinum capsules and sealed. The oxalic acid decomposes explosively at 157°C to produce equimolal concentrations of CO_2 and H_2O, as well as H_2, which diffuses out of the capsules at elevated temperatures (Mavrogenes and Bodnar, 1994). The capsules were loaded into externally-heated cold seal pressure vessels, pressurized and heated to the desired experimental conditions of 3-4 kbars and 400-600°C. During the experiment the fractures trap fluid and heal to produce fluid inclusions. As the masses of the components loaded into the capsules was known the salinity of fluid inclusions formed in each capsule could be calculated. The experiments lasted 7 to 10 days, after which the vessels were removed and quenched. The platinum capsules were weighed to check for possible fluid losses. The quartz prisms were removed and sliced into 1 mm thick disks and polished on both sides for microthermometric analysis. Microthermometry was carried out on a Linkam THMSG 600 heating/freezing stage calibrated using the CO_2-ice melting temperature at -56.6°C of H_2O-CO_2 synthetic fluid inclusions, and the ice melting temperatures at 0°C and critical homogenization temperature at 374.1°C of pure H_2O synthetic fluid inclusion standards (Sterner and Bodnar, 1984). This same stage was later mounted onto the Raman spectrometer to measure the splitting of the Fermi diad for CO_2 in fluid inclusions at the clathrate melting temperature.

3.3. Results and Discussion

The relationship between density and the splitting of the Raman spectrum of the Fermi diad of the CO_2 was determined in the high-pressure optical cell using ultrahigh purity CO_2 at the pressure and temperature ranges described above. Figure 3.5a illustrates the relationship between the pressure and splitting of the Fermi diad at the different experimental temperatures, showing that temperature has little effect on the splitting obtained from the vapor CO_2, and more accentuated effect on the splitting obtained from the liquid CO_2. This agrees with the observation of Kawakami et al. (2003). Using the known pressure and temperature in the cell, the density of the fluid was calculated using the equation of state for the CO_2 of Span and Wagner (1996). Figure 3.5b shows the calculated densities versus the splitting of the Fermi diad, Δ. With increasing pressure the two peaks of the split Fermi diad move to lower wavenumbers and Δ increases. The data were obtained from liquid and vapor CO_2 below the CO_2 critical temperature (31.1°C), as evidenced by the two distinctive groupings of data on Figure 3.5. Regression analysis of the data produced the following 3rd order polynomial equation that relates density to the splitting of the Fermi diad:

$$\rho CO_2 = -0.030315\times\Delta^3+9.432835\times\Delta^2-977.938493\times\Delta+33780.382 \qquad (3)$$

where ρCO_2 is the density of carbon dioxide in g/cm^3, and Δ is the distance between the two peaks of the Fermi diad in cm^{-1} (Fig. 3.4). Equation (3) is similar to that of Kawakami et al. (2003) obtained from the Raman spectrum of CO_2 at temperatures of 18-19°C and in the supercritical state at 57-58°C. The calibration developed in this study was necessary to test if the Raman spectrometric technique used to estimate CO_2 density was valid in the range of interest for clathrate melting temperatures between -10 and +10°C.

Equation (3) was used to determine the density of synthetic fluid inclusions containing different salinities. The fluid inclusions were cooled in the heating/freezing stage that was mounted on the Raman microprobe until a clathrate phase nucleated (Fig. 3.2). The clathrate usually forms at the interface between the liquid CO_2 and liquid H_2O. During cooling from room temperature the aqueous phase remains metastable until cooled to about -30°C, at which point clathrate and ice nucleate simultaneously. The inclusion was then heated, controlling the heating

rate, until the clathrate completely melted in the inclusion. It should be noted that clathrate dissociation is sluggish. A technique that is comparable to the thermal cycling technique (Goldstein and Reynolds, 1994) was used to accurately determine the clathrate melting temperature. Recording the clathrate dissociation temperature requires a very small heating rate (usually <5 °C/minute) as large heating rates can result higher clathrate melting temperatures that the true temperature. The inclusions were cooled to nucleate a clathrate and then slowly heated until the clathrate disappeared at the liquid CO_2-liquid H_2O interface. After the point at which clathrate was no longer visible the temperature was held constant for a short period of time after which the inclusion was slowly cooled. If clathrate still remained in the inclusion it started to rapidly grow with a small temperature decrease. At this point the inclusion was heated again until the clathrate disappeared and the time period at which the temperature was held constant was increased. This cycle was repeated until the time period at the constant temperature was long enough to completely melt the clathrate. In some cases a time period of 10-15 minutes was required to reach total clathrate dissociation. As a consequence recording clathrate melting temperatures can be a tedious process. An important observation related to clathrate melting observation could make laboratory work easier and faster. According to this observation once the clathrate melting temperature is determined by microthermometry, the Raman spectrometry can be carried out also during a simple cooling of the inclusion to the clathrate melting temperature. This can be achieved if the inclusion is cooled from room temperature to the previously observed melting temperature without nucleating the clathrate. Figure 3.6 illustrates the good agreement between Fermi diad splitting obtained with the clathrate melting observed through cycling and Fermi diad splitting obtained during simple cooling to the previously determined clathrate melting temperature. The Fermi diad splitting of CO_2 in the halite saturated inclusions was measured by cooling to the previously determined clathrate melting temperature without clathrate nucleation. In the halite-saturated inclusions hydrohalite ($NaCl•2H_2O$) is the last phase to melt (Roedder, 1984; Vityk and Bodnar, 1994), and the structure of the hydrohalite incorporates some H_2O, similarly to the clathrate. To avoid interference from the hydrohalite during collection of the Raman spectrum of CO_2 the inclusion was heated until hydrohalite melted, after which the inclusion was cooled to the observed clathrate melting temperature. At this point the splitting of the Fermi diad could be recorded without interference of the hydrohalite.

Once the clathrate dissociation temperature was determined the fluid inclusion was maintained at that temperature (±0.05°C) and the Raman spectrum of the CO_2 and Hg peaks were simultaneously collected (Fig. 3.4). Between 8 and 10 inclusions were measured within each sample, and Raman spectra were collected from both the liquid and the vapor phases within any single inclusion. Using Equation (3) the densities at the clathrate melting temperatures were determined for individual fluid inclusions. Knowing the density at the clathrate melting temperature permitted the calculation of the pressure within the inclusion using the equation of state for CO_2 of Span and Wagner (1996). The results on Figure 3.7 show a segment of the PT diagram of the system H_2O-CO_2 (Fig. 3.3). Solid lines on the figure represent the experimental data of Larson (1955) for the CO_2 liquid-vapor curve and the CO_2 clathrate stability in the presence of pure water. The dashed lines represent clathrate stability curves for various salinities based on the computer program package "Clathrates" of Bakker (1997) and Bakker and Brown (2003). The H_2O melting curve for various salinities is shown also. As illustrated, pressures determined in this study at the clathrate melting temperature for synthetic fluid inclusions with known salinities are in good agreement with existing models and experimental data for clathrate stability.

Densities were determined from both liquid and vapor CO_2 within the same inclusion. Figure 3.8a shows the densities of salt free H_2O-CO_2 fluid inclusions calculated from Raman Fermi diad splitting collected from both the liquid and the vapor CO_2, illustrated on the insert in Figure 3.8a. In most cases the densities obtained from the liquid and vapor CO_2 within the same inclusion result the same calculated pressures, corresponding to the L-V curve of the CO_2. Projecting the calculated densities from the same inclusion to densities and pressures along the L-V curve of the CO_2 (Span and Wagner, 1996) show a good agreement between the density of the vapor phase in the inclusion and density of CO_2 vapor on the liquid-vapor curve, and between the density of the liquid phase in the inclusion and the liquid density on the liquid-vapor curve of the CO_2, resulting the same calculated pressure in the fluid inclusion. However, some of the Fermi diad splitting obtained from the vapor CO_2 in the inclusions result densities that correspond to vapor densities below the liquid-vapor curve of the CO_2, in the CO_2 vapor field. This results in an error of up to ±2 bars in pressure determinations based on the density of the vapor phase.

3.4. Conclusions

Fluid inclusions approximated by the system H_2O-CO_2-NaCl are common in many different geologic environments and provide valuable information on the pressure, temperature and composition history of fluids present in the geologic environment, so knowing the salinity of these inclusions is of great importance. Several models and equations exist that relate final clathrate melting temperatures to the salinity of these inclusions. Most of these methods use experimental or theoretical data to relate the pressure and clathrate melting temperatures to the salinity of the fluid inclusions. The proposed analytical technique combines Raman microspectrometry and microthermometry to obtain pressures at clathrate melting temperatures directly form individual fluid inclusions. Results obtained on synthetic fluid inclusions with known salinity is in good agreement with existing models and experimental data, suggesting that the proposed method is reasonable in estimating the salinity of H_2O-CO_2-NaCl fluid inclusion.

REFERENCES

Adar, F., Naudin, C., Whitley, A. and Bodnar, R. J., 2004, Use of a microscope objective corrected for a cover glass to improve confocal spatial resolution inside a sample with finite index of refraction: Applied Spectroscopy, v. 58, p. 1136-1137.

Azbej, T., Severs, M. J., Rusk, B. G. and Bodnar, R. J., 2007, In situ analysis of individual H_2O-CO_2 fluid inclusions by laser Raman spectroscopy: Chemical Geology, v. 237, p. 255-263.

Bakker, R. J., 1997, Clathrates: computer programs to calculate fluid inclusion V-X properties using clathrate melting temperatures: Computers and Geosciences, v. 23, p. 1-18.

Bakker, R. J. and Brown, P. E., 2003, Computer modeling in fluid inclusion research: *in* Samson, I., Anderson, A. and Marshall, D., eds., Fluid Inclusions: Analysis and Interpretation: Short Course 32, v. 32, Mineralogical Association of Canada, p. 175-212.

Bodnar, R. J., 1993, Revised equation and table for determining the freezing pint depression of H2O-NaCl solutions: Geochimica and Cosmochimica Acta, v. 57, p. 683-384.

Bozzo, A. T., Chen, H.-S., Kass, J. R. and Barduhn, A. J., , 1975, The properties of the hydrates of chlorine and carbon dioxide: Desalination, v. 16, p. 303-320.

Chen, H.-S., 1972, The thermodynamics and composition of carbon dioxide hydrate, MS Thesis, Syracuse University, Syracuse, New York, p. 67.

Collins, P. L. F., 1979, Gas hydrates in CO2-bearing fluid inclusions and the use of freezing data for estimation of salinity: Economic Geology, v. 74, p. 1435-1444.

Darling, R. S., 1991, An extended equation to calculate NaCl contents from final clathrate melting temperatures in H_2O-CO_2-NaCl fluid inclusions: implications for P-T isochore location: Geochimica et Cosmochimica Acta, v. 55, p. 3869-3871.

Diamond, L. W., 1992, Stability of CO_2 clathrate hydrate + CO_2 liquid + CO_2 vapour + aqueous KCl-NaCl solution: experimental determination and application to salinity estimates of fluid inclusions: Geochimica et Cosmochimica Acta, v. 56, p. 273-280.

Fukura, S., Mizukami, T., Odake, S. and Kagi, H., 2006, Factors determining the stability, resolution, and precision of a conventional Raman spectrometer. Applied Spectroscopy, v. 60, p. 946-950.

Goldstein, R. H. and Reynolds, T. J. (1994) Systematics of fluid inclusions in diagenetic minerals, SEPM Short Course 31. Society for Sedimentary Geology, p. 199.

Izraeli, E. S., Harris, J. W. and Navon, O., 1999, Raman barometry of diamond formation: Earth and Planetary Science Letters, v. 173, p. 351-360.

Kawakami, Y., Yamamoto, J. and Kagi, H., 2003, Micro-Raman densimeter for the CO2 inclusions in mantle-derived minerals: Applied Spectroscopy, v. 57, p. 1333-1339.

Larson, S.D., 1955, Phase studies of the two-component carbon dioxide-water system involving the carbon dioxide hydrate: PhD Dissertation, University of Illinois, Urbana, Illinois.

Lin, F., Bodnar, R. J., and Becker, S. P., 2007, Experimental determination of the Raman CH4 symmetric stretching (v_1) band position from 1-650 bar and 0.3-22°C: Application to fluid inclusion studies: Geochimica et Cosmochimica Acta, v. 71, p. 3746-3756.

Mavrogenes, J. A. and Bodnar, R. J., 1994, Hydrogen movement into and out of fluid inclusions in quartz; experimental evidence and geologic implications: Geochimica et Cosmochimica Acta, v. 58, p. 141-148.

McCreery, R. L., 2000, Raman spectroscopy for chemical analysis: John Wiley & Sons, p. 420.

Robert, F., Boullier, A.-M. and Firdaous, K., 1995, Gold-quartz veins in metamorphic terranes and their bearing on the role of fluids in faulting: Journal of Geophysical Research, v. 100, p. 12861-12879.

Roedder, E., 1963, Studies of fluid inclusions II: freezing data and their interpretation: Economic Geology, v. 58, p. 167-211.

Roedder, E., 1971, Fluid inclusion studies on the porphyry-type ore deposits at Bingham, Utah, Butte, Montana, and Climax, Colorado: Economic Geology, v. 66, p. 98-120.

Roedder, E., 1984, Fluid inclusions, *in* Ribbe, P. H., ed., Reviews in Mineralogy, v. 12, Washington, D.C., Mineralogical Society of America, p. 644.

Sloan, E. D. and Koh, C. A., 2008, Clathrate hydrates of natural gases, 3rd edition: Chemical Industries Series, v. 119, p. 721.

Span, R. and Wagner, W., 1996, A new equation of state for carbon dioxide covering the fluid region from the triple point temperature to 1100 K at pressures up to 800 MPa: Journal of Physical and Chemical Reference Data, v. 25, pp. 1509-1596.

Sterner, S. M. and Bodnar, R. J., 1984, Synthetic fluid inclusions in natural quartz I. Compositional types synthesized and applications to experimental geochemistry: Geochimica et Cosmochimica Acta, 48, p. 2659-2668.

Sterner, S. M. and Bodnar, R. J., 1991, Synthetic fluid inclusions in natural quartz. X., Experimental determination of P-V-T-X properties in the CO_2-H_2O system to 6 kb and 700 °C: American Journal of Science, v. 262, p. 1055-1074.

Vityk, M. O and Bodnar, R. J., 1994, Interpretation of microthermometric data for H_2O-NaCl fluid inclusions: *in* De Vivo, B. and Frezzotti, M. L., eds., Fluid inclusions in minerals. Methods and applications: Virginia Tech, Blacksburg, VA, USA, 117-130.

Wright, R. B. and Wang, C. H., 1973, Density effect on the Fermi resonance in gaseous CO_2 Raman scattering: Journal of Chemical Physics, v. 58, p. 2893-2895.

Wright, R. B. and Wang, C. H., 1975, Effect of density on the Raman scattering of molecular fluids. II. Study of intermolecular interactions in CO_2: Journal of Chemical Physics, v. 61, p. 2707-2710.

Figures

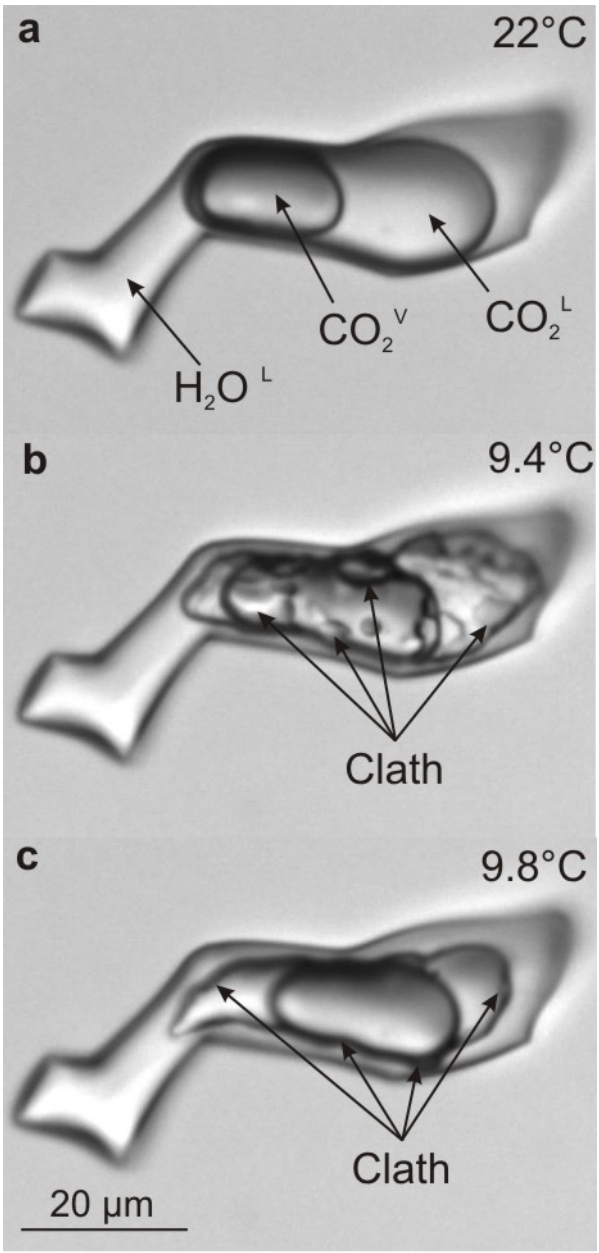

Figure 3.1. Synthetic H_2O-CO_2 fluid inclusion containing 25 mol% CO_2. (a) the inclusion at room temperature, showing tree phases: liquid H_2O, liquid CO_2, and vapor CO_2; (b) the inclusion after clathrate (Calth) nucleated on the liquid H_2O-liquid CO_2 and heated to 9.4°C; (c) the inclusion at 9.8°C, close to the clathrate dissociation temperature.

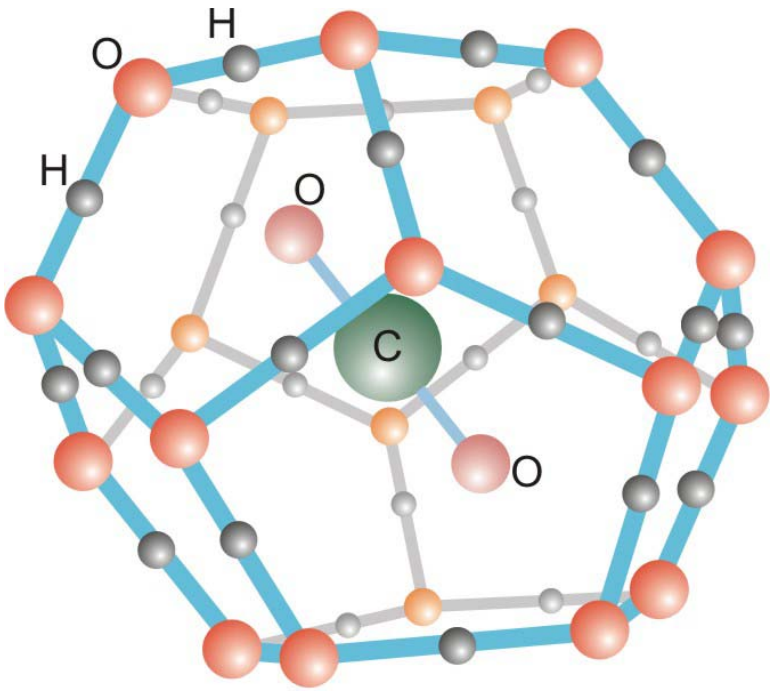

Figure 3.2. The structure of the CO_2 hydrate "cage" (clathrate) (CO_2•5.7H_2O) formed by hydrogen bonded water molecules with the CO_2 molecule residing within the clathrate.

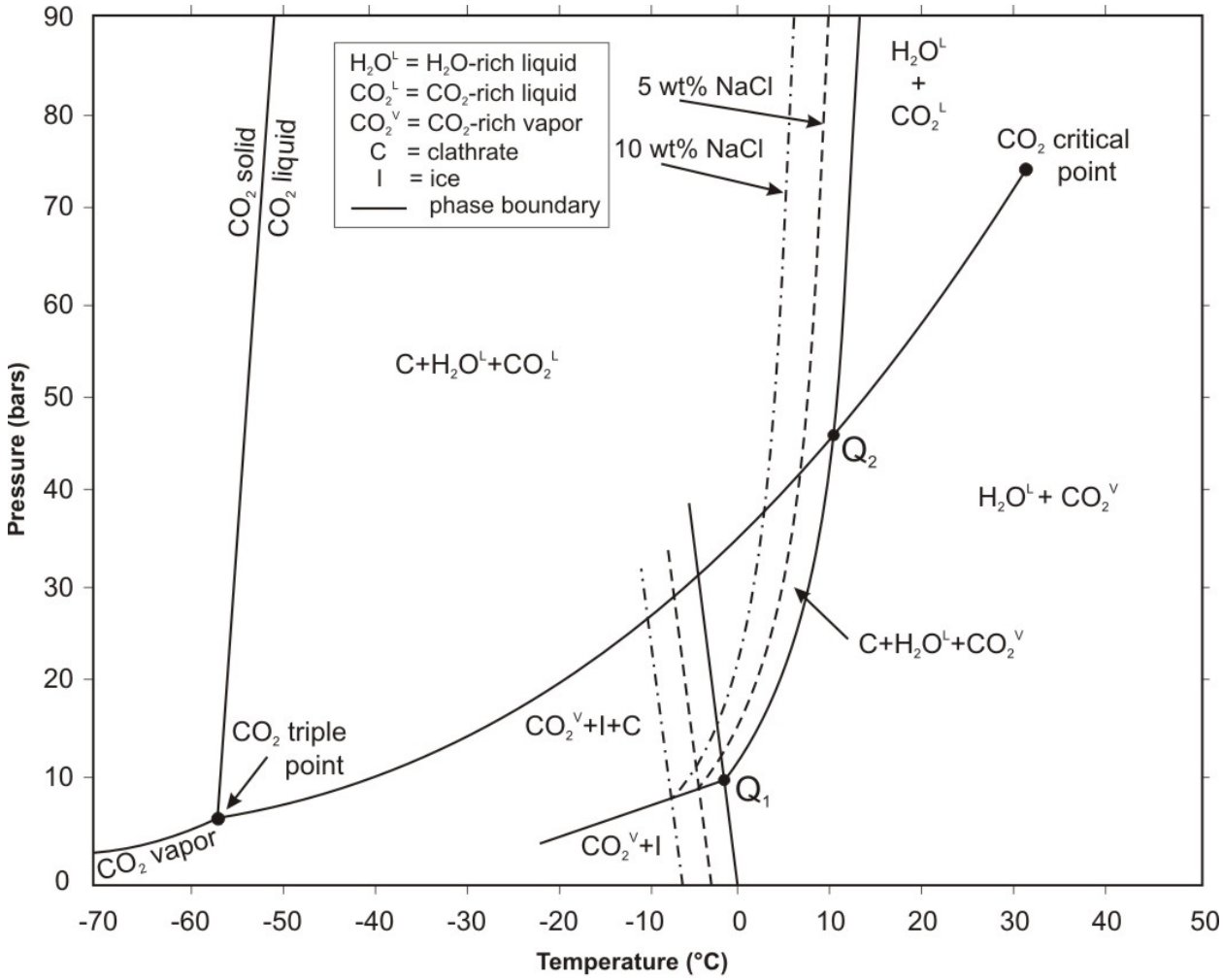

Figure 3.3. The phase diagram of the system H_2O-CO_2-NaCl. Solid lines represent phase boundaries based on data of Larson (1955). Dashed lines represent the CO_2 clathrate stability curves for 5 and 10 wt% NaCl salinity, based on experimental data of Chen (1972).

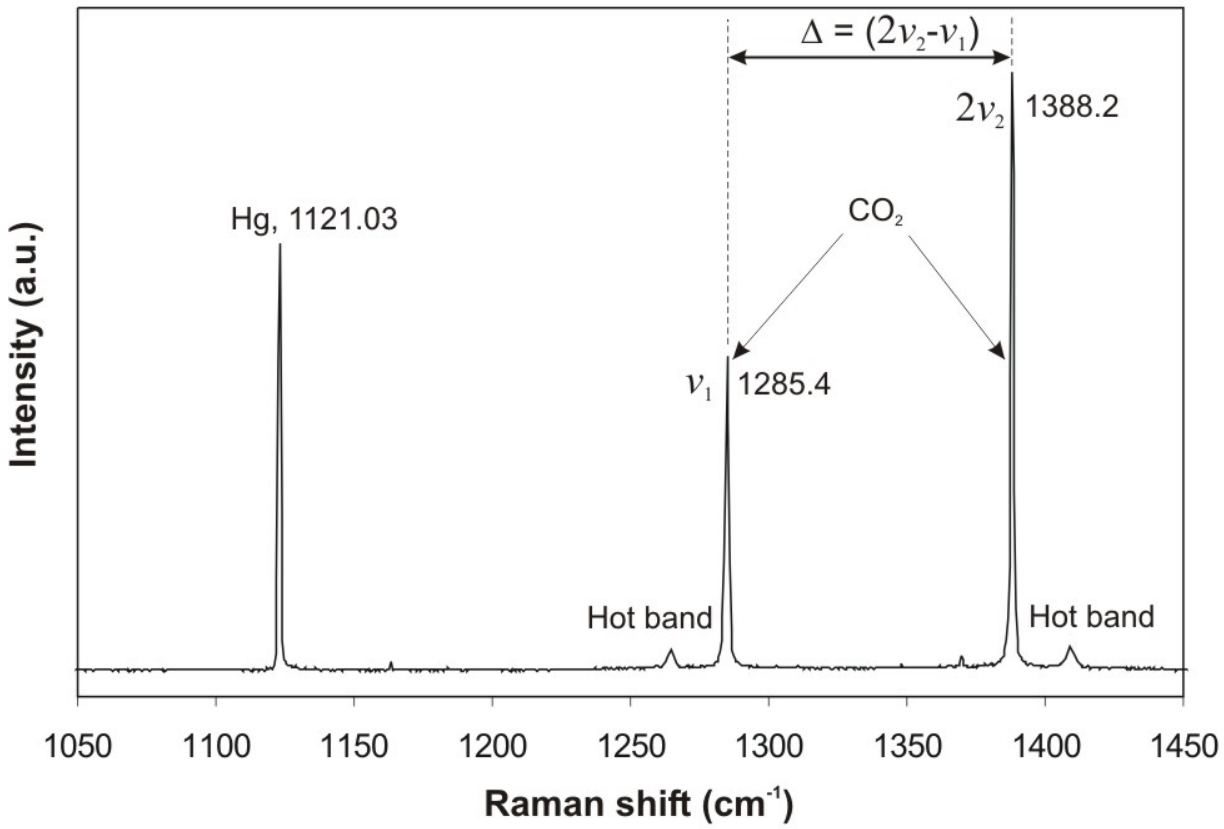

Figure 3.4. Raman spectrum showing the splitting of the Fermi for CO_2. Δ represents the difference between the $2\nu_2$ and ν_1 peak positions, and is density dependent. The low intensity hot bands are due to the thermal energy of the vibrating molecules. Also shown is the Hg peak used for calibration.

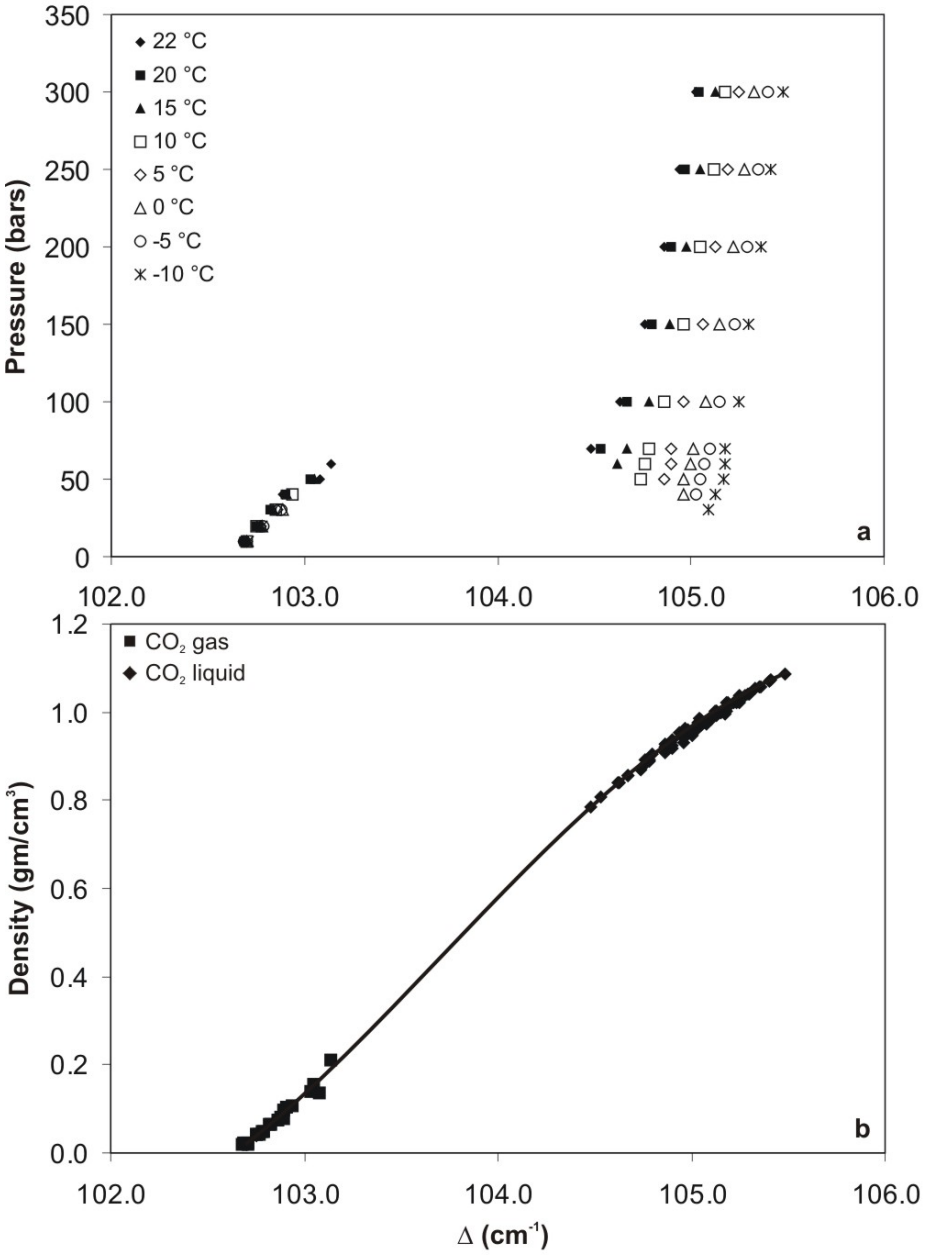

Figure 3.5. (a) Relationship between the experimental pressure and temperature and splitting of the Fermi diad for CO_2 in the high-pressure optical cell; (b) Density in function of Δ for CO_2 in the high-pressure optical cell. The fitted line corresponds to the equation $\rho CO_2 = -0.030315\times\Delta^3+9.432835\times\Delta^2-977.938493\times\Delta+33780.382$, where ρCO_2 is the density of CO_2 in g/cm^3.

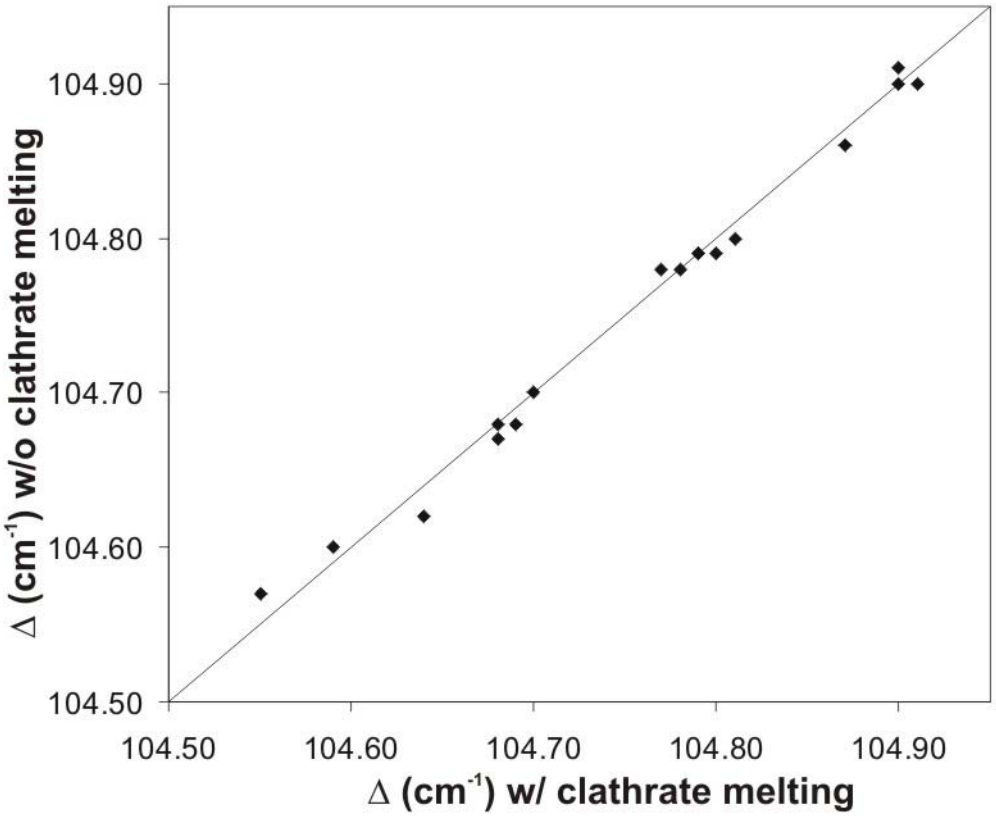

Figure 3.6. Splitting of the Fermi diad for CO_2 obtained at clathrate melting temperature by cycling versus splitting of the spitting obtained by simple cooling of the inclusion to the previously determined clathrate melting temperature.

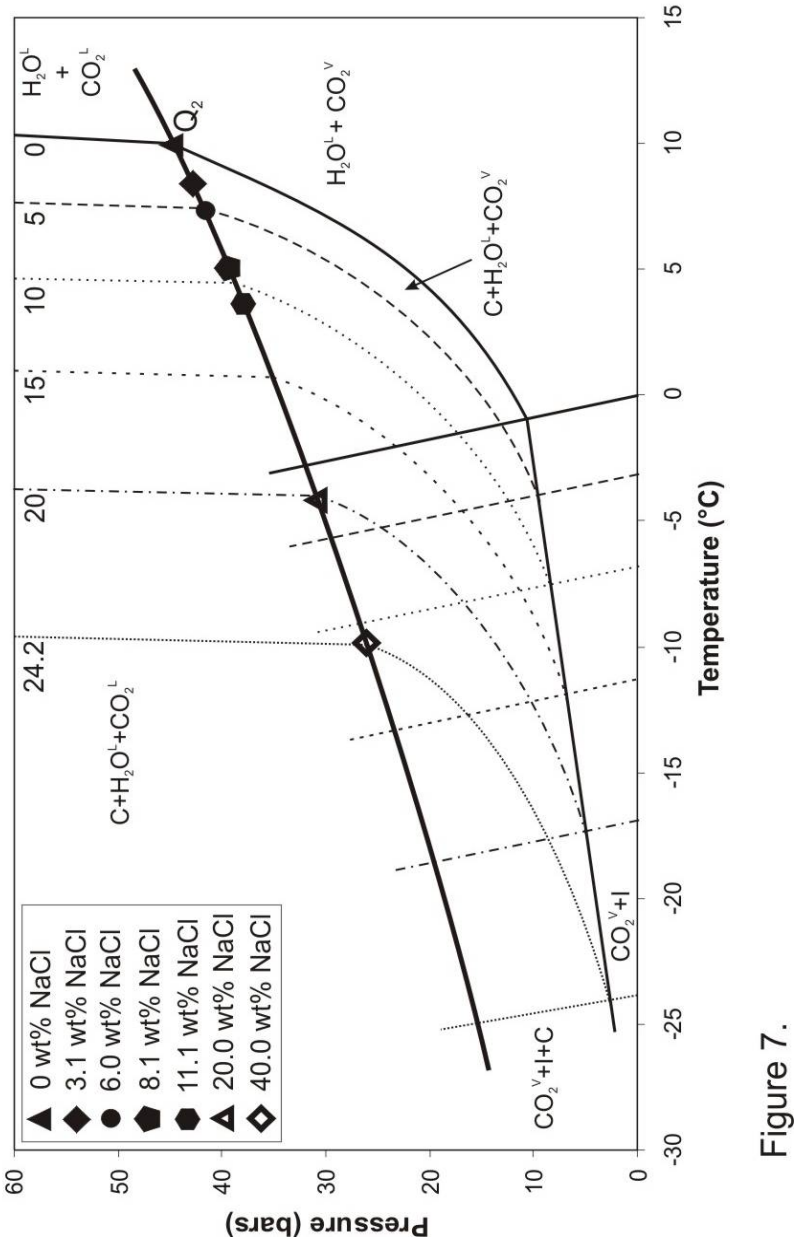

Figure 7.

Figure 3.7. Segment of the phase diagram of the system H_2O-CO_2-NaCl. P-T points corresponding to various salinities of synthetic fluid inclusions calculated combining Raman spectrometry and microthermometry. Solid lines represent phase boundaries based on experimental data of Larson (1955). Thick solid line represents the CO_2 liquid-vapor curve. Dashed lines represent clathrate stability curves for various salinities based on the computer program package "Clathrates" of Bakker (1997) and Bakker and Brown (2003). Abbreviations same as on Fig. 3.

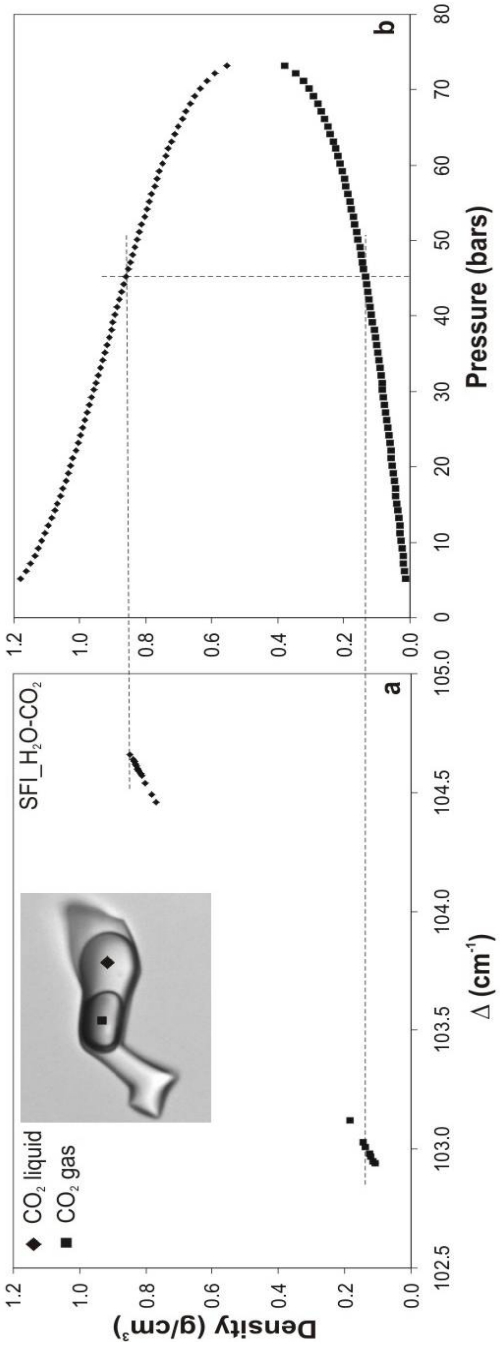

Figure 3.8. (a) Calculated density in function of splitting of the Fermi diad for CO_2 recorded from the vapor and liquid phases of CO_2 in the inclusions. (b) Theoretical densities in function of pressure for CO_2 along the L-V curve. In most cases densities obtained from the liquid and vapor CO_2 phases in the inclusions result the same calculated pressure along the L-V curve of the CO_2.